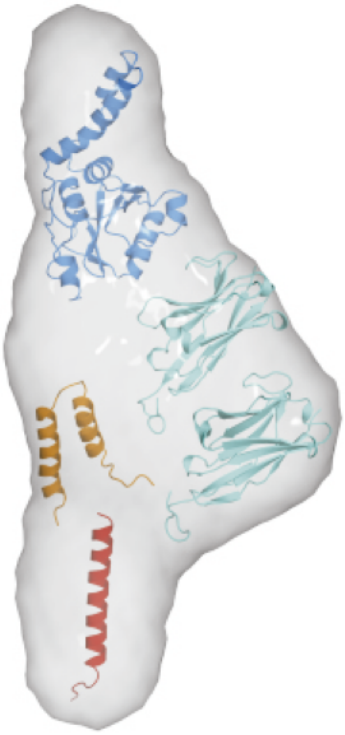

Molecular tools to tackle Ataxin-3 aggregation in Machado-Joseph disease

Ana Viana de Almeida
Mestrado em Bioquímica
Departamento de Química e Bioquímica
2016/2017

Orientador
Dr. Sandra de Macedo Ribeiro, Principal Investigator, IBMC/i3S

Coorientador
Dr. Alexandra Silva, Assistant Researcher, IBMC/i3S

INSTITUTO DE INVESTIGAÇÃO E INOVAÇÃO EM SAÚDE
UNIVERSIDADE DO PORTO

U.PORTO
INSTITUTO DE CIÊNCIAS BIOMÉDICAS ABEL SALAZAR
UNIVERSIDADE DO PORTO

U.PORTO
FACULDADE DE CIÊNCIAS
UNIVERSIDADE DO PORTO

Todas as correções determinadas pelo júri, e só essas, foram efetuadas.
O Presidente do Júri,

Porto, _____/_____/_____

Agradecimentos

Gostaria de agradecer à Dra Sandra Ribeiro por me ter acolhido no seu grupo de investigação para este ano de aprendizagem, obrigada pela oportunidade, auxílio e ensinamentos que partilhou comigo.

Em seguida agradeço à Alexandra Silva por todo o tempo que tirou do seu trabalho para me ajudar e ensinar a estar numa bancada. Obrigada ainda pelo apoio, motivação e conselhos ao decorrer deste ano.

A todos os restantes elementos do grupo: Dr Pedro Pereira, Inês Correia, Jorge Ripoll, José Manso, Joana Fraga, Tatiana Cereija, Pedro Martins e em especial à Zsuzsa Sárkány por me terem mostrado o que é um grupo de investigação e trabalho em equipa.

A todos os meus amigos pelo qual tenho um enorme carinho: Ana Spencer, Vasco Fontes, Daniel Botto pelos almoços e companhia durante este ano. Aos meus afilhados e padrinhos que deixei para vir para o Porto e por fim às melhores pessoas que a FCT UNL me apresentou e vão ficar para sempre. A todos vós pelos momentos inesquecíveis que tantas saudades tenho.

À minha Mãe e ao meu Pai, por todas as oportunidades, por me terem ensinado a ser a pessoa que sou hoje, as saudades nunca… nunca desaparecem. Ao meu Mano, pelo maior amor que alguém pode sentir.

Ao meu João.

Abstract

Machado-Joseph Disease (MJD) is a neurodegenerative disorder included in the group of polyglutamine (polyQ) expansion diseases caused by an expansion of the polyQ tract of Ataxin-3 (Atx-3). This protein possesses a globular domain termed Josephin Domain (JD), which contains aggregation-prone regions (APRs) required for the initial steps of aggregation, a process independent of the polyQ expansion. A few interacting partners of Atx-3 are known to modulate the aggregation rate by protecting these APRs. With this knowledge, this work focused on elucidating the potential of nanobodies (NB) (antigen-binding domain derived from camelid heavy-chain antibodies) produced against the JD in the modulation of the aggregation process of Atx-3.

After production and screening of 17 different NBs the four most promising were selected for further investigation of their biochemical and biophysical properties. The affinity of the interaction between NB01, 02 or 05 and different Atx-3 truncation variants (Atx-3 D1) and isoforms (Atx-3 13Q and 77Q) was determined to be in nanomolar range. NB03 showed no interaction and was used as a negative binding control. Combining Dynamic Light Scattering and Small Angle X-ray Scattering it was possible to observe a structural change in Atx-3 caused by the presence of a NB: while Atx-3 naturally displays an elongated structure the complex (Atx-3 13Q:NB01) presents a more globular shape upon binding of two NB molecules.

When exploring the ability of these NBs to modulate the aggregation process of Atx-3 it was concluded that their presence interfered with the self-assembly of the protein, increasing the lag phase of aggregation. Also, the morphology of mature amyloid fibrils present in the endpoint of the aggregation assay was modified by incubation with the NBs. However, intermediate species such as toxic oligomers or protofibrils are still detected. NB01 showed a significant impact in slowing down aggregation at a ratio of 1:2 (Atx-3:NB01). Additionally, NB05 presented a strong effect on the aggregation of expanded Atx-3 77Q without affecting normal Atx-3 13Q. As such, the latter may be an asset in the therapy against pathological Atx-3.

Ultimately, results show that NBs are a promising tool in the therapeutic research of Machado-Joseph Disease and open a novel approach in the study of this disease.

Keywords:

Neurodegeneration, Machado-Joseph Disease, Ataxin-3, Polyglutamine tract, Josephin Domain, Dynamic Conformation, Aggregation-prone Region, Protein Aggregation, Self-assembly, Amyloid Fibril, Oligomers, Modulation of Aggregation, Nanobodies.

Resumo

A doença de Machado-Joseph (MJD) é uma doença neurodegenerativa em que uma das causas para os sintomas corresponde à acumulação da proteína Ataxina-3 (Atx-3) quando esta apresenta uma expansão na região de poliglutaminas (polyQ). Esta proteína apresenta um domínio globular, Domínio Josefina (JD), que contempla regiões propensas a agregar (APR) responsáveis pelos primeiros passos de agregação, independentemente da expansão de polyQ. Recentemente, têm sido identificadas algumas proteínas capazes de se ligar ao JD como moduladoras da agregação da Atx-3, exercendo uma proteção das APR. Deste modo, definimos como objetivo deste trabalho o estudo das potencialidades do uso de nanobodies (NB) (domínio de ligação ao antigénio derivados de anticorpos de cadeia pesada de camelídeos) produzidos contra o JD para avaliar o efeito dos mesmos na modulação da agregação da Atx-3.

Após a produção de 17 NBs, os 4 mais promissores foram selecionados e as propriedades bioquímicas e biofísicas caracterizadas. As afinidades da interação entre os NB01, 02 e 05 com formas truncadas (Atx-3 D1) ou isoformas (Atx-3 13Q e 77Q) da Atx-3 foram determinadas na escala dos nanomolar, não tendo sido possível detetar interação com o NB03 que foi subsequentemente usado com controlo negativo. Combinando os dados de *Dynamic Light Scattering* (DLS) e *Small Angle X-Ray Scattering* (SAXS) foi possível denotar que enquanto que a Atx-3 apresenta naturalmente uma estrutura alongada, a presença de duas moléculas de NB01 torna o complexo mais globular. Com o estudo da capacidade de modulação destes NBs na agregação da Atx-3 ficou concluído que de facto estes interferem com a oligomerização da proteína, aumentando o tempo da *lag-phase da* agregação. As fibras maduras presentes no final do processo de agregação são alteradas com a incubação com os NBs. No entanto, espécies oligoméricas intermediárias continuam presentes.

O NB01 apresentou um impacto significativo no atraso do início da agregação num rácio de 1:2 (Atx-3:NB). Ainda, o NB05 mostrou um maior efeito na modulação da agregação na Atx-3 expandida sem alterar a agregação da proteína normal, demonstrando o seu potencial na terapia da doença. Os NBs aqui estudados apresentam-se então como moléculas promissoras para estudos na doença de MJD.

Palavras-Chave:

Neurodegeneração, Doença de Machado-Joseph, Ataxina-3, expansão de poliglutaminas, Domínio Josefina, Conformação dinâmica, propenso à agregação, agregação, oligomerização, fibras de amiloide, oligómeros, modulação da agregação, nanobodies.

Table of Contents

List of Tables

List of Figures

Appendix

Abbreviations

MJD	Machado-Joseph Disease
PolyQ	Polyglutamine
Atx-3	Ataxin-3
Atx-3 13Q	Non-expanded Ataxin-3
Atx-3 77Q	Expanded Ataxin-3
JD	Josephin Domain
APR	Aggregation-prone Region
NB	Nanobody
Htt	Huntingtin
HD	Huntington's disease
Atx-1, 2 and 7	Ataxin-1, 2 and 7
SCA 1, 2, 6, 7 and 17	Spinocerebellar Ataxias 1, 2, 6, 7 and 17
CACNA1A	Voltage-dependent Calcium Channel α-1A subunit
TBP	TATA-binding protein
Atn1	atrophin-1
DRPLA	Dentatorubral-Pallidoluysian Atrophy
AR	Androgen Receptor
SBMA	Spinal-Bulbal Muscular Atrophy
DUB	Deubiquitinase
UIM	Ubiquitin Interaction Motifs
NLS	Nuclear Localization Signal
PTM	Post-translational modification
αB-c	Small Heat Shock Protein AlphaB-Crystallin
IgG	Immunoglobulin G
VH	Variable Domain of IgG
V_HH	Variable Domain of Camelid Ig
kDa	Kilodalton
CDR	Complementarity Determining Region
UV	Ultraviolet radiation
CD	Circular Dichroism
LB	Luria-Bertani broth medium
LB-ON	Luria-Bertani broth medium with low osmolarity
SOB	Super Optimal Broth
TB	Terrific Broth
ON	Over Night

Rpm	Revolutions Per Minute
OD_{600}	Optical Density
A_{260}	Absorbance at 260 nm
Amp	Ampicillin
DMSO	Dimethyl Sulfoxide
IPTG	Isopropyl β-D-1-thiogalactopyranoside
PMSF	Phenylmethylsulfonyl Fluoride
SDS	Sodium Dodecyl Sulfate
SDS-PAGE	Sodium Dodecyl Sulfate - Polyacrylamide gel electrophoresis
TBS	Tris-Buffered Saline
DTT	Dithiothreitol
EDTA	Ethylenediaminetetraacetic acid
ECL	Enhanced Chemiluminescence
6-His	Hexa-histidine tag
BSA	Bovine Serum Albumin
SEC	Size Exclusion Chromatography
DLS	Dynamic Light Scattering
SAXS	Small Angle X-ray Scattering
ITC	Isothermal Titration Calorimetry
Kcal	Kilocalorie
K_D	Dissociation Constant
N	Stoichiometry of the reaction
ΔH	Enthalpy Energy
ΔG	Gibbs Energy
$-T\Delta S$	Entropy Energy
TEM	Transmission Electron Microscopy
ThT	Thioflavin T
PdI	Polydispersity Index
NDS	Normalized Spatial Discrepancy
P (r)	Distance Distribution Function
Rg	Radius of Gyration
Tm	Melting Temperature
HMW	High Molecular Weight

Introduction

Protein Misfolding

Proteins perform crucial functions in nearly all biological processes. They are responsible for cellular homeostasis as catalysts, having functions in DNA repair, intercellular communication, transport and molecule storage, providing mechanical support and immune protection, among many other functions.

To accomplish their suitable biological function, polypeptides require folding from a random coil structure (after translation) to a native state (three-dimensional functional state). Acquiring a native structure is usually essential for protein function, but in some cases specific protein domains (or even whole proteins) remain unfolded to achieving their biological function.

Folding errors may lead to the formation of misfolded and inactive proteins which might accumulate and interfere with cellular homeostasis[1]. Many studies have been performed to understand the nature of protein folding mechanisms and energy landscapes are nowadays used to describe them (Figure 1). The energy landscape profile regards a dynamic process between the folded and unfolded states. During folding, the protein procures the lowest energy conformation (native state). Structural fluctuations of the native state may induce temporarily less-folded conformations (partially folded states) that might trigger protein aggregation[2,3].

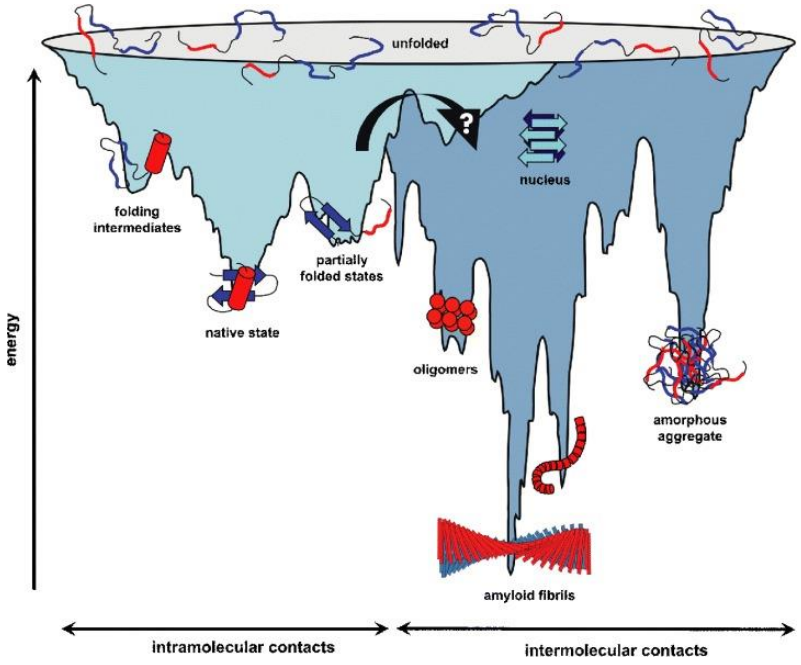

Figure 1: Energy landscape scheme for protein folding and aggregation. The vast conformational states of an unfolded protein merge into a native state via establishment of intramolecular contacts. The exposure of some aggregation-prone regions may lead to intermolecular contacts forming aggregated species with decreasing energy, such as oligomers, amorphous aggregates and at last amyloid fibrils. These amyloid fibrils possess the lowest energy possible, which makes this state very unlikely to reverse back to a native one [4].

Small proteins with less than 100 amino acids reach their native conformation with a simple energy landscape and in a sub-second timescale[4-6]. However, larger proteins have a larger timescale to achieve the native conformation with many intermediate states. Depending on the energy of the intermediate states it can be easier or more difficult to fold back into the native structure[7]. Besides, these intermediate conformations may expose some key regions (aggregation-prone regions) that are required to trigger an aggregation event.

These aggregated conformations may work additionally as a template for further protein aggregation, unbalancing the system.

Polyglutamine Diseases

Giving the appropriate conditions, most proteins have the ability to self-assemble into amyloid fibrils, yet only an exclusive group of proteins appear to aggregate under physiological conditions[8,9].

A protein's ability to aggregate and form organized amyloid-like structures is affected by the amino acid sequence. Proteins with trinucleotide repeats, specifically containing polyglutamines (polyQ), are an extraordinary rarity in the self-assembly protein group. Glutamines are polar residues stabilized by solvent interaction, but it has been demonstrated that isolated polyQ peptides can form insoluble amyloid fibrils in solution[10]. Due to this fact, polyQ repeats are associated with some neurodegenerative disorders designated as polyglutamine diseases.

Polyglutamine expansion diseases constitute a group of hereditary neurodegenerative disorders caused by the expansion of CAG trinucleotide repeats above a certain threshold. The gene expansion is translated into a protein with an expanded polyQ tract.

There are at least nine different polyQ proteins associated with rare neurodegenerative disorders with a mean frequency of 1-10 cases per 100.000 people[11]: Huntingtin (Htt) in Huntington's disease (HD)[12]; ataxin-1 (Atx-1), ataxin-2 (Atx-2), ataxin-3 (Atx-3), voltage-dependent calcium channel α-1A subunit (CACNA1A), ataxin-7 (Atx-7) and TATA-binding protein (TBP) in Spinocerebellar Ataxias SCA1[12], SCA2[13], SCA3 (also called Machado-Joseph disease, MJD)[14], SCA6[15], SCA7[16] and SCA17[17]; atrophin-1 (Atn1) in Dentatorubral-Pallidoluysian Atrophy (DRPLA)[18,19] and Androgen Receptor (AR) in Spinal-Bulbal Muscular Atrophy (SBMA)[20].

Although the proteins related to these diseases share no homology besides the polyQ repeats[21] the expansion of the polyQ tract leads to their aggregation and specific accumulation in neuronal cells as inclusions, with consequent neuronal loss as well as

other physical and neurologic manifestations. Still, each polyQ disease exhibits specific symptoms which usually begin in mid-life and progress over 10 to 30 years, leading ultimately to the patient's death[22,23].

All polyQ diseases have a shared negative correlation between the age onset and the CAG repeats. A greater glutamine repeats number results in an earlier development of the disease. This shows that the glutamine tract plays a central role in the progression of the disease.

Some variability in the polyQ repeats length exists. However, expansion beyond a certain threshold, distinct for each polyQ protein (Table 1), enhances the propensity to form β-rich amyloid-like fibrils[24-28].

Table 1: Human diseases associated with CAG codon repeats adapted from[29].

Disease	Gene	Normal polyQ Repeats	Pathogenic polyQ repeats
Huntington's disease (HD)	HTT (Huntingtin)	6 – 34	36 – 121
Spinocerebellar ataxia Type 1 (SCA1)	ATXN1	6 – 39	40 – 82
Spinocerebellar ataxia Type 2 (SCA2)	ATXN2	15 – 24	32 – 200
Spinocerebellar ataxia Type 3 or Machado-Joseph disease (SCA3 or MJD)	ATXN3	10 – 51	55 – 87
Spinocerebellar ataxia Type 6 (SCA6)	CACNA1A	4 – 20	20 – 29
Spinocerebellar ataxia Type 7 (SCA7)	ATXN7	4 – 35	37 – 306
Spinocerebellar ataxia Type 17 (SCA17)	TBP	25 – 42	47 – 63
Dentatorubral-Pallidoluysian Atrophy (DRPLA)	ATN1	7 – 34	49 – 88
Spinal-Bulbal Muscular Atrophy (SBMA)	Androgen receptor on X chromosome	6 – 34	36 – 121

Machado-Joseph Disease

Machado-Joseph disease (MJD) was described in Portuguese descendants from the Azores islands[30-32] and corresponds to the most common autosomal dominant spinocerebellar ataxia and the second most frequent polyQ disease, after HD[33-35].

This neurodegenerative disease involves neuronal loss in selective brain regions, including the cerebellum (spinocerebellar pathways and dentate nucleus), brainstem, (pons and *medulla oblongata*) basal ganglia (*globus pallidus*, caudate and putamen, *substantia nigra*) and spinal cords[32,36-39]. Common features of MJD are progressive cerebellar ataxia, pyramidal signs, as well as ophthalmoplegia, dystonia, dysphagia and facial and speaking movement problems[40,41].

The gene responsible for the disease (MJD1 or ATX3) is mapped on the long arm of the chromosome 14, region 14q31.1[14]. In the case of MJD, the polyQ of Atx-3 of healthy individuals has up to 44 glutamines and repeats between 45 and 51 are associated with an incomplete penetrance of the disease[14,37,42]. It then manifests when the repeat length surpasses the threshold of 53 glutamines[43,44].

Ataxin-3 Architecture

Atx-3 is a multidomain protein with deubiquitinase (DUB) activity involved in central cellular processes, such as transcriptional regulation, signal transduction and cell quality control[45]. The protein is composed by a conserved globular domain at the N-terminal, the Josephin Domain, (JD, amino acids 1-170) (Figure 2, green box) and a flexible C-terminal tail[46]. The C-terminus comprehends two tandem ubiquitin-interacting motifs (UIM1-2) (Figure 2, yellow boxes) followed by the polyQ region of variable length (Figure 2, red box)[47]. Depending on the splicing variant, the C-terminal region has a third UIM (UIM3) (Figure 2, yellow box)[48].

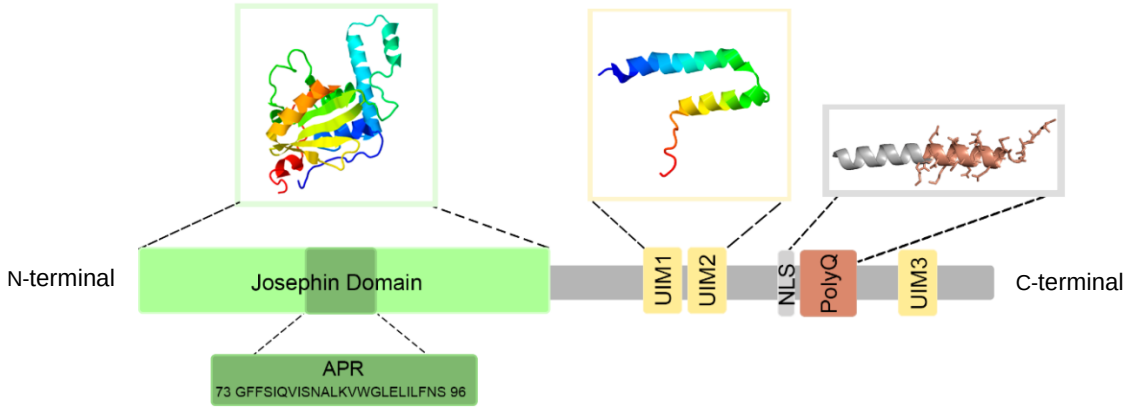

Figure 2: Representation of the domain architecture of Atx-3 evidencing the aggregation-prone region and the 3D atomic structures of some regions. Detailed representation of Atx-3 isoform UIM3 composed by the globular Josephin domain (JD – light green) evidencing the aggregation-prone region (APR – dark green) and the flexible C-terminal with three ubiquitin interaction motifs (UIM – yellow), a nuclear localization sequence (NLS – grey) and the expandable polyglutamine tail (polyQ – red). In the top of the scheme are cartoon representations of JD (PDB accession: 1YZB), UIM1-2 (PBD accession: 2KLZ) and the PolyQ tract (PDB accession: 4WTH).

The isoform containing the UIM3 is the predominant variant in the brain[49]. Finally, a nuclear localization signal (NLS) (Figure 2, in grey) is located upstream of the polyQ region[50].

The three-dimensional structure of Atx-3 has not been determined but there are structural information regarding some of its regions. The JD has a globular papain-like fold with a high α-helical content[46,51]. A catalytic triad is formed in the active site pocket by structurally conserved amino acids C14, H119, N134[52-54]. Structures of the UIM1-2 region revealed a α-helical conformation induced by the presence of ubiquitin[55]. Crystal structures of the C-terminus with a small segment of the polyQ expansion show some evidence of the conformation flexibility of this region[56]. PolyQ expansion does not mediate global structural changes, only local conformational changes have been detected. These subtle changes may be the cause for faster aggregation observed in expanded Atx-3[24,51,57,58].

Ataxin-3 Aggregation Pathway

PolyQ expansion disorders are linked to the formation of extracellular amyloid deposits or intracellular inclusions with amyloid-like characteristics[25,59].

Both non-expanded Atx-3 and the isolated JD have an intrinsic propensity to self-assemble and form amyloid-like fibrils, demonstrating a polyQ-independent aggregation process[58,60-62]. Some specific regions of JD are responsible for triggering the aggregation. These aggregation-prone regions (APRs) can be predicted by bioinformatic analysis of the protein sequence. [63-75] The APRs of Atx-3 are located between residues 73 and 96 (Figure 2, dark green box). This was experimentally validated using limited proteolysis and mass spectrometry by Scarff and colleagues[58].

Usually, these APR are hidden in hydrophobic regions inside the protein preventing the start of aggregation. However, mutations such as the polyQ expansion increase the probability of these APR becoming exposed to the solvent. A two-step process was proposed for the aggregation of Atx-3. The first one is mediated by the APR of JD (independent of the polyQ tract) followed by a second step that is related to the polyQ expansion which results in mature SDS-resistant fibrils[58,76]. Aggregation of Atx-3 starts with a self-assembly of JD. Self-association initiates by exposure of the APR (amino acid 73 to 96) in the globular domain (Figure 2 and Figure 3, dark green)[58]. In solution, the JD is in a conformational equilibrium and the APR may become exposed, initiating the aggregation process. The increased rate of aggregation in expanded Atx-3 can be explained by dynamic fluctuations that expose the APR more frequently[57,58].

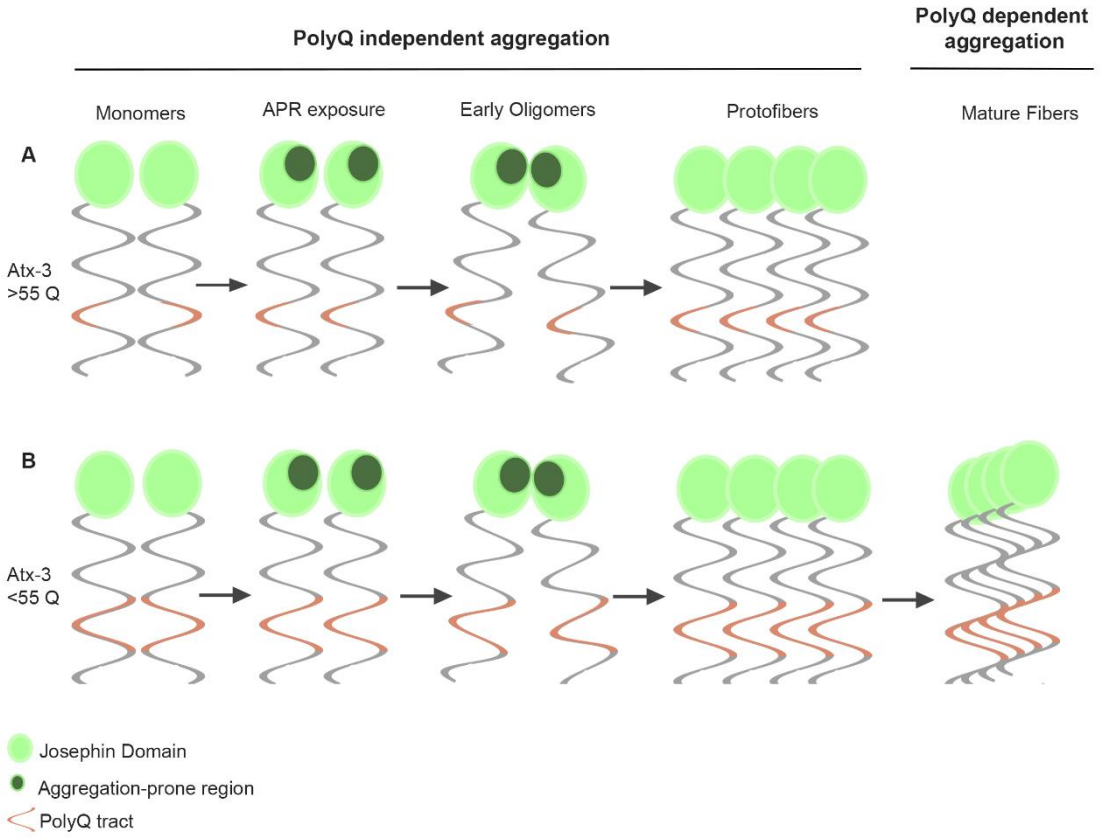

Figure 3: Model of the mechanism of fibril formation of non-expanded and pathogenic Atx-3. The equilibrium conformation in the JD leads (sporadically) to the exposure of its APR. The polyQ expansion increases the likelihood of this exposure resulting in a faster aggregation. This leads to the formation of dimers creating a template for further monomer addition, ultimately creating protofibrils. In non-expanded polyQ these protofibrils are SDS-sensitive. In the case of expanded Atx-3 the polyQ region can then interact by hydrogen bonds and form mature fibrils that are SDS resistant. Adapted from[58].

Self-assembly of monomers by the JD region leads to the formation of compact dimers that function as a nucleation point for the Atx-3 sequential monomer addition, resulting in the formation of elongated SDS-sensitive amyloid protofibrils (Figure 3A)[58].

Up to this point, the process in entirely independent of the polyQ tract and occurs in both normal and pathological Atx-3. The second stage of the aggregation mechanism involves only the expanded Atx-3 with the polyQ tract producing SDS-resistant mature amyloid fibrils (Figure 3B). These amyloids fibrils are stabilized by the hydrogen bonds involving the glutamine side-chains[76,77].

The role of the UIMs in the two steps of aggregation is still under study. The isolated form of UIM1-2 does not aggregate, but the aggregation rate of JD is accelerated by its presence. These regions promote an electrostatic interaction between themselves, approximating the JD's APRs to each other[78]. The presence of these APRs is not unique in Atx-3. In other polyQ proteins such as Atx-1 and Htt these regions have also been identified[79-83].

PolyQ Proteins Oligomeric Species

The accumulation of aggregated protein into insoluble amyloid deposits is the hallmark for several neurodegenerative disorders such as the polyQ diseases[84] . In fact, the process of monomeric polyQ protein self-assembly into amyloid fibrils is being extensively studied (Figure 4A)[10,85,86]. The mechanism of amyloid formation occurs via a nucleation-dependent growth by a polymerization mechanism[86-88]. The global polymerization rate depends on three stages: a slow nucleation phase (lag phase) involving a thermodynamically unfavorable transition from the native form to a non--native conformation which is then followed by its elongation. The latter happens by the exponential addition of fibril-precursors extending the fibril form (elongation phase). After elongation, there is a dynamic equilibrium in the amount of fibrils in the stationary phase.

However, beyond the formation of fibrillar aggregates, cells also accumulate a variety of morphologically distinct species (Figure 4). Besides the aggregation process starting directly from a monomeric conformation (Figure 4A) the aggregation can also start from intermediary soluble oligomers that need structural reorganization to form fibrils (Figure 4B).[89-92] The aforementioned mechanisms may occur simultaneously. Other intermediary species such as annular aggregates may also form (in- or off- pathway[93]), leading to final amorphous aggregates (Figure 4C). All these aggregated structures can accumulate and form large inclusions[93]. The fact that the endpoint structure is an agglomerate of aggregated species makes it very difficult to determine exactly which species is the toxic one.

Neurotoxicity may be caused by the modification of regular function of the polyQ protein by the polyQ expansion[94] and/or from the presence of toxic intermediate oligomers[95-99]. There is evidence that these intermediate oligomers interact with macromolecules present in the cells leading to a pronounced toxicity and amyloid fibrils work as a protection mechanism against these aberrant interactions[100-103].

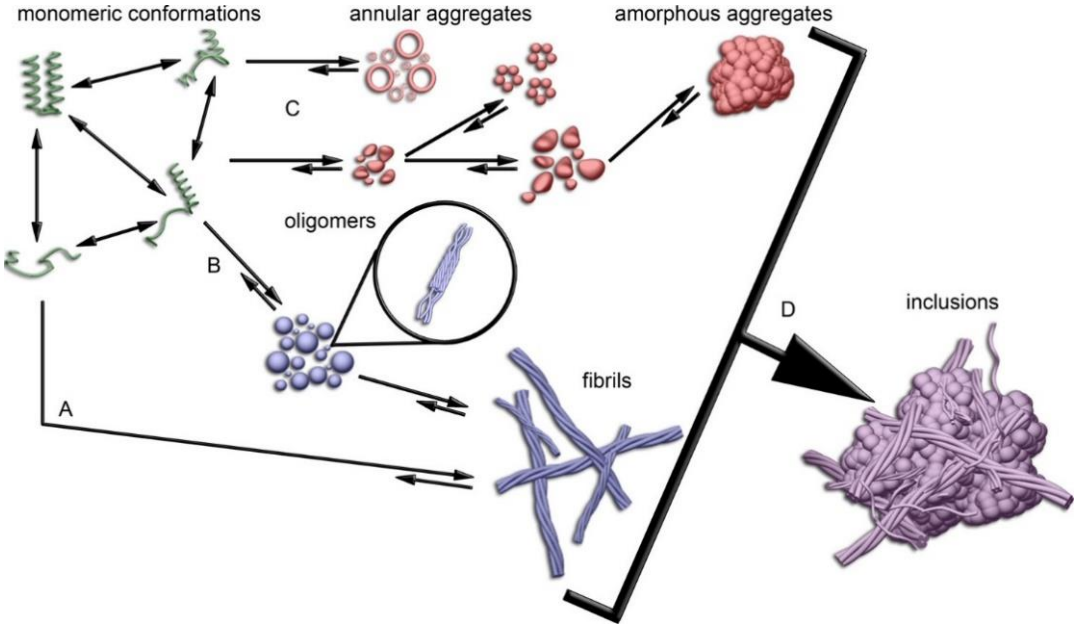

Figure 4: Schematic model of misfolded and aggregated protein with polyQ expansions. Monomeric protein assembles into inclusion bodies through distinct conformers on-pathway (in blue) or off-pathway (in red) to fibril formation. A) monomeric addition leading directly to fibril formation; B) fibril formation via oligomeric intermediates, (both mechanisms A and B can happen simultaneously); C) Off-pathway mechanism with different sized oligomers as annular aggregates and large amorphous structures. D) All these aggregated structures may accumulate and form large inclusions.[93]

Modulation of Atx-3 Aggregation by Molecular Partners

Besides the APRs and the polyQ region post-translational modifications (PTMs) can also mediate Atx-3 aggregation[104,105]. Additionally, aggregation may also be regulated by the presence of molecular partners[29,106]. Interaction of these with the polyQ or the APR may prevent the aggregation self-assembly but can also increase its rate and toxicity[107,108]. The protective effect is mediated by the interaction of said partners at or near the aggregation-prone region shielding the self-assembly sequences. Atx-3 JD also binds to ubiquitin besides UIM1 and UIM2 and due to the proximity of the APR this interaction delays the self-assembly[47,52,109]. Another example of this kind of modulation of aggregation is the interaction with the small heat shock protein alphaB-crystallin (αB-c) which modulates the first step of aggregation (independent of polyQ)[110].

Some small peptides show the ability of inhibiting aggregation in amylogenic diseases but since these peptides also contain short polyQ sequences they have the risk of accelerating Atx-3 aggregation and enhancing its toxicity. So, new strategies need to be developed.[111]

Nanobodies

Antibodies such as conventional Immunoglobulin G (IgG) have been extensively used for the development of new therapies. IgG are tetramers of 150 kDa consisting on two identical heavy chains (50 kDa each) and 2 identical light chains (25 kDa each), linked by disulfide bonds[112]. However, there are some undesirable features related with their application, such as high production costs, large size and instability, prompting a search for new solutions.

While the molecular structure of antibodies among mammals is highly conserved, small variations have been found. A good example is the heavy chain antibody, found in llamas and other camelids (camel, dromedary, vicuña, gunaco), which only exhibits a heavy chain, as the name suggests[113]. Like conventional antibodies (Figure 5A), heavy chain antibodies (Figure 5B) also possess a VH fragment which in this case is called V_HH (variable domain of heavy chain antibody), responsible for epitope recognition. V_HH can be cloned and recombinantly expressed as the smallest form of an antibody (≈ 15 kDa), thus being referred to as nanobody (NB) [114].

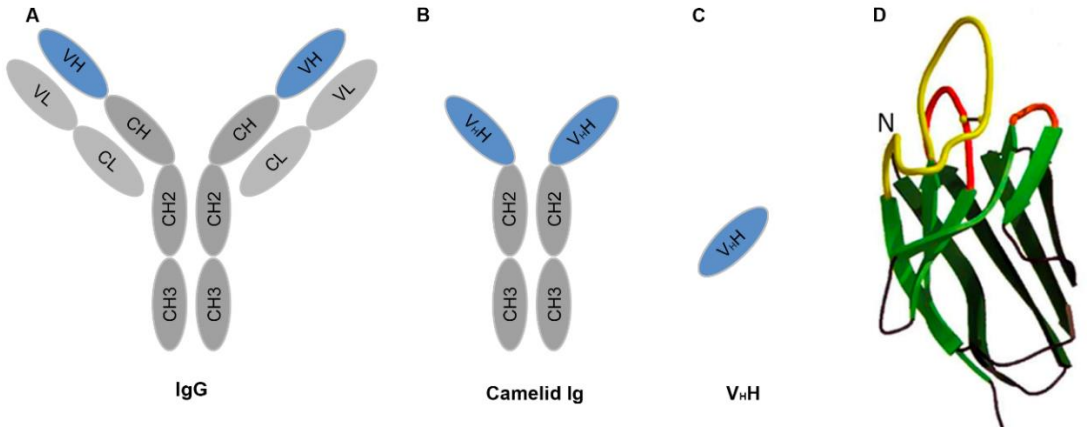

Figure 5: Schematic representation of a conventional antibody, a heavy chain antibody from Camelidae and a Nanobody. A) Schematic representation of an IgG antibody and its segments. B) Schematic representation of a heavy-chain antibody and its segments. C) Isolated variable heavy chain (V_HH), or NB, from camelid Ig. D) X-ray structure of a V_HH fragment. The complementarity determining regions (CDR) 1, 2 and 3 are shown in red, orange and yellow, respectively. The stick between CDR3 and CDR1 indicates a disulfide bond connecting these two regions.[115] CH (constant heavy chain), CL (constant light chain), VH (variable heavy chain) and VL (variable light chain).

The loop of NBs complementarity determining region 3 (CDR3) (Figure 5C and 5D) is more extended than in the usual antibodies and folds over the hydrophobic amino acids in the surface increasing its solubility[116]. Additionally, they present the same specificity of binding as a regular antibody[117].

NBs are easily expressed in *E. coli* as periplasmic proteins with a high yield. They are highly resistant to high temperatures and to pH variations. With these characteristics, they are an excellent tool to apply in both research and therapy[118,119].

Applications of Nanobodies

Due to all the characteristics just mentioned and their low molecular weight, low toxicity, reduced immunogenicity and high affinity, NBs can be applied in distinct fields of research. The applicability of NBs in crystallography as crystallization chaperones (stabilizing a conformation of the protein) has been noted: it was possible to obtain structures such as transient multiprotein assemblies[120-123], membrane proteins[120,124-126] and intrinsically disordered proteins[127,128] with the use of these molecules.

NB have also proved to be a successful application in neurodegenerative disorders research. In this case, NBs are used to modulate the amyloid formation process and as a probe to study the intermediates formed during aggregation[129,130].

The ability of these antibodies to work as an anti-aggregation molecule has already been studied in amyloid disorders as the Huntington's disease and in Parkinson's disease: In Parkinson's, NBs inhibited the formation of fibrils promoting a rapid conformational conversion into a less stable oligomer, reducing the oligomer-induced cellular toxicity[131]. Regarding Huntington's, studies showed that the application of antibodies in the N-terminal region of Huntingtin can modulate the aggregation mechanism both *in vivo* and *in vitro*[132-134]. The application of NBs in amyloid related diseases is therefore considered a promising in the study of aggregation inhibition.

Objectives

Several studies have been recently performed to understand the mechanism of aggregation of Ataxin-3 (Atx-3) and its potential as the main target for the therapy of Machado-Joseph disease, which is still undeveloped. It has been demonstrated that interacting partners such as ubiquitin have the ability to bind Atx-3 near the aggregation--prone region (APR) and increase the lag phase of aggregation. The main intention of this work was to select successful Atx-3-binding molecules with a role in the modulation of Atx-3 aggregation. To achieve this goal four objectives were defined: 1) To express and purify 18 nanobodies raised against the Josephin domain of Atx-3 and pre-select successful Atx-3-binding candidates; 2) To characterize the molecular details of the selected NBs binding to Atx-3 by determination of the binding affinities, the Atx-3:NB complexes stoichiometry and the NBs binding site on Atx-3; 3) To evaluate the crystallization chaperon properties of the NBs on Atx-3; 4) To study their impact on the modulation of Atx-3 aggregation process.

We wanted to address distinct questions. Is the binding of the NB specific to a single region of Atx-3? Do the NBs have an impact on the structure of Atx-3? Can these NBs increase the lag phase of Atx-3 aggregation, delaying the whole process and change the species formed in solution? Also, how do the NBs affect the toxicity of the oligomeric species and what is their potential as a therapeutic tool of MJD? Additionally, the ability of these NBs to work as a crystallization chaperone was explored in crystallization trials for Atx-3 hoping that the stabilization of an Atx-3 conformation would help the crystallization process.

To fulfill the objectives a set of experiments was designed using the following techniques: Isothermal Titration Calorimetry (ITC), Dynamic Light Scattering (DLS) and Small Angle X-ray Scattering (SAXS). To explore the pharmaceutical potential of the NBs in the aggregation process of Atx-3 and subsequent implications in the therapeutic research on Machado-Joseph disease we performed an Atx-3 aggregation time course with and without the presence of NBs as well as a fluorescence assay coupled with size exclusion chromatography and DLS. To assess the toxicity of the species formed at the endpoint of aggregation, samples were examined using Transmission Electron Microscopy, Dot-blot and a Filter Retardation Assay.

Material and Methods

Reagents

Media:

Luria-Bertani solid medium (LB): 1 % (w/v) tryptone, 0.5 % (w/v) yeast extract, 1 % (w/v) sodium chloride (NaCl), 1.5 % (w/v) of agar.

Luria-Bertani broth medium with low osmolarity (LB-ON): 1 % (w/v) tryptone, 0.5 % (w/v) yeast extract.

Terrific Broth (TB): 1.2 % (w/v) tryptone, 2.4 % (w/v) yeast extract, 0.4 % (w/v) glycerol, 0.23 % (w/v) potassium phosphate monobasic (KH_2PO_4), 1.64 % (w/v) potassium phosphate dibasic (K_2HPO_4).

Super Optimal Broth (SOB): 2 % (w/v) Tryptone peptone, 0.5 % (w/v) yeast, 0.05 % (w/v) (NaCl) and 0.0186 % (w/v) potassium chloride (KCl).

Buffers:

Ataxin-3 purification buffers

Cell lysis buffer: 20 mM sodium phosphate pH 7.5, 500 mM NaCl, 2.5 % (w/v) glycerol, 20 mM imidazole, 50 μg/mL lysozyme, 50 μg/mL desoxirribonuclease (DNase) I, 10 mM magnesium chloride ($MgCl_2$) and 10 mM phenylmethylsulfonyl fluoride (PMSF).

Ni^{2+}-charged HisTrap buffer A: 20 mM sodium phosphate pH 7.5, 500 mM NaCl, 2.5 % (w/v) glycerol, 20 mM imidazole.

Ni^{2+}-charged HisTrap buffer B: 20 mM sodium phosphate pH 7.5, 500 mM NaCl, 2.5 % (w/v) glycerol, 500 mM imidazole.

Gel filtration buffer: 20 mM sodium phosphate pH 7.5, 150 mM NaCl, 5 % (w/v) glycerol, 2 mM EDTA, 1 mM dithiothreitol (DTT).

Nanobody purification buffers

Cell lysis buffer: 0.2 M Tris pH 8.0, 0.5 M sucrose and EDTA-free protease inhibitor tablets (Thermo Fisher Scientific).

Ni^{2+}-charged HisTrap Buffer A: 50 mM sodium phosphate pH 7.0, 500 mM NaCl.

Ni^{2+}-charged HisTrap Buffer B: 50 mM sodium phosphate pH 7.0, 500 mM NaCl, 300 mM imidazole.

Gel filtration buffer: 50 mM sodium phosphate pH 7.5, 150 mM NaCl.

Ataxin-3 aggregation buffer: 20 mM sodium phosphate pH 7.5, 150 mM NaCl, 1 mM DTT.

Isothermal Titration Calorimetry (ITC) buffer: 20 mM sodium phosphate pH 7.5, 150 mM NaCl, 1 mM TCEP.

Bacterial Strains

Table 2: List of Bacterial Strains and its genotype for plasmid replication (*E. coli* DH5α) and for Atx-3 variants (*E. coli* BL21-SI) and NBs (*E. coli* WK6 (su-)) recombinant protein expression.

Bacterial Strain	Application	Genotype
E. coli DH5α (Invitrogen)	Plasmid replication	F- endA1 glnV44 thi-1 recA1 relA1 gyrA96 Φ80dlacZΔM15 deoR Δ(lacZYA-argF) U169 nupG, hsdR17(rK- mK+), λ–
E. coli BL21-SI (Stratagene)	Protein expression (Atx-3)	F- ompTIon $hsdS_B$ (r_B-, m_B-) gal dcm endA1 proUp::T7 RNAP::malQ-lacZ (Tet^S)
E. coli WK6 (su-) (Instruct)	Protein expression (NB)	Δ lac-proAB), galE, strA/F' $lacI^q$,lacZΔM15, $proA^+B^+$]

Plasmids

Table 3: List of plasmids for Atx-3 and NBs expression with inductor and antibiotic resistance.

Atx-3 JD	pDEST17/J1-1	Induction: 2xLB; 3M NaCl Resistance: Ampicilin
Atx-3 D1	pDEST17_His6_Atx-3 D1	
Atx-3 13Q	pDEST17_TevG_Atx-3 13Q	
Atx-3 77Q	pDEST17_TevG_Atx-3 77Q	
NBs	Info: GenBank KF415192 pMESy4	Induction: 1mM IPTG Resistance: Ampicilin

Truncated variants and isoforms are displayed in Figure 6.

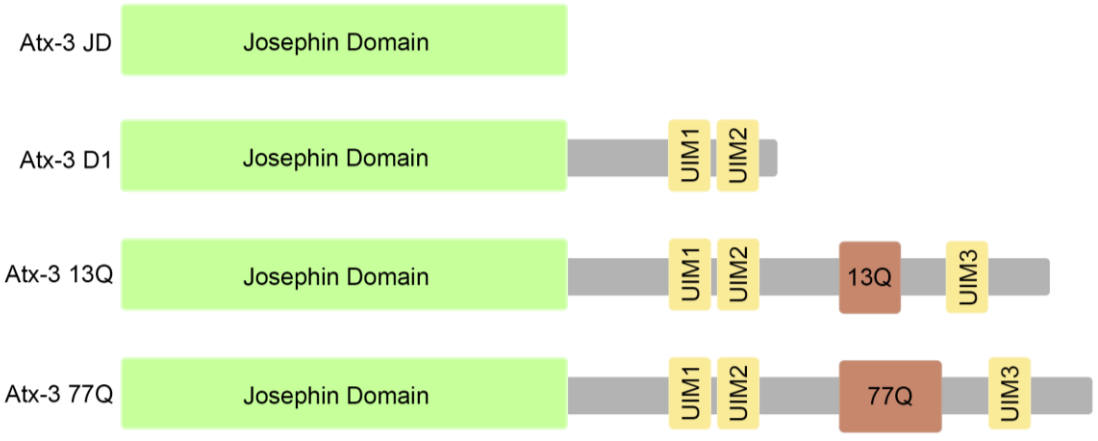

Figure 6: Representation of Atx-3 isoforms and truncation variants used in this study. The globular JD (Atx-3 JD), the JD followed by two tandem ubiquitin interaction motifs (UIM1-2) (Atx-3 D1), the non-pathological full-length protein containing 13 glutamines (Atx-3 13Q) and a pathological isoform with an expansion of polyglutamine tract to 77 glutamines (Atx-3 77Q).

In collaboration with European Instruct Platform Nanobodies4Instruc, conformational NBs against ataxin-3 (Atx-3) were produced by immunization of llamas with the Josephin domain (JD) of Atx-3[135]. The specificity of the NBs was tested by ELISA, and a total of 18 Atx-3-binding NBs were selected for further studies.

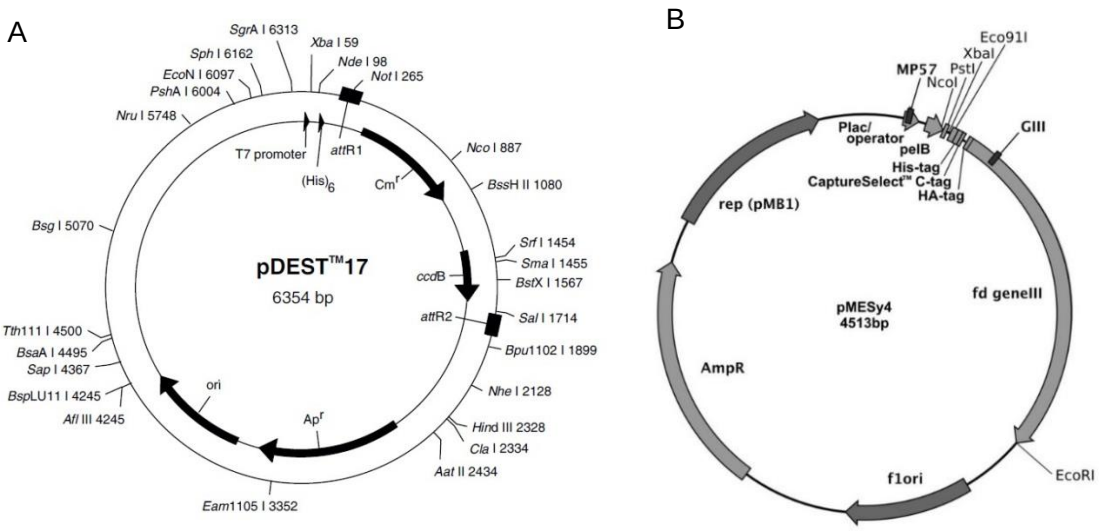

Figure 7: Plasmid representation. A) Ataxin-3 variants plasmid (pDEST17) with T7 promotor, 6x HIS/TEVg and the gene conferring ampicillin resistance (AmpR). B) NBs plasmid (pMESy4), with a lac promotor (Plac/operator) and the Amp resistance gene (AmpR). The NB sequence is inserted in the pMESy4 plasmid between the pelB sequence (periplasm secretion signal) and a 6xHis-tag.

Antibodies

Table 4: Primary and secondary antibodies. Primary antibodies: 1H9 recognizes Atx-3 at the residues E214-L233, anti-OC recognizes amyloid fibrils/protofibrils, Anti-A11 is a conformational antibody that recognizes toxic oligomers. Secondary antibodies anti-mouse and anti-Rabbit with its concentration and incubation conditions.

Primary antibody:	Host	Dilution	Incubation
Anti-Atx-3 1H9 (MAB5360, Millipore)	Mouse	1:20.000 TBS-T 3% BSA	2h, RT
Anti-Amyloid Fibrils OC[136] (AB2286, Millipore)	Rabbit	1:50.000 TBS-T, 3% BSA	ON, 4 ºC
Anti-Amyloid Oligomer A11[137] (AB9234, Millipore)	Rabbit	1:000 TBS-T, 3% BSA	1h, RT

Secondary antibody	Host	Dilution	Incubation
Anti-Rabbit HRP (A6154, Sigma-Aldrich)	Mouse	1:10.000 TBS-T, 3% BSA	1h, RT
Anti-Mouse HRP (A4416, Sigma-Aldrich)	Rabbit	1:10.000 TBS-T, 3% BSA	1h, RT

Preparation of competent cells

E. coli cells (DH5α, BL21-SI and WK6(Su-)) were inoculated on a plate containing LB medium and grown overnight (ON) at 37 ºC (INCU-line, VWR). An isolated colony was picked and inoculated in 30 mL of LB medium at 37 ºC, 250 rpm for 6-8 hours (Shaker, IKA). Then 1 mL of the grown culture was inoculated in 250 mL of SOB and left ON at 18 ºC and 200 rpm (Shaker, IKA). When the culture reached OD_{600} 0.6 the culture was kept in ice for 10 min and harvested at 2500 xg (Sorvall ST 40, Thermo Fisher Scientific), 10 min, 4 ºC. The pellet was carefully resuspended in transformation buffer (0.238 % HEPES, 0.22 % $CaCl_2.2H_2O$, 1.864 % KCl at pH 6.7 and 1.09 % of $MnCl_2.4H_2O$), kept on ice during 10 min and harvested again at 2500 xg, 10 min, 4 ºC. The pellet was resuspended in transformation buffer and 1.5 mL of dimethyl sulfoxide (DMSO) were added drop by drop and kept during 10 min on ice. Aliquots of 200 μL were frozen and stored at -80 ºC.

Transformation of competent cells with plasmid DNA

100 ng of plasmid DNA was added to 50 μL of competent cells and incubated on ice for 30 minutes. Afterwards, the mix suffered a heat shock treatment for 45 sec at 42 ºC, followed by a cold-shock during 10 min on ice. After that, 500 μL of LB-ON medium was added, and the suspension was incubated at 37 ºC for 1 hour at 180 rpm (Shaker, IKA). The cells were then plated on LB-ON solid medium supplemented with ampicillin 100 mg/L and incubated ON at 37 ºC (Sigma-Aldrich).

This procedure was followed by a plasmid DNA replication or a recombinant protein expression protocol as detailed below.

Plasmid DNA Replication

For plasmid DNA replication *E. coli* DH5α cells were used. An isolated colony of transformed cells was inoculated in 20 mL LB liquid medium and incubated ON at 37 ºC, 180 rpm (Shaker, IKA). The next day, the cells were harvested at 3500 xg, 10 min (Avanti J-26 XP - Rotor J-LITE JLA 8.1000, Beckman-Coulter) and the plasmid purification was performed using the commercial NZYMiniprep Kit (NZYtech – Gene and Enzymes) and following the manufacturer's protocol. The plasmid concentration was determined at measuring the absorbance at 260 nm using the Nanodrop (Thermo Fisher Scientific). To detect any possible mutation during the replication process, nucleotide sequences of NBs were confirmed by direct sequencing of the plasmids (LightRun, GATC biotech).

Recombinant Protein Expression

For the expression of Atx-3 and of the NBs *E. coli* BL21-SI and WK6(su-) cells, respectively, were used. BL21-SI cells were transformed with pDEST17 plasmid expressing 6His-Atx-3 (Atx-3 JD, Atx-3 D1 domain, full length Atx-3 13Q and expanded Atx-3 77Q). WK6(su-) were transformed with pMESy4 plasmid expressing 6His-NB.

4 to 5 colonies of the transformed *E. coli* BL21-SI cells were resuspended in 500 μL of LB-ON medium and 100 μL of inoculum was plated on LB-ON solid medium supplemented with 100 mg/L ampicillin (Sigma-Aldrich, USA) and incubated overnight at 37 ºC (INCU-line, VWR) for truncated and isoforms of Atx-3. The same procedure was used for the expression of NBs with the only exception being the use of LB media instead.

Expression of Ataxin-3 Variants

The bacterial film formed ON in the agar plate was collected with a sterile incubation loop, inoculated on 500 mL LB-ON medium supplemented with 100 mg/L ampicillin and 0.4 % (w/v) glucose and grown at 37 ºC, 180 rpm until the OD_{600} 0.6-0.8. The culture was then cooled to 30 °C and protein expression induced with 300 mM NaCl. After 3 hours of expression, the cells were harvested by centrifugation (Avanti J-26 XP - Rotor J-LITE JLA 8.1000, Beckman-Coulter), resuspended in Atx-3 lysis buffer and frozen at -20 ºC.

Nanobody Expression

The bacterial film formed overnight on the agar plate collected and inoculated on 500 mL of TB medium supplemented with 100 mg/L ampicillin at 37 ºC, 180 rpm (Shaker, IKA) until the OD_{600} 0.8–1.0. At this point the NB overexpression was induced with isopropyl β-D-1-thiogalactopyranoside (IPTG) at a final concentration of 1 mM and the medium as further supplemented with ampicillin (100 mg/L). Different expression conditions were tested, namely 3 hours at 37 ºC (selected condition), overnight at 28 ºC and overnight at 25 ºC. After 3 h expression the cells were harvested by centrifugation at 4 000 xg, 25 min, 4 ºC (Avanti J-26 XP - Rotor J-LITE JLA 8.1000, Beckman-Coulter) resuspended in NB cell lysis buffer and frozen at -20 ºC.

Recombinant Protein Purification

Ataxin-3 variants purification

Before purification, 1 mM of PMSF, 20 μg/mL DNase I (from bovine pancreas, Sigma-Aldrich) and 1 mM $MgCl_2$ were added to the cells and these were disrupted by stirring 1 hour on ice. The supernatant obtained after centrifugation was loaded into a pre-equilibrated (with Atx-3 buffer A) Ni^{2+}-charged HisTrap column (GE Healthcare Life Sciences) and protein was eluted with a gradient of imidazole (50 mM, 250 mM and 500 mM). Atx-3 eluted with 250 mM of imidazole was applied into a HiPrep 26/60 Sephacryl S-200 HR column (GE Healthcare Life Sciences) equilibrated in Atx-3 gel filtration buffer and eluted with a flow rate of 2 mL/min. After SDS-PAGE analysis, fractions corresponding to pure Atx-3 were pooled and concentrated on Amicon Ultra-15 (cut-off 10 kDa) centrifuge filter (Millipore) to 20-30 mg/mL. After concentration, the protein was centrifuged for 15 min at 15,000 rpm at 4 ºC (Himac CT 15 RE, VWR), aliquoted, frozen in liquid nitrogen and stored at -80 ºC.

Nanobody Purification

Overexpressed cells were thawed and left stirring during one hour in NB cell lysis buffer. The soluble fraction was separated from the insoluble fraction by centrifugation (14 000rpm, 45 min, 4 ºC (Avanti J-26 XP - Rotor J-LITE JA 25.50, Beckman-Coulter)). The supernatant obtained after centrifugation was loaded onto a pre-equilibrated (with NB Buffer A) Ni^{2+}-charged HisTrap column (GE Healthcare Life Sciences) and NB was eluted with a single elution step containing 300 mM of imidazole. Eluted protein was applied to a Hiprep 26/60 Sephacryl S-100 HR column (GE – Healthcare Life Science) equilibrated in NB gel filtration buffer and eluted with a flow rate of 2 mL/min. After SDS--PAGE analysis, fractions corresponding to pure NB were pooled and concentrated on Amicon Ultra-15 (cut-off 3 kDa) centrifuge filter (Millipore) to 20-30 mg/mL. After concentration, the protein was centrifuged for 15 min at 15,000 rpm at 4 ºC (Himac CT 15 RE, VWR), aliquoted, frozen in liquid nitrogen and stored at -80 ºC.

SDS-PAGE

During the expression and purification process (and for other studies) samples were collected to verify the protein expression levels and possible contaminants by conducting a sodium dodecyl sulfate polyacrylamide gel electrophoresis (SDS-PAGE) analysis. The composition of the SDS-PAGE gel is mentioned below. Each gel was run at 30 mV.

Table 5: SDS-PAGE preparation. Resolving and Stacking gel preparation

Resolving Gel (12.5 %)	Stacking Gel (4 %)
2.25 mL H_2O	1.78 mL H_2O
2.15 mL 1M Tris pH 8.8	0.71 mL 1M Tris pH 8.8
2.06 mL 40% acrylamide	0.28 mL 40% acrylamide
65.2 µL 20% SDS	28 µL 20% SDS
65.2 µL 10% APS	28 µL 10% APS
6.52 µL TEMED	2.8 µL TEMED

SDS-PAGE MARKER: Unstained SDS-PAGE protein ladder standards with the corresponding molecular weight (Bio-Rad).

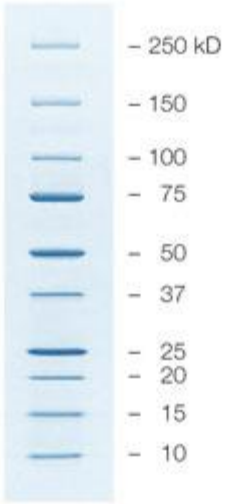

Figure 8: Unstained protein marker: unstained precision Plus protein ladder standard with the respective markers molecular weight.

Protein Concentration

Protein concentration was determined by measuring the absorbance at 280 nm with a Nanodrop spectrophotometer (Thermo Fisher Scientific) and using the protein extinction coefficient determined from the amino acid sequence (values for Atx-3 and NBs are displayed in Appendix).

Nanobody Selection

After the expression and purification process of all NBs that were produced against the JD, a screening was made in order to select the most promising ones. With this purpose, a pull-down assay was performed using Atx-3 13Q (full length) as bait protein followed by a size exclusion chromatography step to confirm the previous results, but in this case, using all four Atx-3 variants.

Pull-Down Assay

To select the Atx-3 interacting NBs a pull-down assay was performed.

0.50 μM of Atx-3 13Q was incubated with 0.50 μM of each, previously purified, NB for 30 min at 4 ºC in 500 μL of interaction buffer (20 mM sodium phosphate pH 7.5, 150 mM NaCl, 5 % glycerol, 2 mM EDTA, 1 mM DTT). Afterwards, 1 μL of anti-Atx-3 1H9 antibody was added to the mix for 45 min at 4 ºC (this antibody recognizes the E214-L233 epitope within the UIM1 of Atx-3). Subsequently, the mix was added to 20 μL of protein G Sepharose 4 fast flow beads (GE Healthcare Life Sciences) previously washed with interaction buffer.

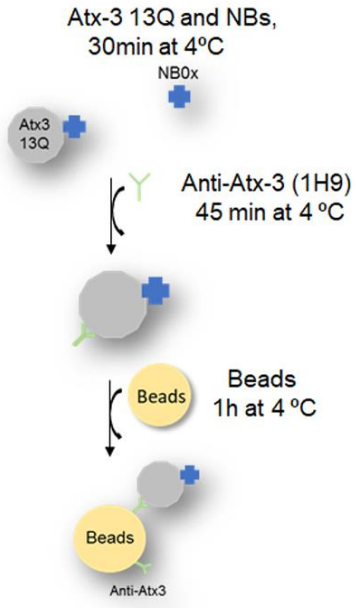

Figure 9: Pull-Down experiment scheme carried out to select the most promising NBs for further studies. First Atx-3 was incubated with different NBs for 30 min. After that Anti-Atx-3 13Q 1H9 HRP antibody was added for 45 min binding to the sepharose beads ensuring the pull-down.

The protein G Sepharose 4 fast flow beads bind to the Fc (fragment crystalliable) region of IgG proteins, in this case to anti-Atx-3 1H9 antibody. The latter binds to the Atx-3 13Q, which may interact with the NB leading to its pull-down. (Protocol scheme in Figure 9). After incubation for 1 h at 4 ºC the mixture was centrifuged at 3,000 rpm (Himac CT 15 RE, VWR) for 1 min. The supernatant was removed, and the beads were washed with interaction buffer (4x) to ensure the removal of any unspecific interaction. Then, 10 μL of loading buffer was added to beads and the mix was boiled for 10 min, centrifuged at 15,000 xg for 10 min (Himac CT 15 RE, VWR), and 10 μL of each sample was loaded into an SDS-PAGE gel along with the appropriate controls.

Size Exclusion Chromatography

Size Exclusion Chromatography (SEC) was performed to validate the Atx-3 binding NBs pre-selected in the pull-down assay detailed above. In this assay all four variants of Atx-3 (Atx-3 JD, Atx-3 D1, Atx-3 13Q and Atx-3 77Q) were used. 20 μM of Atx-3 protein was added to 40 μM of NB (1:2 ratio). After 90 min of incubation of the Atx-3 isoform with the NB, on ice, the sample was separated in a Superdex 200 increase 5/150 GL column (GE Healthcare Life Sciences), pre-equilibrated with interaction buffer, at a flow rate of 0.3 mL/min. 200 μL fractions were collected and stored for subsequent SDS-PAGE analysis. As control, the isolated proteins were also applied to the column.

Complex Characterization (Atx-3:NBs)

Combining the information obtained in the pull-down assay and in the SEC, four distinct NBs were selected for further biophysical and structural characterization. In order to map the binding sites of the NBs on Atx-3 four different Atx-3 variants were used (Figure 6).

To characterize the interaction between each isoform and the NBs a set of experiments was carried out: Isothermal Titration Calorimetry (ITC), Dynamic Light Scattering (DLS), Small Angle X-ray Scattering (SAXS) and Thermal Shift Assay.

Isothermal Titration Calorimetry

The Isothermal Titration Calorimetry (ITC) technique allows the determination of the binding affinity and the thermodynamic parameters of an interaction between two molecules. The binding affinity (K_D), the stoichiometry of the reaction (n) and thermodynamic parameters such as enthalpy (ΔH) and entropic factor ($-T\Delta S$) are calculated by measuring the heat released or consumed during the interaction, providing a thermodynamic profile.

The measurements of the interaction between Atx-3 variants and the NBs were performed at 20 ºC by using a MicroCal VP-ITC calorimeter (GE Healthcare Life Sciences). All proteins were dialyzed twice against 1 L of ITC buffer, first for 4 hours and then overnight using a 3 kDa cut-off dialysis membrane (Spectrum). After dialysis, the protein was filtered on centrifugal filters 0.22 μm (Ultrafree, Millipore) by centrifugation for 2 min at 12,000 rpm, 4 ºC (Himac CT 15 RE, VWR) to ensure the removal of putative protein aggregates.

The calorimeter cell sample (1.4 mL) was loaded with approximately 10 μM of each Atx-3 isoform. The titration assay was carried out by sequential 8 μL injection of

NB (200 μM) with 7 min intervals. All titration assays were performed in triplicate except for Atx-3 JD isoform, which were only performed once.

Titration data were analyzed using the Origin 7.0 program from MicroCal in order to obtain a non-linear regression using a single binding site model. The heat generated due to dilution of the titrant (NBs) was subtracted with a baseline correction.

Dynamic Light Scattering

Dynamic Light Scattering (DLS) was used to evaluate changes in the molecular size of particles in solutions of isolated Atx-3 variants and Atx-3 complexes with NB01.

DLS was preceded by the purification of Atx-3:NB01 complex by SEC. First, each isoform of Atx-3 (0.24 mM) was incubated with NB01 (0.48 mM), in a ratio of 1:2, for 90 min on ice. After that, the complex was loaded into a SEC column (Superdex 200 increase 5/150 GL, GE Healthcare Life Sciences) pre-equilibrated with interaction buffer (20 mM sodium phosphate pH 7.5, 150 mM NaCl, 5% glycerol, 2 mM EDTA, 1 mM DTT) at a flow rate of 0.3 mL/min. Fractions corresponding to the peak of Atx-3:NB01 complex were analyzed by DLS. The measurement was performed in triplicates using a Zetasizer Nano ZS (Malvern) in a quartz cuvette at 20 ºC with a count rate of 390.1 kcps. DLS results were visualized using the Zetasizer software 7.11.

Small Angle X-ray Scattering

Size Exclusion Chromatography in line with Small Angle X-ray Scattering (SEC-SAXS) was applied to study differences in the shape of Atx-3 13Q:NB01 complex in solution. SEC-SAXS data were collected at the BM29 BioSAXS beamline in the European Synchrotron Radiation Facility (ESRF, Grenoble) at a wavelength of 0.9919 Å.

100 μL samples of Atx-3 13Q at 10 mg/mL, NB01 at 10 mg/mL, and complexes of 10 mg/mL of Atx-3 13Q incubated with different molar ratios of NB01 (1:1 and 1:2) were loaded onto gel filtration chromatography column (Yarra SEC 3 μm SEC-3000) equilibrated with 20 mM sodium phosphate pH 7.2, 150 mM NaCl, 5% glycerol, 2 mM EDTA, 1 mM DTT buffer, and eluted at a flow rate of 0.2 mL/min. The eluted protein was redirected to the sample flow path for immediate SAXS data collection. 2500 frames (one per second) were collected at 10 ºC using 1M PILATUS detector over a scattering vector ($q = (4\pi \sin\theta)/\lambda$, where 2θ is the scattering angle) range up to 0.5 $Å^{-1}$, which corresponds to a sample-detector distance of 2.867 m. No radiation damage was detected. Data collection and treatment was performed by lab colleague Dr. José Manso.

Baseline subtraction was performed using the solution scattering right before the peak elution. Only the frames presenting protein were used for the subsequent data treatment. This selection was performed manually and merged to a single averaged frame.

Data was processed and analyzed with the *ATSAS* 2.8 package[138]. Pair--distance distribution function, *P*(*r*), was calculated with GNOM[139]. *Ab initio* shape reconstructions were calculated with the program DAMMIF[140]; fifteen independent reconstructions were superimposed, averaged, and filtered with DAMAVER[141]. Scattering profile of atomic structure was calculated with CRYSOL[142]. SAXS-based rigid body modeling of complexes with one or several of lack fragments with CORAL[143].

The 3D atomic structure for the SAXS-based rigid body modeling are the presenting ones: JD PDB accession 1yzb, UIM PDB accession 2hlz and PolyQ tract PDB accession 4wth and NB structure PDB accession 1I3V.

Thermal Shift Assay

The Thermal Shift Assay is a temperature based assay designed to study protein stability. An increase in temperature triggers the denaturation of the protein. During this step, a fluorophore (SYPRO ORANGE (Invitrogen)) may bind to the hydrophobic regions of the protein that are now accessible enhancing the fluorescence signal. The thermal shift assay was performed for each Atx-3 isoform in the presence of the NBs with the highest affinity (NB01 and NB02) to study their impact on the thermostability of Atx-3 isoforms and its isolated domains. For each condition, a final concentration of 0.3 mg/mL of Atx-3 isoform incubated with NBs (NB01 and NB02) in a ratio of 1:5. The experiment was performed in triplicate.

A final concentration of 10x SYPRO ORANGE dye was used (comparing to the stock solution 5000x). The temperature was increased from 25 ºC to 95 ºC in 0.5 ºC increments and the fluorescence was measured using a qPCR iQ5 (Biorad) and a Cy3 filter setup.

Complex Crystallization

Using the same approach as the one used for the purification of isolated Atx-3:NB complexes for DLS analysis, Atx-3 D1:NB complexes were purified by SEC in crystallization buffer (20 mM HEPES, 150 mM NaCl, 5% glycerol, 2 mM EDTA and 1 mM DTT). Fractions corresponding to complex peak were concentrated in an Amicon Ultra-15 (cut-off 3 kDa) centrifuge filter (Millipore) to a final concentration of 28 mg/mL and centrifuged during 15 min, 4 ºC at 15 000 rpm (Himac CT 15 RE, VWR).

The following commercial screens were used in initial crystallization tests: ProPlex, JCSG, MIDAS, PACT premier, Morpheus, SG1, PGA screen (Molecular Dimensions), Index, PEG/ION, Crystal Screen 1 and 2 (Hampton Research). The drops were setup using a crystallization robot Oryx 4 (Douglas Instruments). Two conditions were tested in the same crystallization plate: 0.1 μL complex drops at a concentration of 28 mg/mL were added to 0.1 μL of reservoir crystallization solution and a second condition in which 0.2 μL of complex were added to 0.1 μL of reservoir crystallization solution in sitting drop plates with 96 wells (SWISSCI, Scientific Innovation) with 50 μL of reservoir volume. The plate was stored at 20 ºC.

Scale-up of promising conditions were as well attempted, the precipitant concentration was varied from 20 %, 22.5 %, 25 %, 27.5 % to 30 % and the pH of the 0.1 M Tris buffer varied between 8.3, 8.5, 8.7 and 9.0. Drops consisted on two different protein:precipitant ratios: 1 μL 28 mg/mL Atx-3 D1:NB01 complex with 1 μL of precipitant and 1.5 μL of 28 mg/mL complex with 0.75 μL of reservoir solution in 24 wells sitting drop plates with 300 μL of reservoir volume. The crystallization plates were stored at 20 ºC.

Modulation of Ataxin-3 aggregation by Nanobodies

To study the effect of the selected NB in Atx-3 aggregation, sequential techniques were used. First, a Thioflavin T (ThT) aggregation assay was performed followed by a Filter Retardation Assay, Dot-blot with amyloid-specific antibodies and Transmission Electron Microscopy (TEM).

Thioflavin T Aggregation Assay

To analyze the effect of the selected NBs in Atx-3 amyloid formation an aggregation assay was performed using ThT. This compound is a benzothiazole salt that enhances its fluorescence upon binding to β-strands due to the rotational restriction of the central C–C bond. The binding occurs between side chains along the length of amyloid-like fibrils that are formed along the aggregation process.

However, despite its regular application in aggregation studies, this method has some limitations due to the formation of intermediate species that do not bind to ThT[144] and also due to other compounds, such as aggregation modulators, that may be present in solution and block the binding of ThT, decreasing the signal.[145] The typical profile of a ThT aggregation curve encompasses 3 distinct and sequential steps: the lag-phase, the elongation phase and the stationary phase. During the lag-phase the fluorophore does not report the formation of oligomeric species/protofibrils but the first

steps of aggregation are already occurring (concentration below the detection limit), leading to the formation of dimers and/or oligomers. After that, during the elongation phase, exponential increase in ThT fluorescence signal corresponds to the elongation of the oligomeric species into Atx-3 protofibrils/fibrils. The aggregation endpoint is the stationary phase in which an equilibrium in the fibrils amount occurs and the signal stabilizes.

Aliquots of purified Atx-3 variants were thawed on ice and centrifuged at 15 000 rpm (Himac CT 15 RE, VWR) during 15 min at 4 ºC to remove all precipitated protein. Protein was loaded into a Superdex 200 increase 5/150 GL (GE Healthcare Life Sciences) equilibrated in aggregation buffer (20 mM sodium phosphate pH 7.5, 150 mM NaCl, 1 mM DTT). Resulting fractions were kept on ice and the protein concentration was determined. After that, the protein was filtered using a centrifugal filter 0.22 μm (Ultrafree, Millipore) to remove all possible aggregates before the ThT experiment.

Atx-3 variants were diluted to a final concentration of 5 μM and NBs were added at a final ratio of 1:1 (5 μM), 1:2 (10 μM), 1:5 (25 μM) and 1:10 (50 μM). A ThT stock (SIGMA Aldrich) solution was added at a final concentration of 100 μM. After a gentle mix, 50 μL of each sample was loaded into Thermowell 96-Well Polycarbonate PCR Microplates (Costar) in 3 independent replicates for each condition. The microplate was centrifuged (Sorvall ST 40, ThermoFischer Scientific) at 1 200 rpm during 2 min. After that, 20 μL of parafilm oil (Molecular Dimensions) was added to each well to prevent sample evaporation. The plate was placed in FluoDia T70 microplate fluorimeter (Photon Technology International) previously heated at 37 ºC, with excitation and emission wavelength of 400 nm and 480 nm, respectively. Measurements were collected every 30 min and each cycle were preceded by a short orbital agitation.

Filter Retardation Assay

The first step in Atx-3 aggregation is independent of the polyQ tail and is controlled by the aggregation-prone region located within the globular JD. After the start of aggregation polyQ tails from different Atx-3 molecules, when expanded, can interact completing the second step of aggregation. These interactions between polyQ regions are mediated by hydrogen bonds leading to the self-assembly of β–sheets and the formation of long and straight mature amyloid fibres that are not disassembled by treatment with SDS. When the polyQ region is not expanded, the second step does not occur.

In the ThT experiment endpoint, the microplate was removed from the fluorimeter and 5 μL of each sample was boiled during 5 min in 200 μL of TBS buffer (50 mM Tris-HCl pH 7.5 and 150 mM NaCl) with 2% SDS and without SDS. After boiling, the mixture was loaded into a vacuous system (BioDot SF – BIORAD) previously prepared. First, two filter papers (BioDot SF – BIORAD) were soaked in TBS buffer as well as a cellulose acetate membrane, pore size 0.2 μm (GE Healthcare Life Sciences).

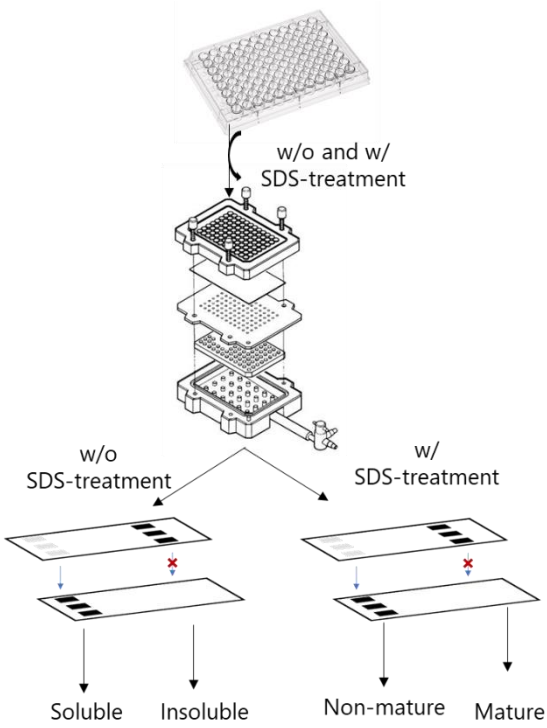

Figure 10: Filter Retardation Assay experiment representation. The experiment samples were removed from the aggregation plate and treated with and without SDS and loaded to the vacuous system with a cellulose acetate membrane placed on top of filter paper. Without SDS treatment, if the fibers are retained in the membrane it shows that the sample in study have insoluble fibers and it there not the fibers are soluble. With the SDS-treatment if the fibers retain in the membrane it is an evidence that we are examining mature fibers if not we are studying non-mature fibers.

The cellulose acetate membrane was placed on top of filter paper and the latter was placed in the vacuum system (system assembly in Figure 10). The vacuum system was closed, and the samples were loaded into the manifold wells. Samples with and without SDS treatment, were filtered through the membrane by applying vacuum without allowing the membrane to dry. After that, the membrane was washed with TBS with 0.1 % SDS (in the samples without SDS treatment) and with 2 % SDS (in the samples with SDS treatment). The membrane was blocked with 5 % milk in TBS-T buffer (50 mM Tris pH 7.5; 150 mM NaCl and 0.1% Tween 20) during 1 h at room temperature. The membrane was incubated with primary antibody anti-Atx-3 1H9 (1:1000) (Millipore) overnight at 4 ºC followed by the secondary antibody anti-mouse (Sigma-Aldrich) (1:10 000) for 2 h at room temperature. The membrane was developed using ECL reagent (GE Healthcare Life Sciences).

Dot-blot

Samples from the ThT aggregation assay were also used to perform a dot-blot assay to compare the Atx-3 oligomeric intermediary species present at the endpoint aggregation in the absence and in the presence of NB. In this study, the 2 μL of each sample was loaded into a nitrocellulose membrane (BIORAD) through circular

templates. The membrane was then blocked with 5 % BSA. The membrane was successively incubated with the following antibodies: Antibody anti-Atx-3 1H9 (ON at 4 ºC), Antibody Anti-OC (ON at 4 ºC) and Antibody Anti-A11 (1h at RT). Between each immunoblot the membrane was stripped using Restore Western Bolt Stripping Buffer (Thermo Fisher Scientific). Information about the primary antibodies and their secondary antibodies is detailed in Table 4.

Transmission Electron Microscopy

To analyze the morphology of the aggregates/protofibrils/fibrils present at the endpoint of ThT assay, negative-stain transmission electron microscopy (TEM) using carbon-coated 200 mesh nickel grids (FCF300-NI, Electron Microscopy Science) was executed. The endpoint samples were diluted in to a final concentration of 2.5 μM of Atx-3 with milliQ water. 5 μL of the diluted sample was placed and absorbed by the grids (Electron Microscopy Science) during 2 min. After that, 2 μL of 2 % (w/v) uranyl acetate (ANAME) was loaded in the grid for 15 sec for negative-staining. The images were acquired at a magnification of 80,000–100,000x using an electron microscope JEM-1400 (JEOL) at an accelerating voltage of 80 kV at IBMC, Porto, Portugal.

Time course analysis of Atx-3 self-assembly

To study soluble species involved in the early events of the aggregation pathway an oligomerization time course analysis was performed using SEC. In addition, a DLS experiment was performed to study the molecular distribution of the sample along the aggregation.

Size Exclusion Chromatography

To monitor the effect of NB01 and NB05 in the soluble species formed during Atx-3 13Q and Atx-3 77Q isoforms aggregation a time course analysis using SEC was performed. Along the aggregation process, samples were loaded in a Superdex 200 increase 5/150 GL (GE Healthcare Life Sciences).

Using the protocol previously described, the protein was thawed, centrifuged and injected in a Superdex 200 increase 5/150 GL (GE Healthcare Life Sciences) to remove some intermediary species and to remove the glycerol that was present in the Atx-3 buffer. After elution, protein concentration was determined, and the protein was diluted to a final concentration of 5 μM in 700 μL. NB01 (for Atx-3 13Q and 77Q) and NB05 (for Atx-3 77Q) was added to a final concentration of 10 μM and 50 μM, respectively. The samples, Atx-3 13Q 5 μM (control), Atx-3 13Q:NB01 (1:2),

Atx-3 77Q 5 μM (control), Atx-3 77Q:NB01 (1:2), Atx-3 77Q:NB05 (1:10), NB01 (10 μM) and NB05 (50 μM) were incubated at 37 ºC without shaking. At different time points, 50 μL aliquots were collected, filtered in a centrifugal filter 0.22 μm (Ultrafree, Millipore) and injected into a Superdex 200 increase 5/150 GL (GE Healthcare Life Sciences).

To monitor the assay and to select the proper times for the chromatography step a ThT assay under the same experimental conditions was also performed simultaneously.

Dynamic Light Scattering

To study the effect of NB01 in the average size distribution of species during the Atx-3 13Q self-assembly an aggregation assay was made using DLS. Measurement were performed using an ALV/DLS/SLS-5000F, SP-86 goniometer system (ALV-GmbH) equipped with a CW diode-pumped Nd:YAG solid-state Compass-DPSS laser with a symmetrizer (Coherent Inc). The laser operated at 488 nm with an output power of 400 mW. The intensity scale was calibrated against scattering from toluene.

The samples, 700 μL of 5 μM Atx-3 13Q and Atx-3 13Q:NB01 (1:2), previously centrifuged, repurified in aggregation buffer and filtrated in a centrifugal filter 0.22 μm (Ultrafree, Millipore) were incubated in a DLS glass cuvette at 37 ºC and scattering was periodically at a 90º angle to the incident beam. Hydrodynamic radii of the particles in solution were estimated from the diffusion coefficient obtained from COMTIN3 analysis of the auto-correlation function of scattered light intensity. Data collection and treatment was performed by lab colleague Dr. Pedro Martins.

Results and Discussion

Recombinant Protein Purification

Purification of Ataxin-3 isoforms and truncated variants

The four Atx-3 variants used in this study (Josephin Domain (JD), D1, full-length 13Q and full-length expanded 77Q) (Figure 6) were expressed according to the protocol previously described in methods. After expression, the cells were lysate and the supernatant was loaded onto a pre-equilibrated Ni^{2+}- charged Histrap and the protein was eluted with a gradient of imidazole (Figure 11A, green line). Atx-3 eluted with 50 % of imidazole (250 mM) was applied to a second purification step by size exclusion chromatography (SEC) (Figure 11B, 11D, 11F and 11H) to ensure the removal of any contaminants and possible aggregates or intermediate protein states that are formed during the expression and purification process, thereby enriching the monomeric form.

The Atx-3 variants have different elution volumes due to their different molecular weights (Figure 11B, 11D, 11F and 11H). During the purification process aliquots were collected and loaded in a SDS-PAGE to confirm the purity of the final protein in each step of the purification process (Figure 11C, 11E, 11G and 11I). The protein yield varies according to the Atx-3 isoform (Figure 11J).

SDS-PAGE gels demonstrate that throughout the purification process the presence of contaminants is reduced but in some cases, after the final step, some contaminants are still present. Analyzing the SEC profile (Figure 11B, 11D, 11F and 11H), it is noticed that protein aggregates are formed during the expression and purification process, particularly in the full-length proteins containing the polyQ tract that increases the protein aggregation tendency.

A

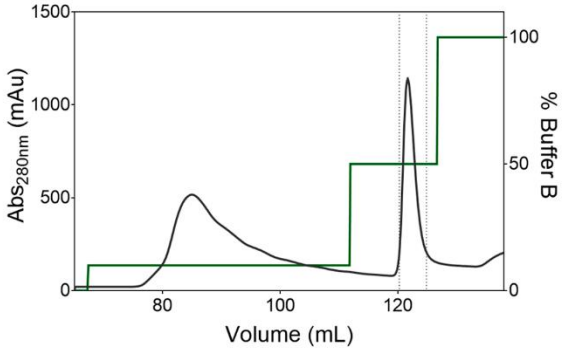

B Atx-3 JD (S200)

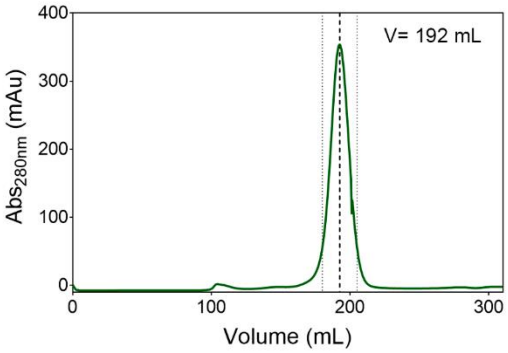

D Atx-3 D1 (S200)

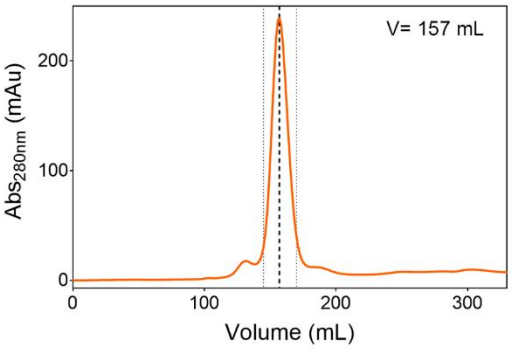

C Atx-3 JD

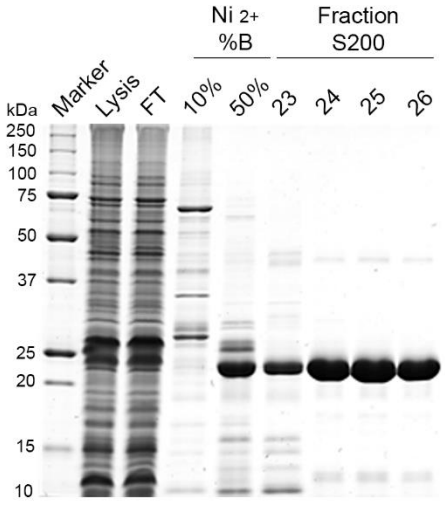

E Atx-3 D1

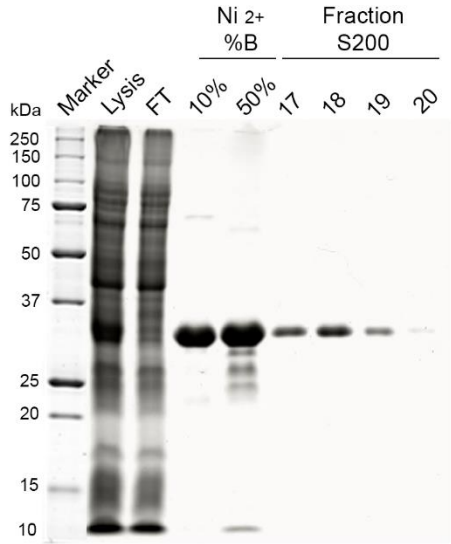

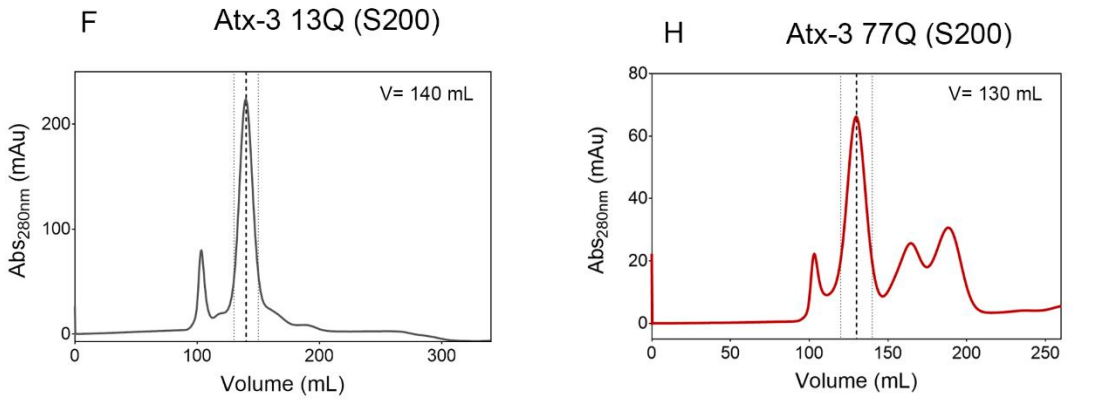

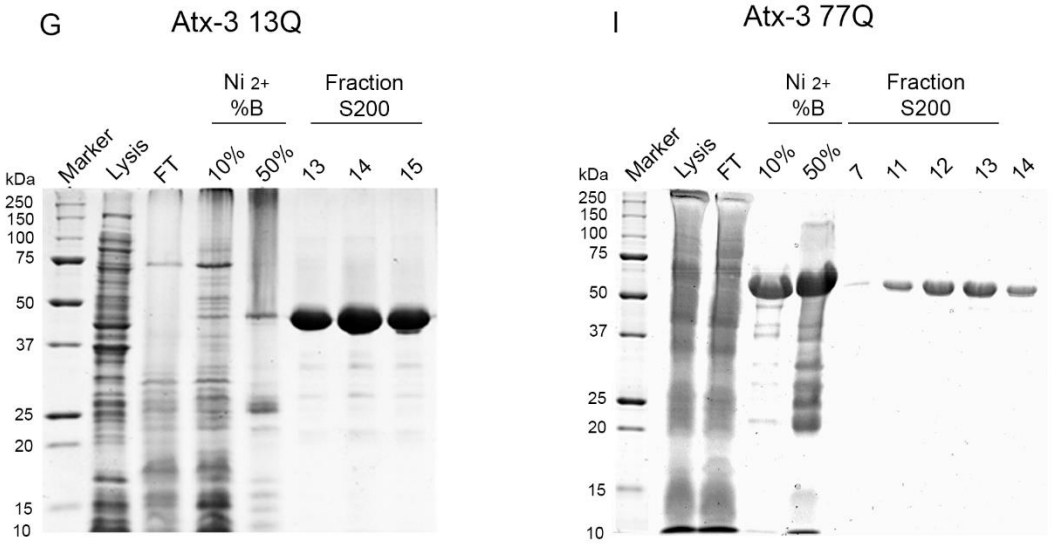

J

Atx-3 isoforms purification				
Atx-3 Isoforms	Molecular Weight (Da)	S200 Factions	S200 Elution Volume (mL)	Yield mg/L of culture
Atx-3 JD	21859	23-26	192	3.5 mg/L
Atx-3 D1	32581	17-20	157	2.7 mg/L
Atx-3 13Q	43583	13-15	140	2.1 mg/L
Atx-3 77Q	51882	11-14	130	0.6 mg/L

Figure 11: Purification of Atx-3 variants. A) Representative of a Ni^{2+}- charged Histrap elution profile with two steps, first with lower imidazole concentration (50 mM, 10% buffer B) and then with an increased concentration of imidazole (250 mM, 50% buffer B) (green line). Protein elution was detected by monitoring the absorbance at 280 nm (left axis). Size exclusion chromatography profile of B) Atx-3 JD (green), D) Atx-3 D1 (orange), F) Atx-3 13Q (grey) and H) Atx-3 77Q (red). The selected fractions were injected into a size exclusion chromatography column where the protein elution could be observed by following monitoring the absorbance at 280 nm. SDS-PAGE was used to monitor the sample purity throughout the purification process for each variant: C) Atx-3 JD, E) Atx-3 D1, G) Atx-3 13Q and I) Atx-3 77. J) Summary table of molecular weight, elution fractions selected in SEC and pooled together for further assays, elution volume of the main peak and expression yield for each Atx-3 variant.

Small-Scale expression and purification of the Nanobodies

Following expression and purification of Atx-3 constructs the selection of the most promising NBs for the forthcoming studies was also required, starting with small--scale expression (500 mL culture) and purification steps. First, three distinct expression conditions were tested in TB medium in which the temperature and the induction time were varied: 4 hours at 37 ºC, overnight (ON) at 28 ºC and finally ON at 25 ºC (Figure 12A). The presence of a secretion signal within the NBs sequence mediates the export of the protein to the periplasmic space, allowing the preparation of a cell extract by osmotic shock thereby considerably decreasing the amount of contaminants present in the soluble fraction. Regarding the expression conditions, no major differences in protein expression are visible between the expression conditions and the protein in study, in all cases, is present in the soluble fraction. It is further noted that before IPTG addition there is no NB expression proving that the system is controlled and there is no basal expression. Therefore, the temperature of 37 ºC and cell collection 4h after induction was selected for expression of all NBs being studied.

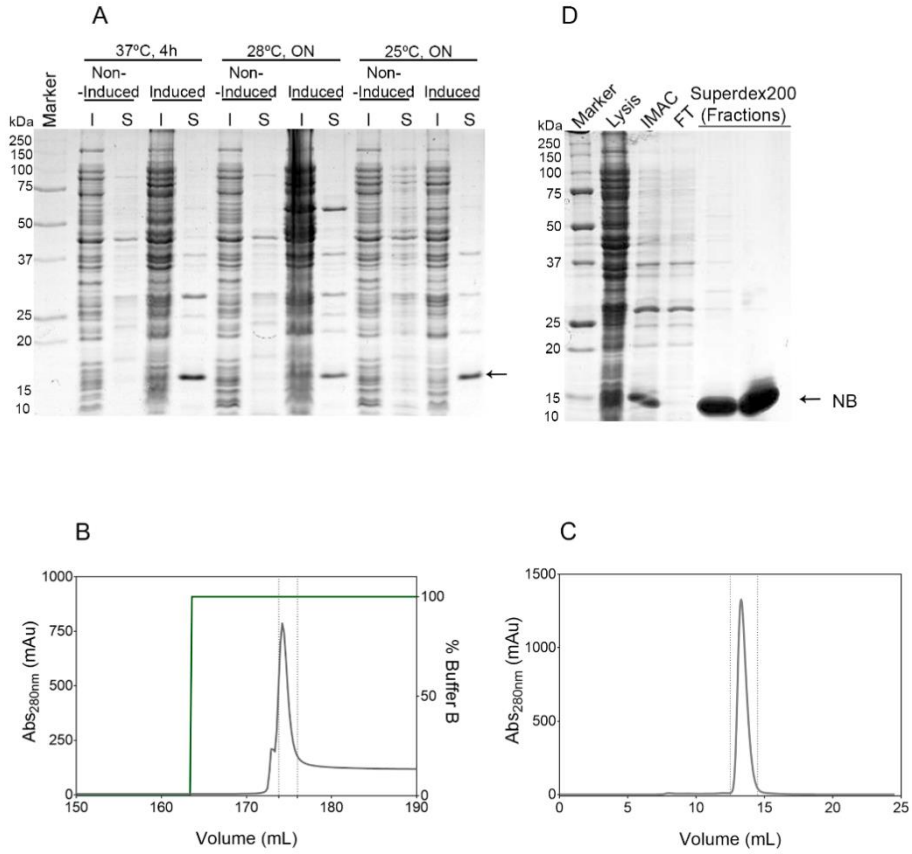

Figure 12: Small-scale expression and purification of NBs. A) Representative SDS-PAGE analysis of expression conditions tested for NB05. Cell growth temperatures of 37 ºC, 28 º and 25 ºC were tested, and expression was induced with IPTG for 4 hours (37 ºC) or overnight (ON). Soluble (S) and insoluble (I) fractions were analyzed before and after induction of protein expression. B) Representative Ni^{2+}- charged Histrap chromatography profile showing a single elution step with 100% buffer B (300 mM Imidazole) (green line). C) Size exclusion chromatography. Protein was detected by monitoring the absorbance at 280 nm. D) SDS-PAGE analysis of the purification steps (Lysis, Ni^{2+}- charged Histrap pooled fraction, Flow Through and SEC fractions).

After the selection of the best expression condition, the NBs were purified by two sequential steps: first with an Ni^{2+}-charged Histrap (Figure 12B) with only one elution step (300 mM imidazole) in which the NB-containing fraction was loaded on the SEC column (Figure 12C). The purity of the samples was analyzed by SDS-PAGE gel (Figure 12D).

Unfortunately, one of the NBs (NB10) raised against Atx-3 JD did not express in the soluble fraction in the preliminary expression screen and consequently it was not used for further studies.

Nanobody Purification (Large–Scale)

A large–scale expression and purification was required after the selection of the most promising NB (described below). Scale–up to 3L of culture was carried out using the same protocol and purification was done as described above: Ni2+-charged Histrap chromatography (Figure 13A) followed by SEC. The four NB that were selected for large scale purification (see below) have slightly different elution volumes, which result from small differences in their molecular weights and/or additionally from possible interactions with the column matrix (Figure 13B, 13D, 13F and 13H). Throughout the purification procedure samples were collected and analyzed by SDS--PAGE to verify their purity. It is noted that during the purification the contaminants in the total extract are almost totally removed (Figure 13C, 13E, 13G and 13I), but the expression yield varies greatly depending on the NB (Figure 13J).

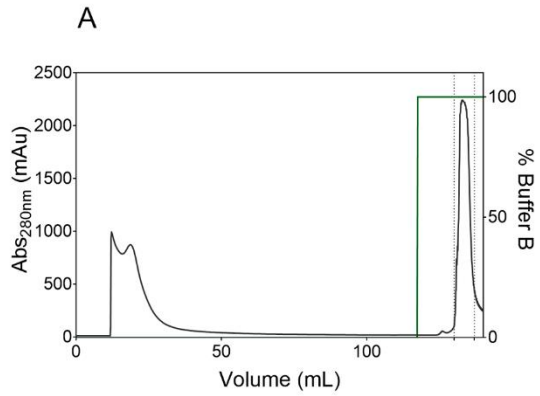
A
2500
2000
1500
1000
500
0
Abs280nm (mAu)
100
50
0
% Buffer B
0
50
100
Volume (mL)

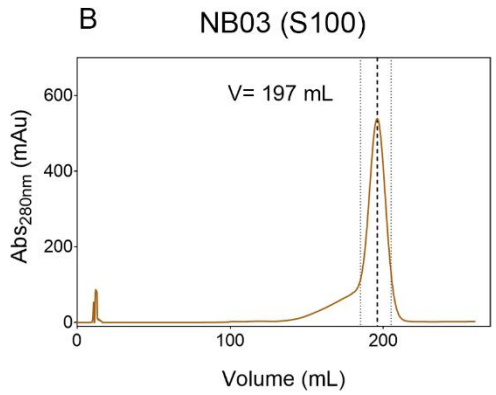
B
NB03 (S100)
V= 197 mL
600
400
200
0
Abs280nm (mAu)
0
100
200
Volume (mL)

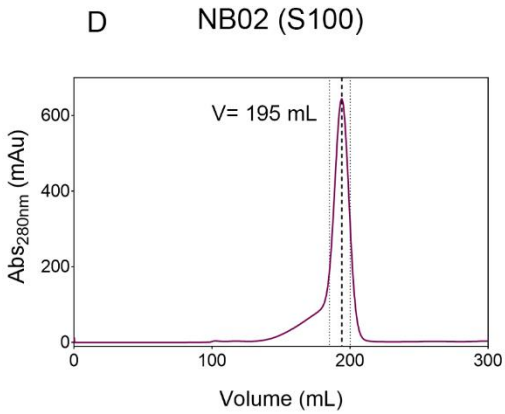
D
NB02 (S100)
V= 195 mL
600
400
200
0
Abs280nm (mAu)
0
100
200
300
Volume (mL)

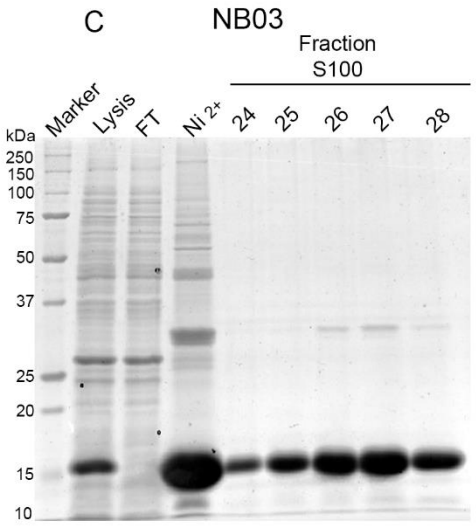
C
NB03
Fraction
S100
Marker
Lysis
FT
Ni 2+
24
25
26
27
28
kDa
250
150
100
75
50
37
25
20
15
10

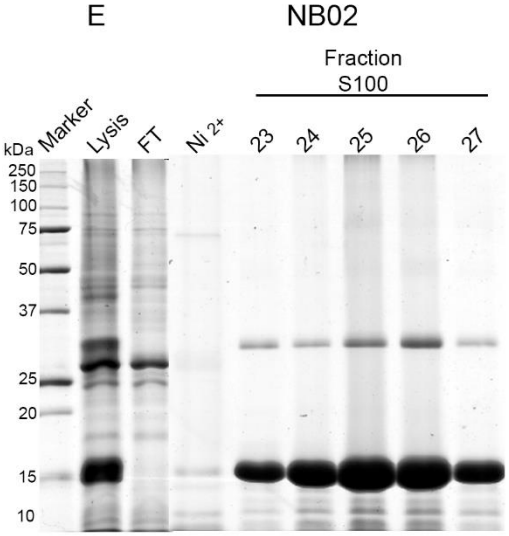
E
NB02
Fraction
S100
Marker
Lysis
FT
Ni 2+
23
24
25
26
27
kDa
250
150
100
75
50
37
25
20
15
10

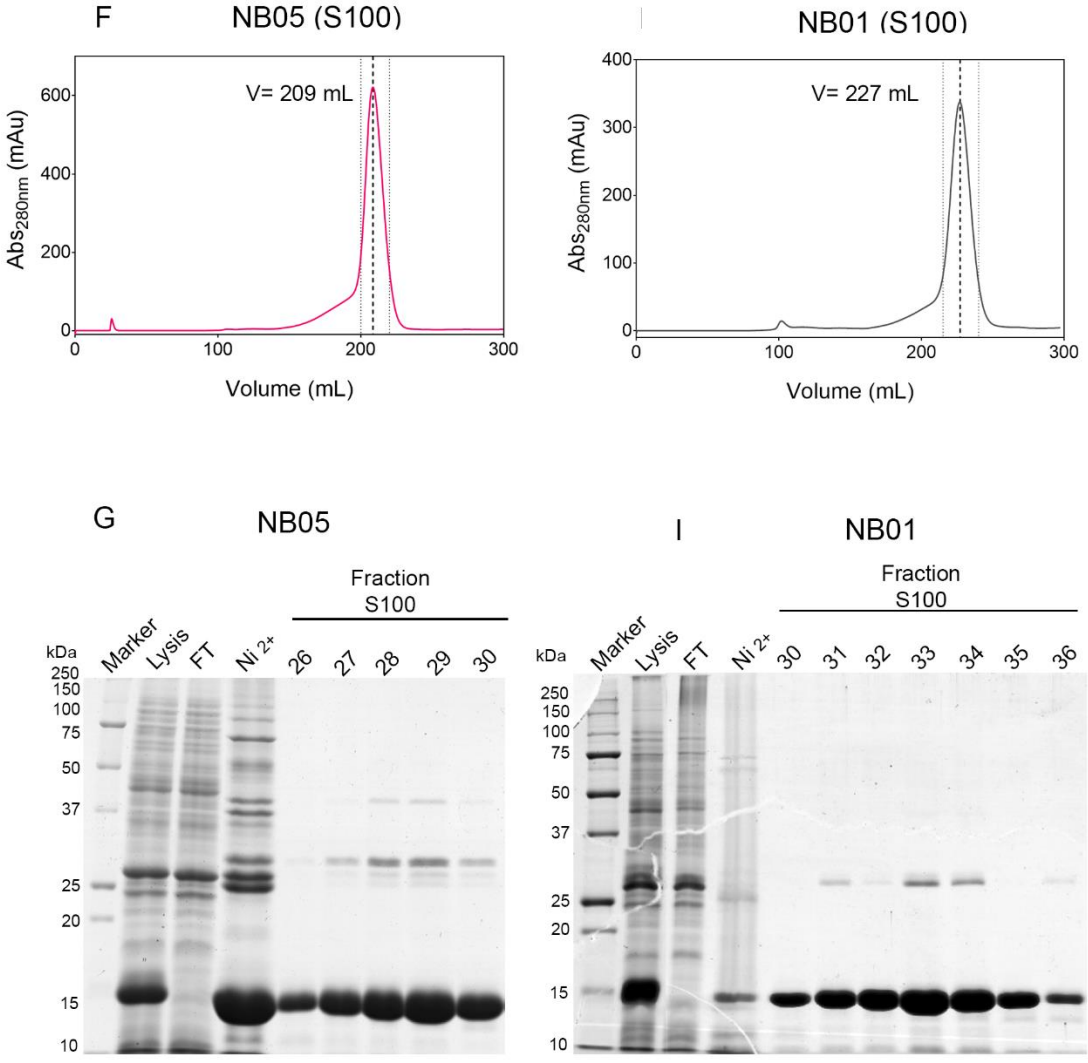

J

NB purification				
NB nr.	Molecular Weight (Da)	S100 Factions	S100 Elution Volume (mL)	Yield mg/L of culture
NB03	15091.6	25-28	197	3.0 - 6.3 mg/L
NB02	14499.2	24-27	195	
NB05	14080.6	27-30	209	
NB01	14155.7	30-34	227	

Figure 13: NB Purification (large-scale). A) Representative Ni^{2+}- charged Histrap elution profile with a purification step with 100 % buffer B (300 mM Imidazole) (green line). Protein elution was detected by monitoring the absorbance at 280 nm (left axis). SEC profile of B) NB03 (brown), D) NB02 (purple), F) NB05 (pink), H) NB01 (grey). Protein presence was monitored by measuring the absorbance at 280 nm. The NB-containing fractions were injected into a size exclusion chromatography column where the protein elution could be observed by following monitoring the absorbance at 280 nm. SDS-PAGE was used to monitor the sample purity throughout the purification process for each variant: C) NB03, E) NB02, G) NB05 and I) NB01. J) Summary table of molecular weight, elution fractions selected in SEC and pooled together for further assays, elution volume of the main peak and expression yield for each NB.

Selection of Atx-3 interacting nanobodies

Pull-Down Assay

After completing the expression and purification of Atx-3 constructs and all of the NBs produced against the JD it was necessary to make a pre-selection of the most interesting candidates for future studies. This was achieved with a pull-down assay using Atx-3 13Q (full length) variant as bait protein and all 17 NBs (see Figure 14).

In this assay, sepharose beads coated with protein G were used to bait the monoclonal anti-Atx-3-1H9 antibody. Upon incubation of the NBs with the Atx-3 13Q its immunoprecipitation with anti-Atx-3-1H9 antibody will capture the specific Atx-3 13Q interactors, which will be then detect by SDS-PAGE (schematic representation of the protocol in Figure 9).

Analyzing the results shown in Figure 14A it is perceptible when the sepharose beads are incubated with the Anti-Atx-3 1H9 antibody the presence of two bands corresponding to the antibody heavy (higher molecular weight) and light chains (low molecular weight). When beads are incubated with Atx-3 13Q, the presence of a light band is visible, showing that a nonspecific binding occurs between the beads and the Atx-3 13Q itself, yet, this will not interfere with the pull-down assay. When Atx-3 13Q is incubated with the beads in the presence of the antibody three bands are detected, the two antibody related bands and one corresponding to Atx-3 13Q.

NBs controls were also performed and when NB is incubated with the beads, a non-specific interaction is present (low molecular weight band). However, the coating of the sepharose beads with the anti-Atx-3 1H9 antibody prevented the binding of NB to the beads (Figure 14A).

Finally, this assay suggests the formation of a complex between Atx-3 13Q and NB01 as well as between Atx-3 13Q and NB02, which is demonstrated in the SDS--PAGE gel. Nevertheless, NB03 (Figure 14B) and NB05 (Figure 14A) are not captured upon incubation with Atx-3 13Q suggesting that no interaction occurs, at least with this variant of Atx-3 and/or in these condition, but which does not exclude the putative interaction with other Atx-3 variants, which was further evaluated as detailed below.

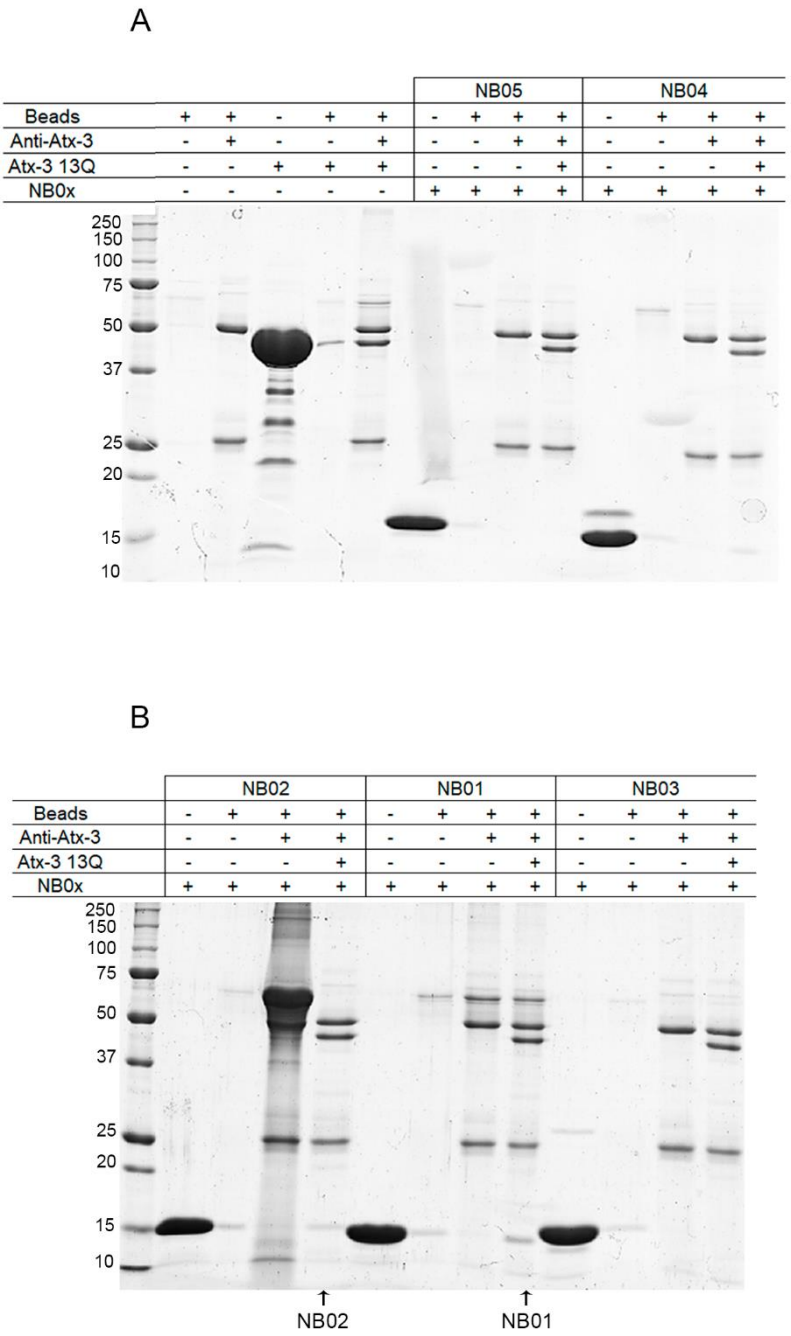

Figure 14: Pull-Down Assay between Atx-3 13Q and NBs produced against JD. Experimental controls and assay results were analyzed by SDS-PAGE. The legend for each lane is displayed above the gel. The NB01 and NB02 interact Atx-3 13Q, while NB03 and NB05 do not interact with this variant in the conditions tested in the pull-down assay.

As mentioned above, this is a fast way to select some promising interactors of Atx-3. Yet, these results must be confirmed by additional experiments, such as a gel filtration to exclude the existence of false positives (non-specific interaction) or false negatives (NB interaction not detected probably due to blocking of the binding site by the antibody or the complex affinity is too low to be detected by SDS-PAGE).

Table 6: Summary of the Pull-Down Assay Results in the screen for Atx-3 13Q interacting NBs. ✓ represents a positive interaction with Atx-3 13Q; X no interaction detected using this approach * represents the NB that was not tested due to its insolubility in the preliminary expression and purification assays.

Pull-Down Assay	
Atx-3 13Q vs	
NB01	✓
NB02	✓
NB03	X
NB04	✓
NB05	X
NB06	✓
NB07	✓
NB08	X
NB09	X
NB10	*
NB11	✓
NB12	X
NB13	✓
NB14	✓
NB15	✓
NB16	X
NB17	✓
NB18	✓

Size Exclusion Chromatography

To verify the negative interaction detected for NB03 and NB05 and to validate the NBs selected as potential interactors (NB02 and NB01) a SEC was carried out.

Atx-3 variants (20 μM) and each NB (40 μM) were incubated (1:2 ratio) and loaded into a gel filtration column. Resulting fractions were loaded in an SDS-PAGE to confirm the coexistence of both proteins in each peak. Atx-3 and each NB were also loaded separately to determine the elution volume of each isolated protein. This assay was performed with NB03, NB05, NB02 and NB01 incubated with the four Atx-3 variants (Atx-3 JD, Atx-3 D1, Atx-3 13Q, Atx-3 77Q).

NB03 Based on the pull-down assay NB03 was selected as a non-interactor of Atx-3 13Q and the SEC profile confirms this notion (Figure 15). Based on this information this NB was used in subsequent assays as a negative control.

NB05 Regarding NB05 (similarly to NB03, NB05 in the pull-down assay was not captured suggesting no affinity to Atx-3 13Q), a small shift for a higher molecular weight observed in the SEC profile upon incubation with Atx-3 D1 and Atx-3 13Q (Figure 16B and 16C), suggesting the formation of a complex. However, no shift was observed upon incubation with Atx-3 JD (Figure 16A) and only a slight increase in the absorbance of the complex with Atx-3 77Q (Figure 16D). An explanation for these results could be that in the pull-down assay, the antibody Anti-Atx-3 1H9 used against Atx-3 13Q may have hindered the interaction interface between NB05 and Atx-3 13Q. In the SEC studies, due to the absence of the Anti-Atx-3 antibody, the formation of the complex was possible.

NB02 Incubation with JD followed by SEC analysis revealed no evidence of complex formation with NB02 (Figure 17A) even though this NB was specifically produced against this truncated variant. Nonetheless, upon incubation of Atx-3 D1 with NB02 the formation of a complex was observed with a shift of the peak to a lower elution volume, corresponding to a higher molecular weight, accompanied by the decrease in the absorbance of the peak corresponding to isolated NB02 (Figure 17B). The same result was obtained upon incubation with Atx-3 13Q and Atx-3 77Q (Figure 17C and Figure 17D, respectively) demonstrating that NB02 interacts with Atx-3 D1, Atx-3 13 and Atx-3 77Q variants. Additionally, SDS-PAGE gels from the SEC fractions were performed and the presence of both NB02 and Atx-3 variants in the fractions peaks corresponding to the complexes were confirmed (Figure 17). These results confirm the pull-down experiment, but more information regarding the complex formation was needed.

NB01 Using the same approach, the binding of NB01 to Atx-3 variants was also tested. Like the other NBs, NB01 apparently does not interact with Atx-3 JD (Figure 18A). Still, complex formation between NB01 and Atx-3 D1 (Figure 18B), Atx-3 13Q (Figure 18C) or Atx-3 77Q (Figure 18D) variants was observed by SEC and the presence of both NB01 and Atx-3 variants in the peaks corresponding to the complexes were confirmed by SDS-PAGE. As the NB01 peak disappeared entirely it can be hypothesized that this interaction will not occur in a ratio of 1 Atx-3 (D1/13Q/77Q) to 1 NB01 but may occur in a 1 Atx-3 to 2 NB01 or even in a higher

ratio. However, based only on this experiment we cannot make this kind of assumption and a further biophysical characterization of the complex was intended next.

Regarding all data obtained with the SEC and the pull-down experiments it was possible to confirm the interaction between NB02 and NB01 with all Atx-3 constructs except for Atx-3 JD (even though the NBs were specifically produced against this domain). A possibility for this lack of interaction may be the NB's ability to recognize only a specific conformation of Atx-3 JD. This specific conformation may be present at a higher frequency in the longest variants such as Atx-3 D1 (with the UIM1-2) or the full-length Atx-3 13Q and Atx-3 77Q. So, the interaction of the JD to these conformational NBs could be transient or too low to be detected by SEC, contrarily to what happened with the longer Atx-3 variants.

NB03, as previously shown by the pull-down assay and confirming with SEC, does not interact with Atx-3. Therefore, it will be used as a negative control for the subsequent experiments. NB05, which had been previously considered a negative control with no Atx-3 13Q interaction, is now a promising tool for future studies. Nevertheless, complementary biochemical assays are necessary to accomplish a more complete complex characterization with these four selected NBs and Atx-3 constructs.

NB03

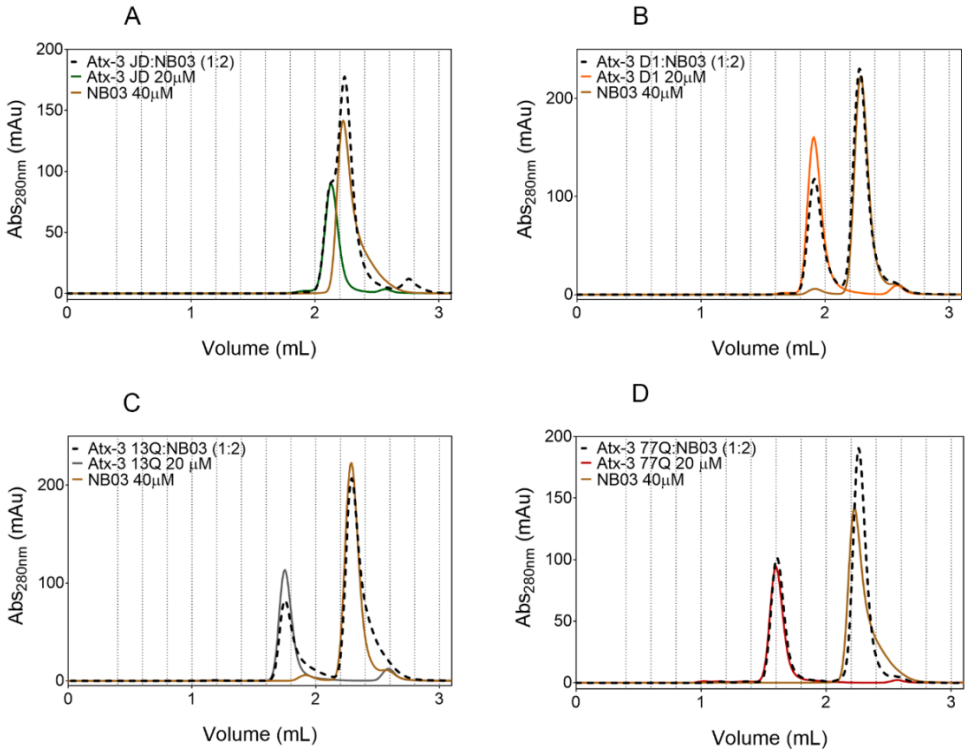

Figure 15: Size Exclusion Chromatography of Atx-3 variants incubated with NB03 profile. A) Atx-3 JD (green line), NB03 (brown line) and Atx-3 JD: NB03 complex (black dots). B) Atx-3 D1 (orange line), NB03 (brown line) and Atx-3 D1:NB03 complex (black dots). C) Atx-3 13Q (black line), NB03 (brown) and Atx-3 13Q:NB03 complex (black dots). D) Atx-3 77Q (red line), NB03 (brown line) and Atx-3 13Q:NB03 complex (black dots). There is no stable complex, both protein bands (Atx-3 variants and NB03) are eluted separatly.

NB05

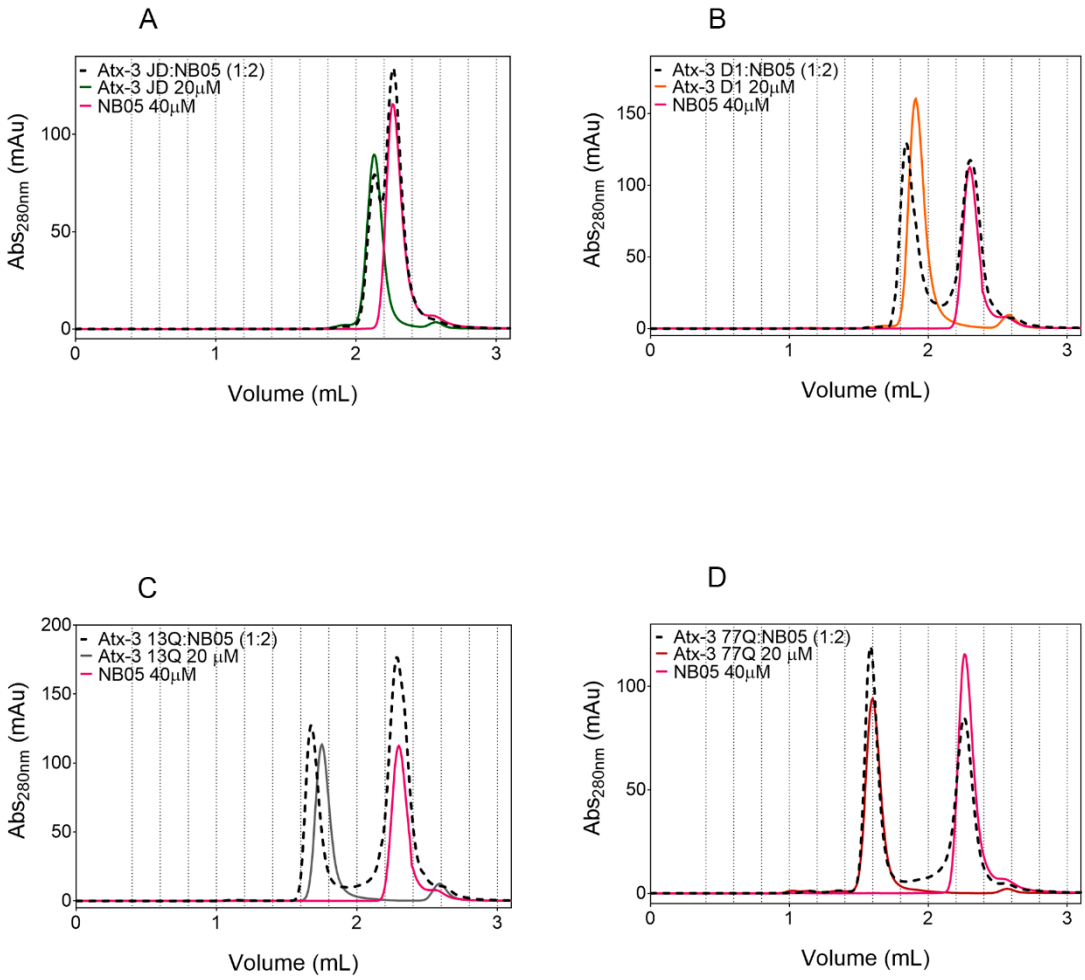

Figure 16: Size Exclusion Chromatography of Atx-3 variants incubated with NB05 profile A) Atx-3 JD (green line), NB05 (pink line) and Atx-3 JD:NB05 complex (black dots). B) Atx-3 D1 (orange line), NB05 (pink line) and Atx-3 D1:NB05 complex (black dots). C) Atx-3 13Q (black line), NB05 (pink line) and Atx-3 13Q:NB05 complex (black dots). D) Atx-3 77Q (red line), NB05 (pink line) and Atx-3 13Q:NB05 complex (black dots). Formation of a stable complex in (B) Atx-3 D1, (C) Atx-3 13Q and (D) a slight increase Atx-3 77Q shift to higher molecular weight, absorvance increase and desapearing of NB05 band. (A) Atx-3 JD no stable complex is formed. In the Atx-3 JD and NB02 the peak were not sucessfully separeted.

NB02

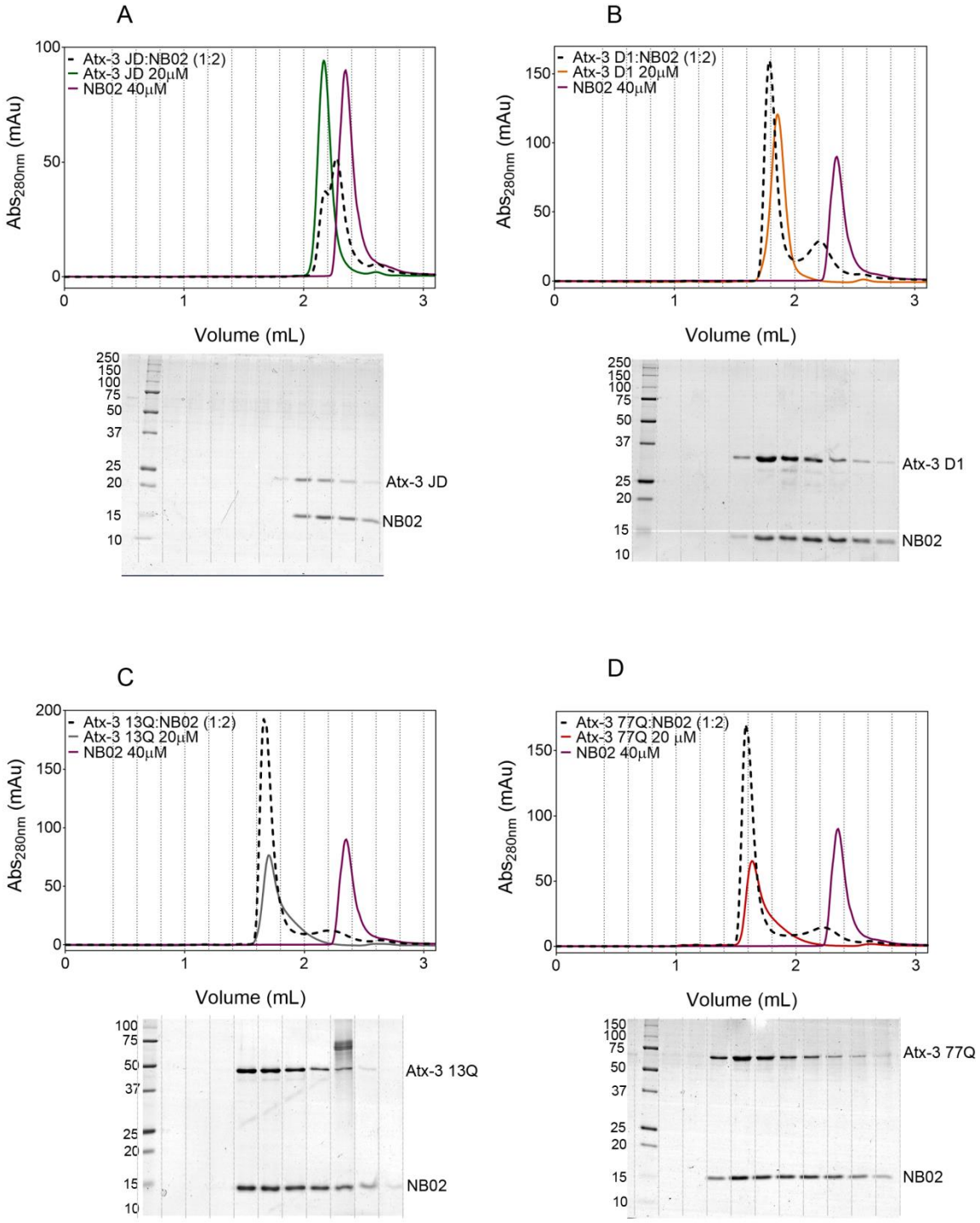

Figure 17: Size Exclusion Chromatography of Atx-3 variants incubated with NB02 profile. A) Atx-3 JD (green line), NB02 (purple) and Atx-3 JD:NB02 complex (black dots). B) Atx-3 D1 (orange lines), NB02 (purple line) and Atx-3 D1:NB02 complex (black dots). C) Atx-3 13Q (black line), NB02 (purple) and Atx-3 13Q:NB02 complex (black dots). D) Atx-3 77Q (red line), NB02 (purple line) and Atx-3 13Q:NB02 complex (black dots). Complex elution is evident in (B) Atx-3 D1:NB02, (C) Atx-3 13Q:NB02 and (D) Atx-3 77Q:NB02. There is no stable complex formation between Atx-3 JD and NB02. Bellow the chromatographic profiles the SDS-PAGE analysis is shown, demonstrating the presence of both proteins in the peak corresponding to the complexes.. In the Atx-3 JD and NB02 the peak were not sucessfully separeted.

NB01

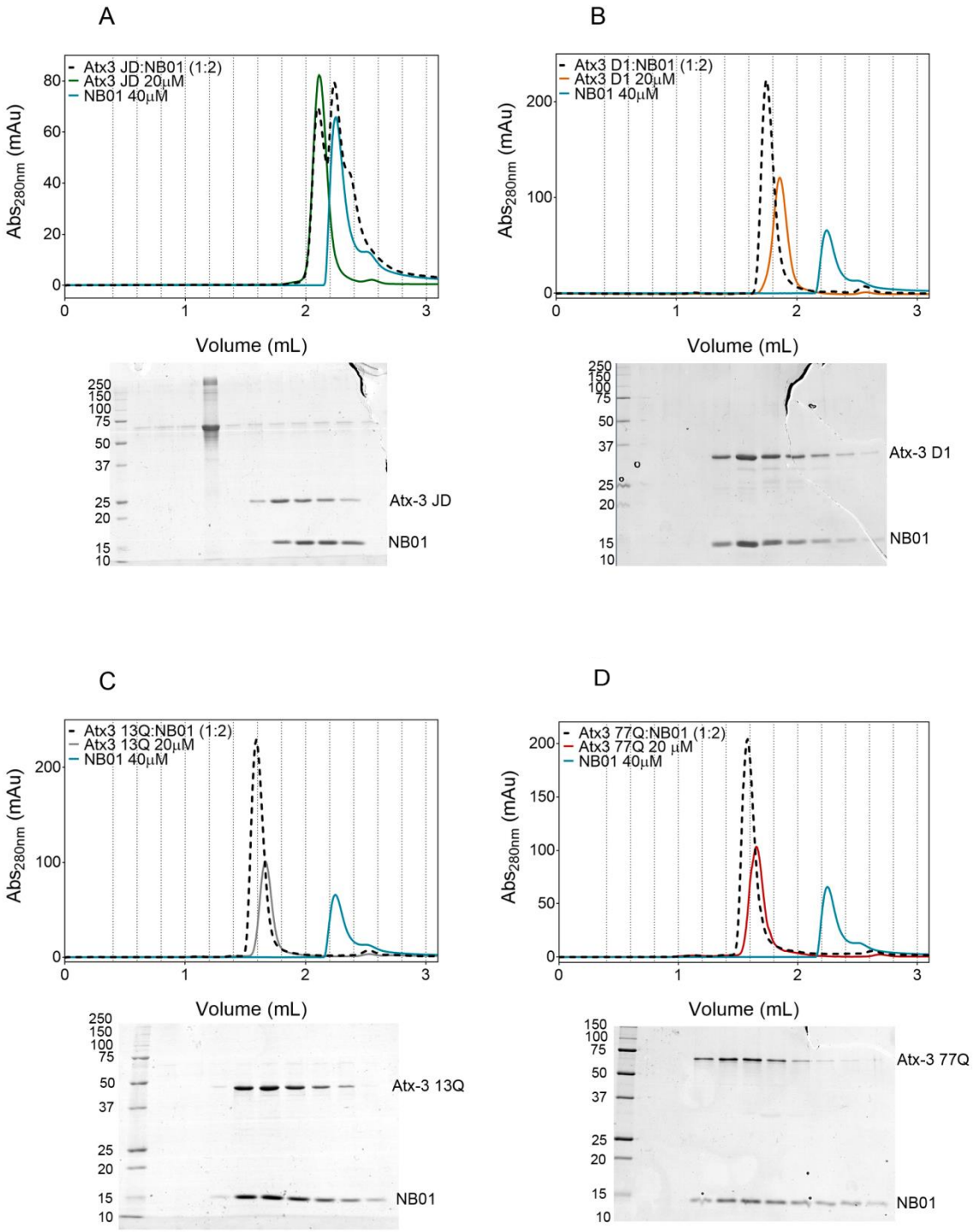

Figure 18: Size Exclusion Chromatography of Atx-3 variants incubated with NB01 profile. A) Atx-3 JD (green line), NB01 (blue) and Atx-3 JD:NB01 complex (black dots). B) Atx-3 D1 (orange lines), NB01 (blue line) and Atx-3 D1:NB01 complex (black dots). C) Atx-3 13Q (black line), NB01 (blue) and Atx-3 13Q:NB01 complex (black dots). D) Atx-3 77Q (red line), NB01 (blue line) and Atx-3 13Q:NB01 complex (black dots). Complex formation is evident in (B) Atx-3 D1:NB01, (C) Atx-3 13Q:NB01 and (D) Atx-3 77Q:NB01. There is no stable complex formation between Atx-3 JD and NB01. Bellow the chromatographic profiles the SDS-PAGE analysis is shown, demonstrating the presence of both proteins in the peak corresponding to the complexes. In the Atx-3 JD and NB01 the peaks were not sucessfully separated.

Characterization of the Atx-3:Nanobody complexes

Isothermal Titration Calorimetry

Isothermal Titration Calorimetry (ITC) assay was the technique chosen to characterize the nature of the interaction between Atx-3 and each NB. For this, the Atx-3 variants used in this work were separately titrated with each NB (in order, NB03, 05, 02, 01). With this experiment, it was possible to obtain the dissociation constant (K_D), stoichiometry (n) and thermodynamic parameters (ΔG, ΔH, $-T\Delta S$) of the binding at 20 ºC.

NB03 Once again no interaction between NB03 and Atx-3 was observed (flat signal, Figure 19A), either because i) it does not occur, ii) affinity is so low that it is not detected by this experimental condition or iii) this interaction does not generate or consume heat, preventing the interaction parameters to be calculated. Nonetheless, even if some interaction occurs this NB can still be used as a negative control in the following experiments since it cannot be detected.

NB05 It was possible to observe an interaction between NB05 and all the Atx-3 variants except for Atx-3 JD (Figure 20A). Using this technique, the K_D for the interactions between NB05 and the Atx-3 variants was determined as 407 ± 32 nM for Atx-3 D1, 393 ± 36 nM for Atx-3 13Q and 446 ± 13 nM for Atx-3 77Q (Figure 20B, 20C and 20D). The stoichiometry for these interactions is 1:1 demonstrating one Atx-3 binding site per NB. Additionally, it was also possible to determine the energy profile of the interaction (Figure 20E), in which the enthalpy energy is the component that dictates the complex formation, indicating a favorable hydrogen and/or van der Walls interactions.

NB02 ITC data regarding NB02 also revealed no binding towards Atx-3 JD (Figure 21A) contrasting, once again, with the well-established interaction observed for Atx-3 D1 (K_D = 1.4 ± 0.3 mM) (Figure 21B) with a stoichiometry of 1:1. The presence of the C-terminal region containing the polyQ tract increased the binding affinity of NB02 towards Atx-3 13Q (Figure 21C) and 77Q isoforms (Figure 21D) (K_D = 428 ± 34 nM and 911 ± 54 nM, respectively) interestingly with a stoichiometry of 1:2 for both. With this data, it is possible to suggest that Atx-3 D1 only has one interaction site and Atx-3 13Q and 77Q have two interaction regions for NB02 and it can be hypothesized that this second interaction site is located after the ubiquitin interaction motifs (UIM1-2).

Additionally, NB02 presents higher affinity to Atx-3 13Q and Atx-3 77Q than to Atx-3 D1, which may be explained by an increase in binding sites. This NB also exhibits an interaction for Atx-3 dictated by the enthalpic factor (Figure 21E), indicating that no large conformational changes occur during the complex formation, which is typical characteristic of this type of interaction (antibody:antigene)[146,147].

NB01 Even with ITC it was still not possible to detect an interaction between NB01 and Atx-3 JD (Figure 22A). However, the binding of NB01 to Atx-3 D1 was in the nanomolar range with a K_D of 49.4 ± 6.7 nM (Figure 22B). This time, the presence of the C-terminal region, containing the polyQ tract, slightly reduced the affinity of the NB01 towards Atx-3, namely to the non-expanded isoform Atx-3 13Q (K_D = 212 ± 9 nM) (Figure 22C), and Atx-3 77Q (K_D = 333 ± 49 nM) (Figure 22D). Regarding stoichiometry of interaction all 3 variants have a ratio of 1 Atx-3 molecule (D1, 13Q and 77Q) to 2 molecules of NB01 (Figure 22F), which agrees with preliminary SEC results. Again, the energetic parameter with the greatest impact was the enthalpic factor.

Comparing ITC data for all NBs, the NB with the highest affinity for the Atx-3 variants is NB01. Stoichiometry of reaction varies between a ratio of 1:1 and 1:2 (Atx-3 to NB) depending on the NB and on the Atx-3 variant. The energetic parameter controlling the complex formation in all samples corresponds to the enthalpic factor, indicating the formation of hydrogen and van der Walls interactions between the two proteins. This also indicates that no major structural changes are occurring.

NB03 once again was incapable of presenting any interaction with Atx-3. Contrarily, interaction between NB05 and Atx-3 variants was confirmed with an affinity even higher than NB02. Still, the stoichiometry duality (in NB01 and NB02) raises the question: how can NBs recognize more than one region in Atx-3 protein? In order to clarify this, Dynamic Light Scattering (DLS) and Small Angle X-ray Scattering (SAXS) were performed.

NB03

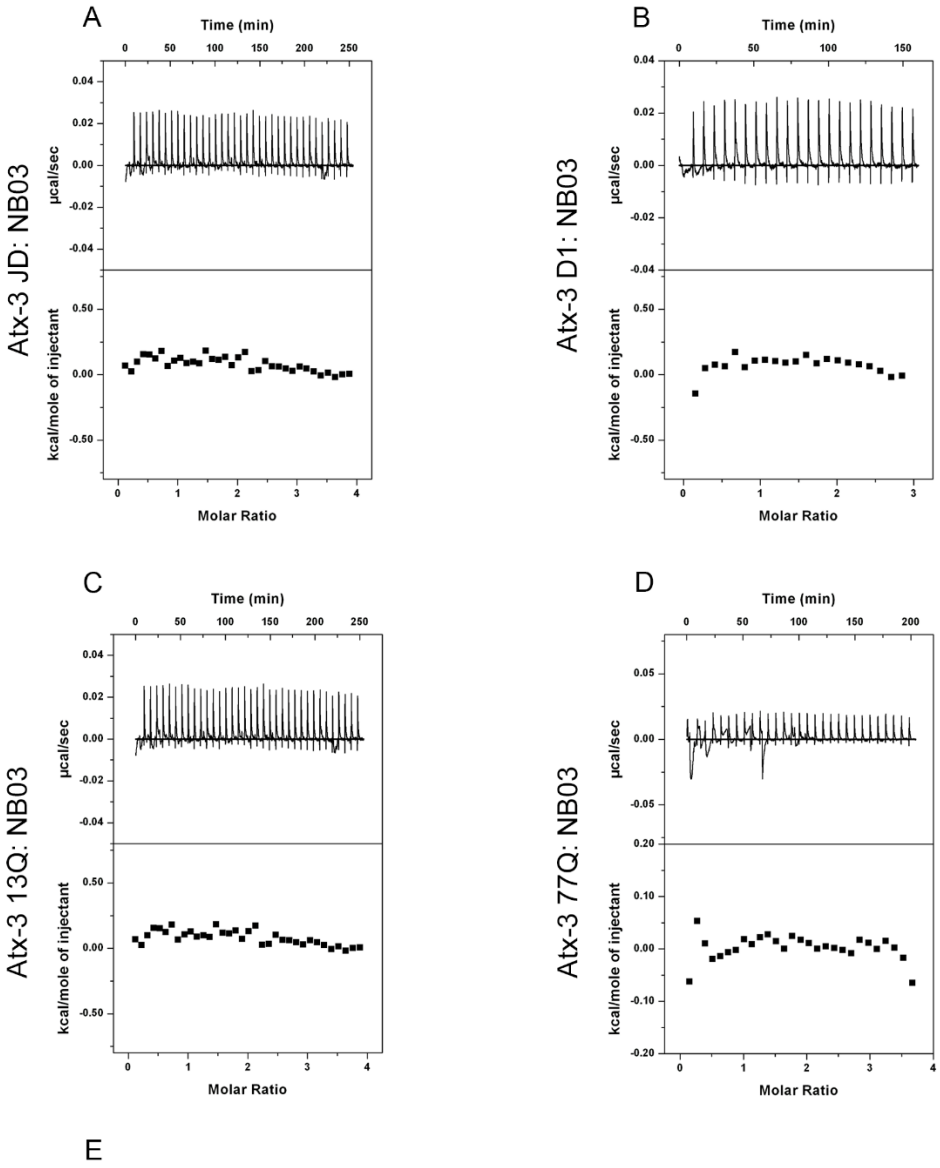

E

NB03					
Protein	N (Molar Ratio)	K_D (nM)	ΔH (kcal/mol)	-TΔSb (kcal/mol)	ΔG (kcal/mol)
Atx-3 JD	-	-	-	-	-
Atx-3 D1	-	-	-	-	-
Atx-3 13Q	-	-	-	-	-
Atx-3 77Q	-	-	-	-	-

Figure 19: Thermodynamic profiles of the NB03 interactions with Atx-3 variants analyzed by ITC. A) Atx-3 JD vs NB03, B) Atx-3 D1 vs NB03, C) Atx-3 13Q vs NB03, D) Atx-3 77Q:NB03. Measurement of the heat that is released during the NB03 injections (µcal/seg). E) Absence of parameter values.

NB05

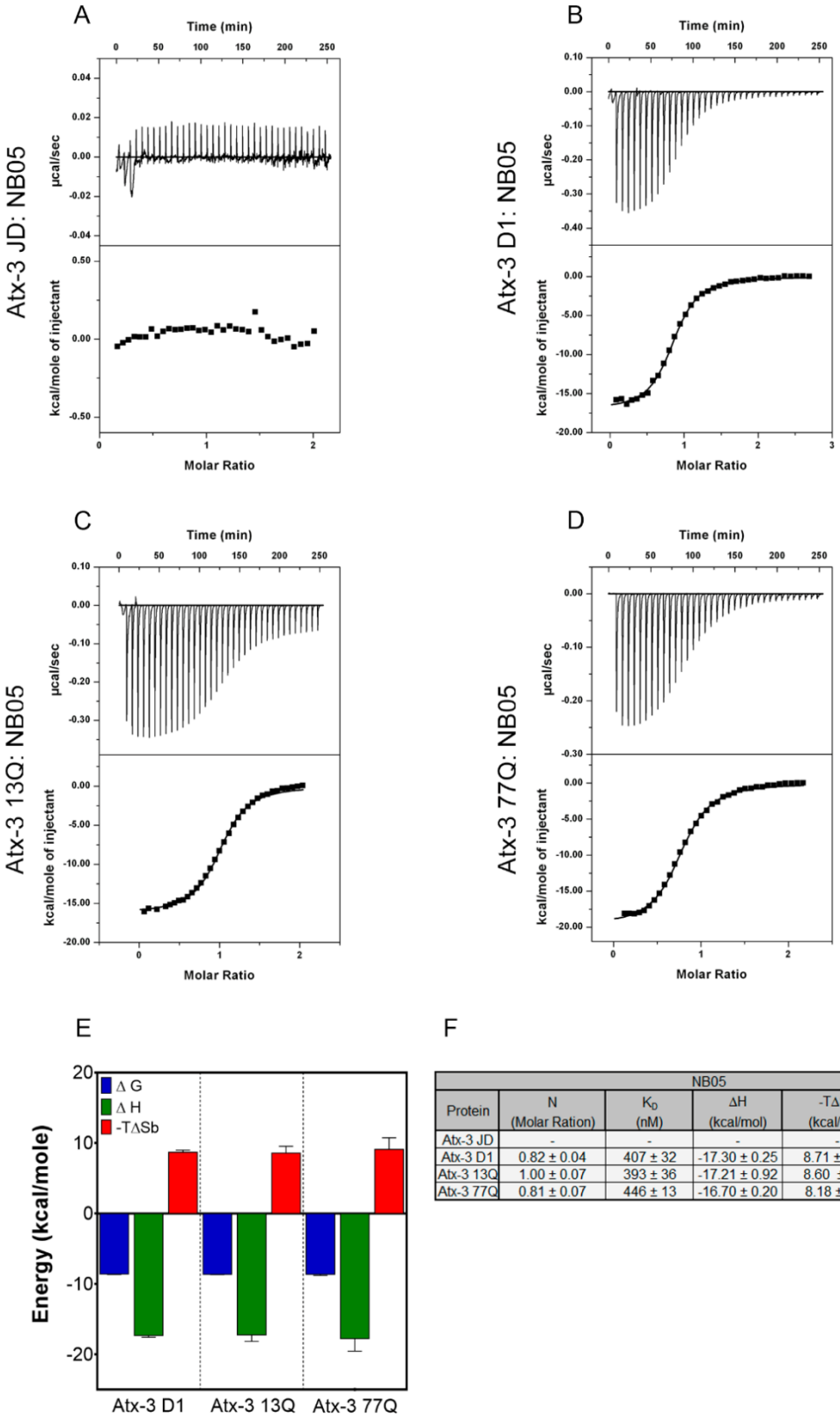

NB05					
Protein	N (Molar Ration)	K_D (nM)	ΔH (kcal/mol)	-TΔSb (kcal/mol)	ΔG (kcal/mol)
Atx-3 JD	-	-	-	-	-
Atx-3 D1	0.82 ± 0.04	407 ± 32	-17.30 ± 0.25	8.71 ± 0.29	-8.59 ± 0.04
Atx-3 13Q	1.00 ± 0.07	393 ± 36	-17.21 ± 0.92	8.60 ± 0.95	-8.61 ± 0.04
Atx-3 77Q	0.81 ± 0.07	446 ± 13	-16.70 ± 0.20	8.18 ± 0.17	-8.52 ± 0.03

Figure 20: Thermodynamic profiles of the NB05 interactions with Atx-3 variants analyzed by ITC. A) Atx-3 JD vs NB05, B) Atx-3 D1:NB05, C) Atx-3 13Q:NB05, D) Atx-3 77Q:NB05. Measurement of the heat that is released during the NB05 injections (µcal/seg) and experimental data fitting using a single binding site model. E) Energetic parameters of the complex formation (Atx-3 D1, Atx-3 13Q and Atx-3 77Q) ΔG (blue), ΔH (green) and -TΔS (red). F) ITC parameter values N (molar ratio), K_D, ΔH, -TΔS and ΔG, and error calculation in experiment triplicates.

NB02

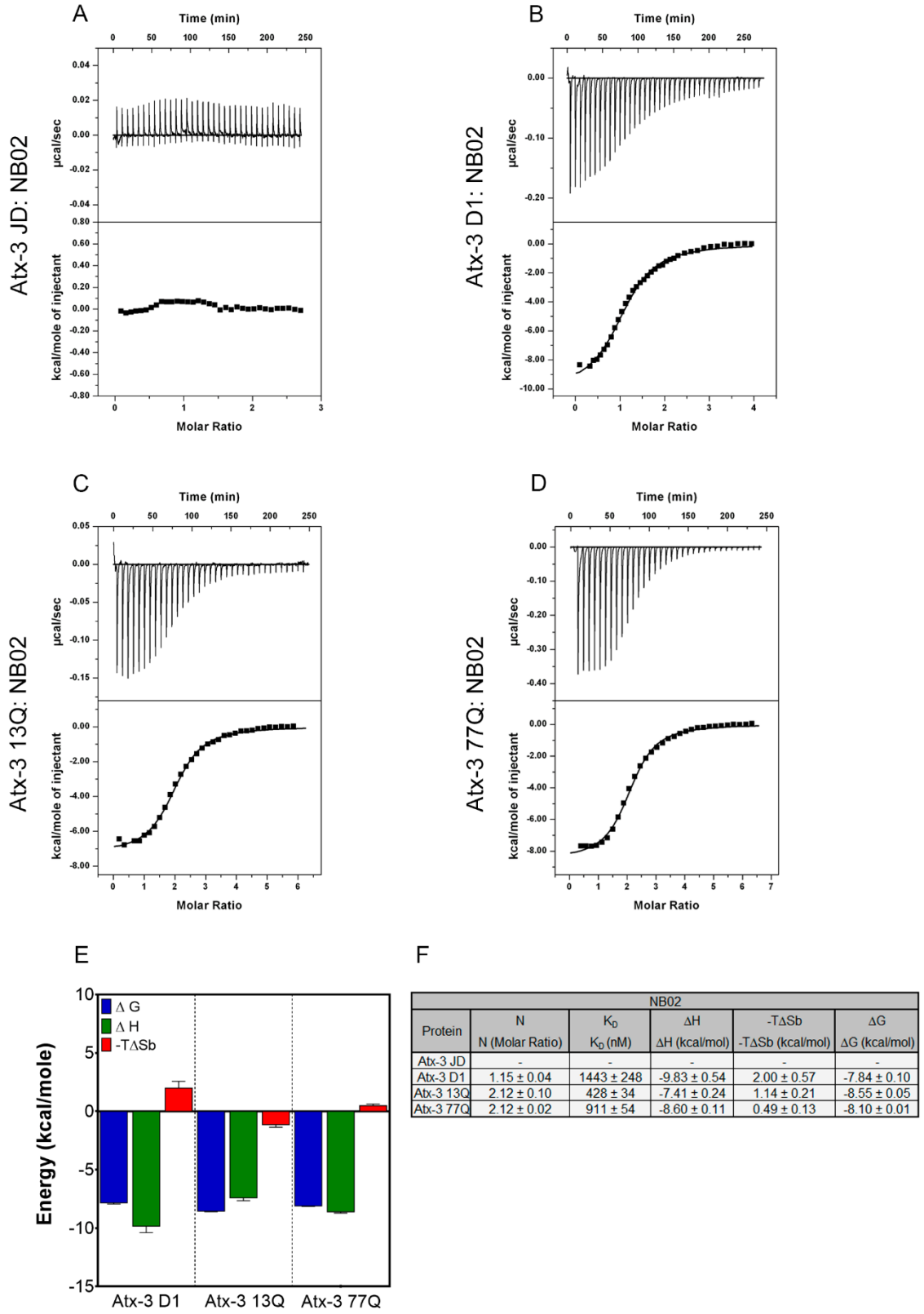

NB02					
Protein	N N (Molar Ratio)	K_D K_D (nM)	ΔH ΔH (kcal/mol)	-TΔSb -TΔSb (kcal/mol)	ΔG ΔG (kcal/mol)
Atx-3 JD	-	-	-	-	-
Atx-3 D1	1.15 ± 0.04	1443 ± 248	-9.83 ± 0.54	2.00 ± 0.57	-7.84 ± 0.10
Atx-3 13Q	2.12 ± 0.10	428 ± 34	-7.41 ± 0.24	1.14 ± 0.21	-8.55 ± 0.05
Atx-3 77Q	2.12 ± 0.02	911 ± 54	-8.60 ± 0.11	0.49 ± 0.13	-8.10 ± 0.01

Figure 21: Thermodynamic profiles of the NB02 interactions with Atx-3 variants analyzed by ITC. A) Atx-3 JD vs NB02, B) Atx-3 D1:NB02, C) Atx-3 13Q:NB02, D) Atx-3 77Q:NB02. Measurement of the heat that is released during the NB02 injections (µcal/seg) and experimental data fitting using a single binding site model. E) Energetic parameters of the complex formation (Atx-3 D1, Atx-3 13Q and Atx-3 77Q) ΔG (blue), ΔH (green) and -TΔS (red). F) ITC parameter values N (molar ratio), K_D, ΔH, -TΔS and ΔG, and error calculation in experiment triplicates.

NB01

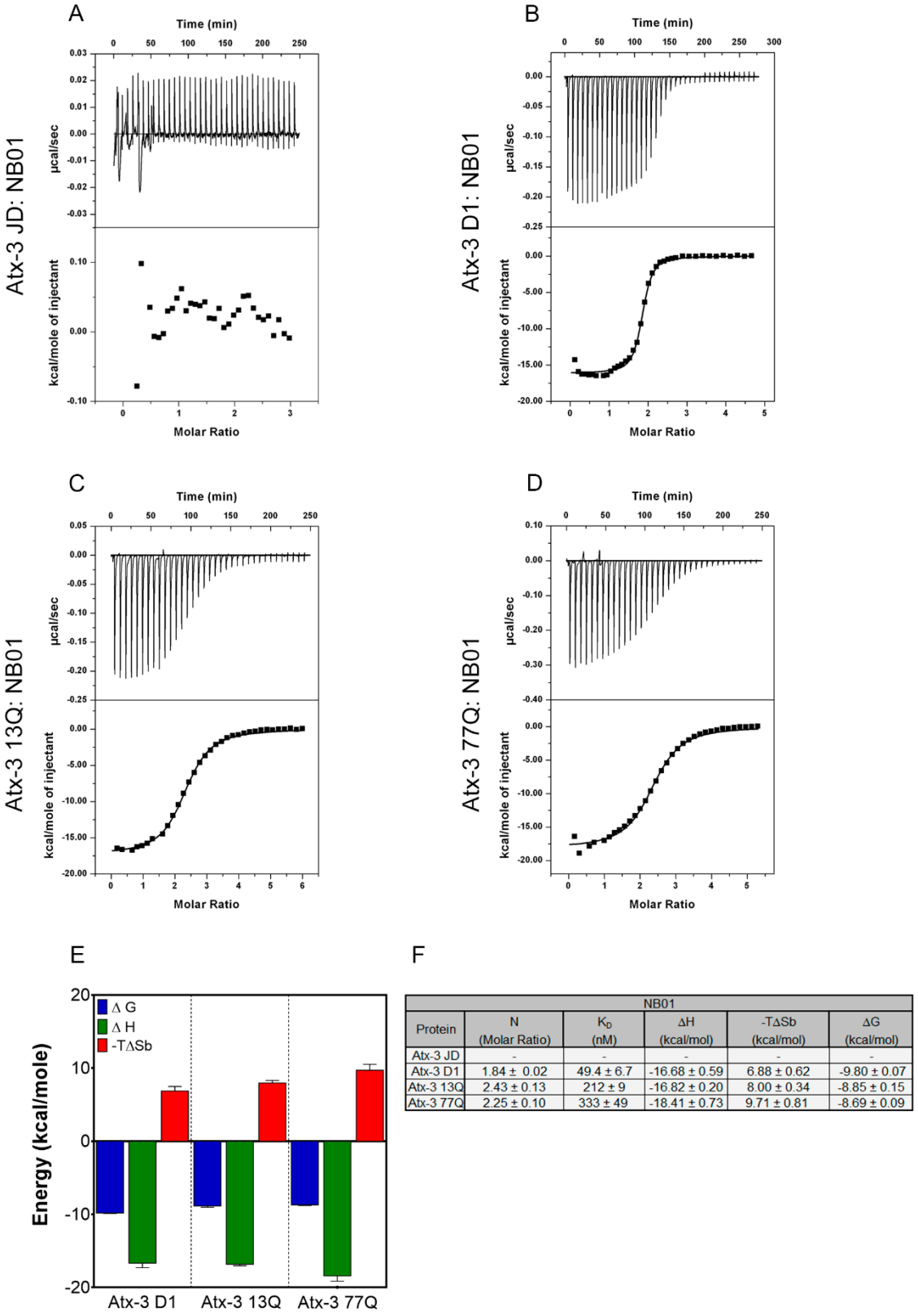

F

NB01					
Protein	N (Molar Ratio)	K_D (nM)	ΔH (kcal/mol)	-TΔSb (kcal/mol)	ΔG (kcal/mol)
Atx-3 JD	-	-	-	-	-
Atx-3 D1	1.84 ± 0.02	49.4 ± 6.7	-16.68 ± 0.59	6.88 ± 0.62	-9.80 ± 0.07
Atx-3 13Q	2.43 ± 0.13	212 ± 9	-16.82 ± 0.20	8.00 ± 0.34	-8.85 ± 0.15
Atx-3 77Q	2.25 ± 0.10	333 ± 49	-18.41 ± 0.73	9.71 ± 0.81	-8.69 ± 0.09

Figure 22: Thermodynamic profiles of the NB01 interactions with Atx-3 variants analyzed by ITC. A) Atx-3 JD vs NB01, B) Atx-3 D1:NB01, C) Atx-3 13Q:NB01, D) Atx-3 77Q:NB01. Measurement of the heat that is released during the NB01 injections (µcal/seg) and experimental data fitting using a single binding site model. E) Energetic parameters of the complex formation (Atx-3 D1, Atx-3 13Q and Atx-3 77Q) ΔG (blue), ΔH (green) and -TΔS (red). F) ITC parameter values N (molar ratio), K_D, ΔH, -TΔS and ΔG, and error calculation in experiment triplicates.

Dynamic Light Scattering

ITC data regarding the complexes formed between NB01 (and NB02) and Atx-3 variants suggested an interaction ratio of 1:2 (1 Atx-3 D1/13Q/77Q molecule for 2 NB01 molecules). As mentioned before this stoichiometry raises some questions, such as: how can a NB recognize two distinct regions of Atx-3, i.e. two epitopes? A dynamic light scattering (DLS) assay was performed in order to enlighten this question.

To proceed to this study Atx-3:NB01 complexes, previously incubated during 90 min in ice, were purified by SEC (Figure 23A, 23B, 23C) followed by DLS analysis with triplicate reading of each condition. Isolated Atx-3 variants and NB01 were also analyzed to compare the results.

Atx-3 is known to be an elongated protein with only a single globular domain and the same evidence is obtained by DLS. Thus, based on the protein radius (nm), the Zetasizer software over-estimates the molecular weight (MW) (kDa) of Atx-3 when compared to the theoretical MW calculated using the amino acidic sequence, since Zetasizer considers, for the calculation, that all proteins are globular. (A comparison between the theoretical and the measured molecular weight is depicted in Figure 23F).

DLS data demonstrate that, as expected, NB01 (black dots) has a smaller particle size than Atx-3 variants or Atx-3:NB01 complexes (Figure 23D, 23E and 23F). However, no major differences are observed between the isolated Atx-3 variants and the corresponding complexes. The DLS peak of Atx-3 variants and of the corresponding Atx-3:NB01 complexes overlap with a very close (Atx-3 13Q vs NB01:Atx-3 13Q, Figure 23E) or even with the same hydrodynamic radius (Atx-3 D1 vs NB01:Atx-3 D1, Figure 23D) (Atx-3 77Q vs NB01:Atx-3 77Q, Figure 23F).

Knowing that the complex is formed (by the SEC purification of the complex), but that there is no major change in size (by DLS results) it can be assumed that the binding of 1 or 2 NB01 leads to the formation of a complex that is closer to the theoretical values (amino acid sequence), indicating the gain of a more compact globular shape in the complex than in the isolated protein.

Contrary to our expectations with this technique, it was not possible to obtain any clarification about the complex Atx-3:NB01 stoichiometry as initially proposed. However, it was possible to acquire additional information that was also quite interesting. The data suggests that the presence NB01 leads to the formation of a complex presenting a more compact globular shape, when comparing to the isolated Atx-3 protein, which is greatly elongated due to the UIMs regions and the polyQ stretch.

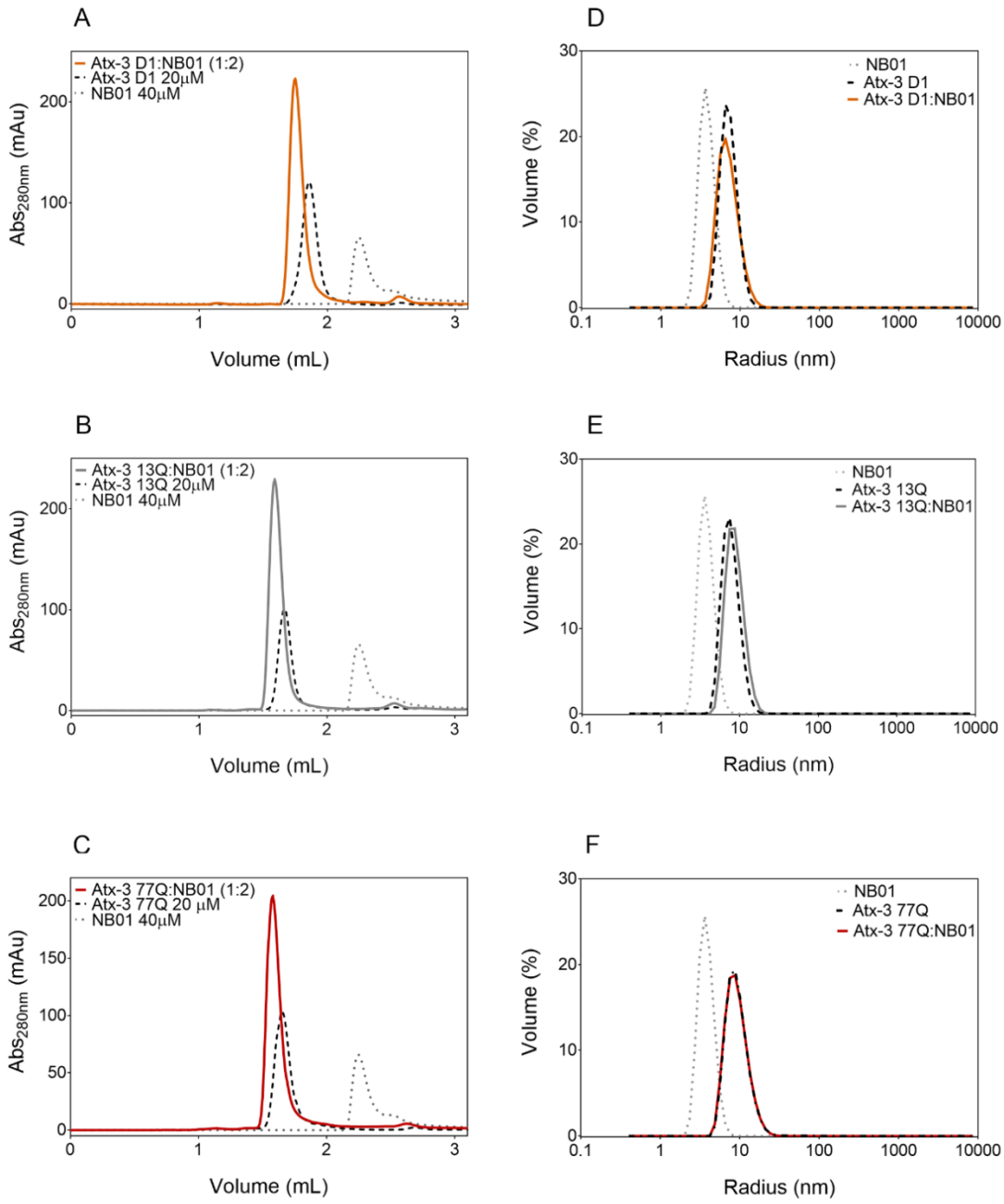

G

	DLS			
Protein	Hydrodynamic Radius (nm)	Apparent DLS MW (kDa)	Theoretical MW (kDA)	PdI
NB01	2.09	18.9	14.16	0.39
Atx-3 D1	3.25	53.1	32.58	0.23
Atx-3 D1:NB01	3.25	53.1	46.74	0.14
Atx-3 13Q	3.77	75.1	43.58	0.32
Atx-3 13Q:NB01	3.96	84.3	57.74	0.07
Atx-3 77Q	4.16	94.6	51.88	0.38
Atx-3 77Q:NB01	4.16	94.6	66.04	0.13

Figure 23: SEC profile and DLS assay of the complex between NB01 and Atx-3 variants. A) Atx-3 D1 (orange), B) Atx-3 13Q (grey) and C) Atx-3 77Q (red) complex formation with NB01 (grey dots) and purifiaction by SEC. There is an overlap of Atx-3 variants and Atx-3:NB01 complexes DLS peak indicating similar particle sizes in D) Atx-3 D1 vs NB01, E) Atx-3 13Q vs NB01 and F) Atx-3 77Q vs NB01. This result indicates that the complex is more compact and globular than the isolated Atx-3 protein. G) Experiment summary, the decreased polydispersity (PdI) in the three complexes may sugest that NB01 may be a useful tool to modulate the aggregation process in Atx-3.

One interesting information obtain by DLS was the Polydispersity Index (PdI) deduced parameter that allows us to estimate the heterogeneity of the particle size distribution in the sample. The closer the PdI value is to zero more monodisperse (uniform) is the sample. The PdI of the isolated Atx-3 constructs (Atx-3 D1, Atx-3 13Q and Atx-3 77Q) demonstrated higher values (0.23, 0.32 and 0.38, respectively) than the corresponding complexes with NB01 (0.14, 0.07 and 0.13, respectively) (Figure 23G).

Therefore, it appears that NB01 increases the stability of Atx-3 conformation avoiding the occurrence of intermediate protein states. This data suggests that NB01 may be a good candidate and a potential tool for the modulation of Atx-3 aggregation and also for its crystallization.

DLS results were inconclusive regarding the stoichiometry of the complex. Small Angle X-ray Scattering (SAXS) was performed to try to clarify this remaining question and hopefully to validate the DLS results.

Small Angle X-ray Scattering

To complement the information obtained by DLS a SEC-SAXS experiment was applied to determine the structural factors radius of gyration (Rg) and maximum intramolecular distance (D_{max}) to acquire more detailed evidence of the size and shape of the complex in solution. With this technique, it would be possible to clarify the stoichiometry of the complex.

To guarantee workable results the Atx-3 13Q and the complexes (Atx-3 13Q:NB01 (1:1) and Atx-3 13Q:NB01 (1:2)) were injected into a gel filtration column and directly measured. The frames of each experiment (Atx-3 13Q, the Atx-3 13Q:NB01 (1:1) and the Atx-3 13Q:NB01 (1:2)) were used to calculate the experimental average scattering curve (colored dots, Figure 24A) that was therefore used for subsequent analysis.

The Guinier plot (Figure 24B) of the scattering data may be used to indicate the presence of aggregated protein. Regarding Atx-3 13Q this may be a restrictive step due to its tendency for amyloid formation. Yet, observing the linearity of the Guinier plot of the scattering data (Figure 24B), the sample was monodisperse and without aggregates in both isolated protein and complex samples. In addition, the radius of gyration (Rg) was estimated to be 38.4 Å, 43.0 Å and 44.1 Å for Atx-3 13Q, Atx-3 13Q:NB01 (1:1) and Atx-3 13Q:NB01 (1:2), respectively. By the addition of molecules, the center of mass (Rg) also increased.

The distance distribution function (Figure 24C), P(r), was calculated and it confirmed the elongated conformation of Atx-3 13Q by the presence of a non--symmetric peak (green line, Figure 24C). Also confirming the DLS results, the NB presence at a ratio of 1:1 (pink line, Figure 24C) and, more evident at a ratio of 1:2 (orange line, Figure 24C), alters the complex to more globular state. This statement is supported by the transition from an elongated curve of Atx-3 13Q (green line, Figure 24C) to a bell-shape curve of 1:1 and 1:2 for the complexes (pink and orange line, Figure 24C). Furthermore, the D_{max} of Atx-3 13Q and the complexes is approximately the same with 185 Å indicating that the Atx-3 13Q length is in fact the longest part of the complex.

Averaged molecular envelopes of fifteen *ab initio* independent models were generated to reconstruct the shape of Atx-3 13Q and the complexes (grey shape in Figure 24D). A value of normalized spatial discrepancy (NDS) below indicates low variability between the models.

Atx-3 13Q and the complex models were generated from the atomic structures of several known domains (PDB accession: JD (1yzb), UIM (2hlz), and C-terminal *(*4wth) and NB (1I3V)) and were fitted into the molecular reconstructions showing an excellent agreement with the experimental scattering curves (black lines, Figure 24A). The best adjusts for the Atx-3 13Q domains complexes with the NB (PBD: 1I3V) are represented in Figure 24D. The envelope of Atx-3 13Q control (1) is represented with the consecutives domains: Josephin domain (blue), UIM (orange) and C-terminal (red). In the complex ratio of 1:1 (2) an additional globular shape is visible corresponding to the presence of NB01. Finally, in the ratio of 1:2 (3) a second globular shape is found corresponding to the second NB.

With this result, the presence of 2 molecules of NB per 1 molecule of Atx-3 13Q is evident. Yet, not all questions were elucidated, it seems that the interaction region between the NB01 with the Atx-3 13Q is very close to the JD but it cannot be confirmed if in fact this interaction is established in this region. Furthermore, the complex fitting with the atomic structure of the Atx-3 13Q and the 2 molecules of NB01 is not totally clear whether both NB bind to Atx-3 at two distinct sites or if one of the NB is only binding to the other, and not to Atx-3.

To try to clarify these remaining questions a last attempt was made: crystallization trials of the complex between NB01/NB02 (the binding of two of these NB per Atx-3 was determined by ITC) with Atx-3.

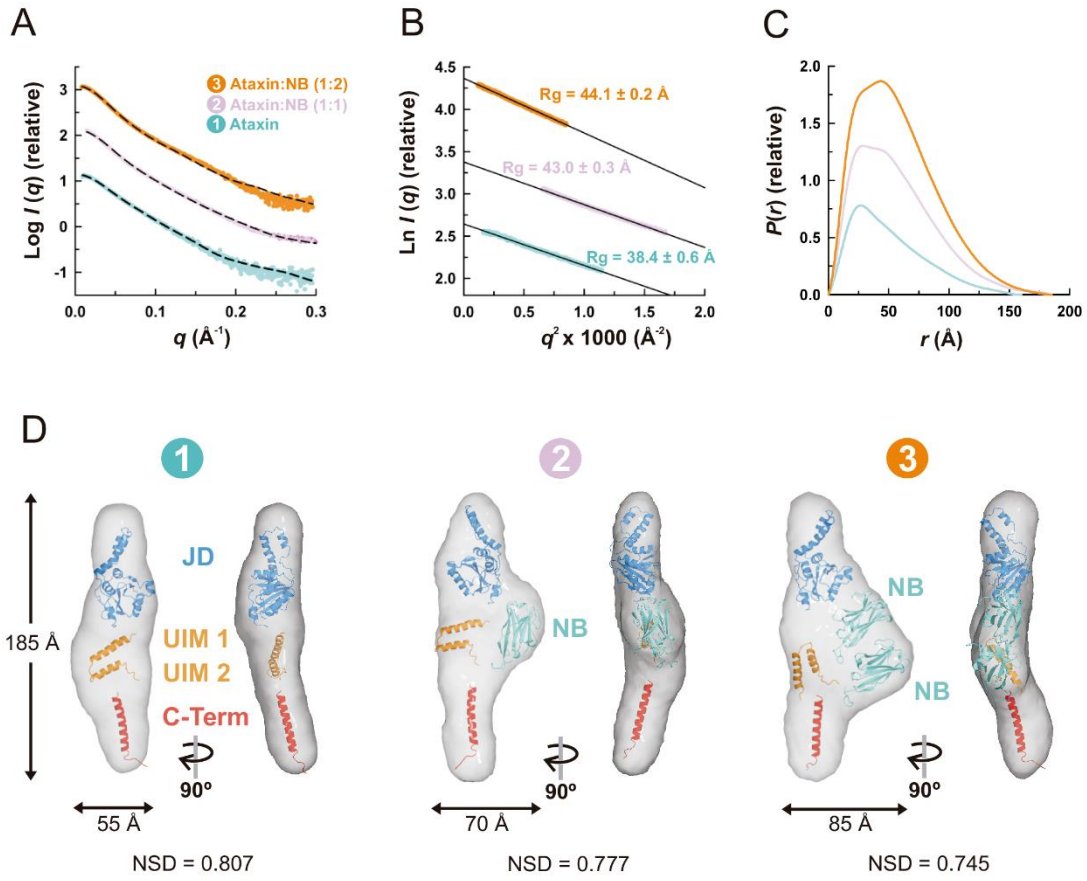

Figure 24: Small angle X-ray scattering coupled to a SEC column (SEC-SAXS) experiment for Atx-3 13Q:NB01 complex. A) Experimental average scattering curves (color dots) with the respective legend above and the fitting of *ab initio* reconstruction in black lines. Atx-3 13Q (green), Atx-3 13Q:NB01 (1:1) (pink) and Atx-3 13Q:NB01 (1:2) (orange). B) Guinier plot of the scattering curve presenting a monodispersed sample (3 experiments) and calculation of Rg with 44.1 A, 43.0 A and 38.4 A for Atx-3 13Q (green), Atx-3 13Q:NB01 (1:1) (pink) and Atx-3 13Q:NB01 (1:2) (orange), respectively. C) Distance distribution function with Atx-3 13Q (green line) presenting an elongated profile. The presence of NB01 turns the complex more globular (pink and orange lines). Determination of maximum distance of Atx-3 13Q and both complexes with 185 A. D) *Ab initio* shape reconstruction (grey) of (1) Atx-3 13Q and complexes (2) 1:1 and (3) 1:2. The atomic structures (PDB accession: JD (1yzb) (blue), UIM (2hlz) (orange), and C-terminal (4wth (red) and NB (1I3V) (green)) were adjusted into the molecules shape with CORAL. NSD demonstrate the molecules flexibility in solution.

Thermal Shift Assay (Sypro Orange)

One of the goals for the study of Atx-3 binding NBs was to use them as a crystallization chaperones to stabilize the monomeric Atx-3 protein, facilitate the formation of Atx-3 crystals and subsequently determine its three-dimensional structure. To detect if any of the selected NB (with a molar ratio of 1:2) are able to stabilize Atx-3, a Thermal Shift Assay was performed with NB01 and NB02.

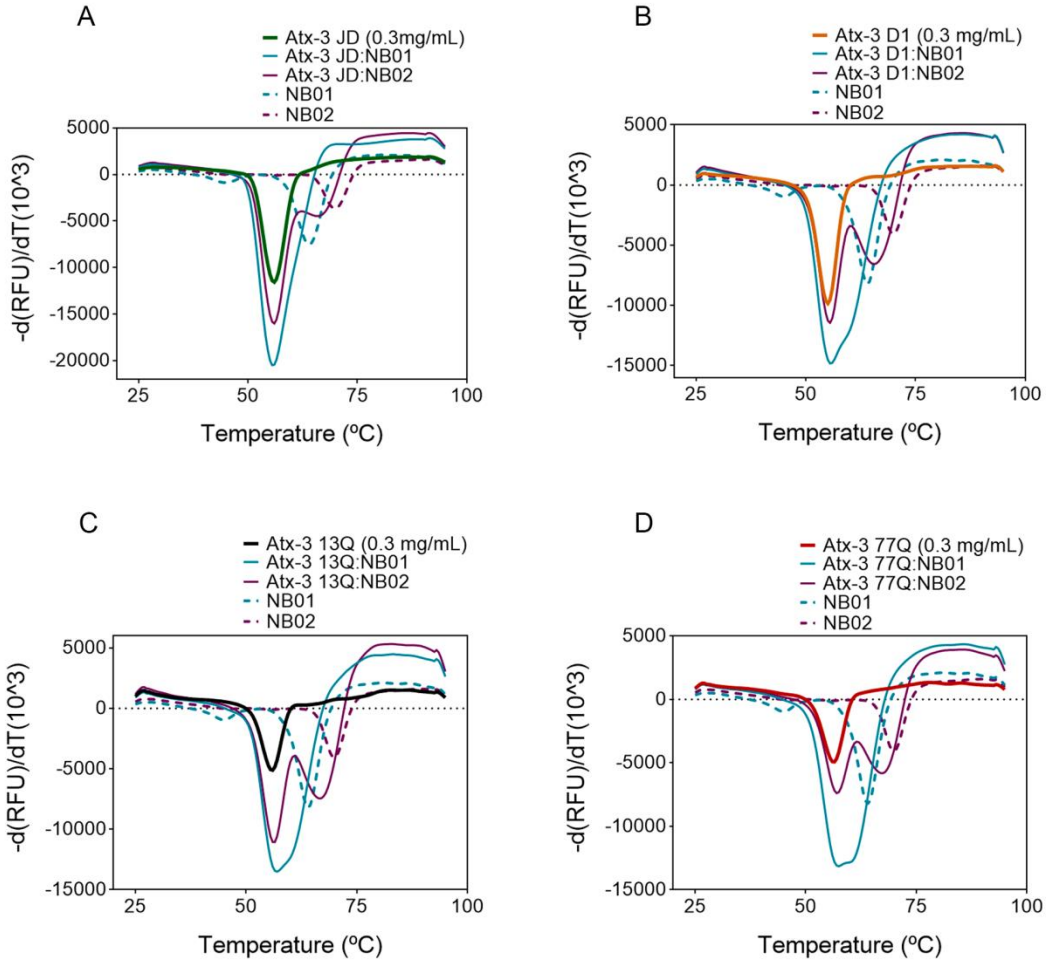

E

Thermal Shift Assay	
Protein	Melting Temperature ºC
NB01	64 ± 0
NB02	70 ± 0
Atx-3 JD (0.3 mg/mL)	56 ± 0
Atx-3 JD:NB01 (1:5)	55.5 ± 0
Atx-3 JD:NB02 (1:5)	55.83 ± 0.3
Atx-3 D1 (0.3 mg/mL)	55 ± 0
Atx-3 D1:NB01 (1:5)	55.5 ± 0
Atx-3 D1:NB02 (1:5)	55.5 ± 0
Atx-3 13Q (0.3 mg/mL)	55.8 ± 0.3
Atx-3 13Q:NB01 (1:5)	57 ± 0
Atx-3 13Q:NB02 (1:5)	56.3 ± 0.3
Atx-3 77Q (0.3 mg/mL)	56.3 ± 0.3
Atx-3 77Q:NB01 (1:5)	57.2 ± 0.3
Atx-3 77Q:NB02 (1:5)	57.2 ± 0.3

Figure 25: Thermal Shift Assay with Atx-3 variants and NB01 or NB02. Atx-3 constructs were incubated with NB01 or NB02 to analyze differences in the melting temperatures by measuring the emission of Sypro Orange fluorophore with temperature (result derivative). A) Atx-3 JD (green line), Atx-3 JD with NB01 (blue line), NB01 control (blue dots), Atx-3 JD with NB02 (purple line) and NB02 (purple dots). B) Atx-3 D1 domain (orange line), Atx-3 D1 with NB01 (blue line), NB01 control (blue dots), Atx-3 D1 with NB02 (purple line) and NB02 (purple dots). C) Atx-3 13Q domain (black line), Atx-3 13Q with NB01 (blue line), NB01 control (blue dots), Atx-3 13Q with NB02 (purple line) and NB02 (purple dots). D) Atx-3 77Q domain (red line), Atx-3 77Q with NB01 (blue line), NB01 control (blue dots), Atx-3 13Q with NB02 (purple line) and NB02 (purple dots). E) Melting temperature summary.

The thermal shift assay quantifies the protein stability by monitoring its denaturation temperature. A good ligand/chaperone for crystallization may increase the protein thermal stability and consequently increase the protein denaturation temperature. SYPRO Orange is a fluorophore that binds, nonspecifically, to hydrophobic surfaces. With the protein denaturation more hydrophobic surfaces are exposed increasing the dye binding and enhancing its fluorescence. The melting temperature (TM) is easily determined by plotting the first derivate of the raw data and finding its minimum.

Using this method, small differences were detected but no great evidence of an induced stabilization of Atx-3 by the NBs was observed (Figure 25).

Complex Crystallization

Even thought it was not possible to obtain relevant data from the thermal shift assay, crystallization trials of Atx-3:NB complexes were performed using commercial crystallography screening kits and a Oryx4 Crystallization robot.

Different kits and protein-to-precipitant ratios were tested as described in Methods. Crystals were obtained in several crystallization conditions. However, most of the crystals proved to be salt crystals. Nonetheless, in a condition of the crystallization screen Index HT (Hampton Research) (25% PEG 3,350 and 0.1M Tris pH 8.5) Atx-3 D1:NB01 complex crystals were obtained (Figure 26).

Figure 26: Crystal of Atx-3 D1 variant with NB01. Crystals of Atx-3 D1 domain complexed NB01 at 28 mg/mL; Condition: 25% PEG 3,350 and 0.1M Tris pH 8.5, 0.2μL of protein and 0.1 μL of crystallization buffer in sitting drop plate.

With the aim to obtain larger crystals a scale-up process was tried by fine tuning around the buffer pH and precipitant concentration. Efforts are still currently being made to reproduce these crystallization conditions.

Nanobodies as Modulators of Atx-3 Aggregation

Before each aggregation assay, separately Atx-3 variant were repurifed to exchange buffer to aggregation buffer (without glycerol, which delays aggregation) and to remove possible Atx-3 aggregates and intermediate oligomeric species in solution formed during the freezing and thawing processes (Figure 27).

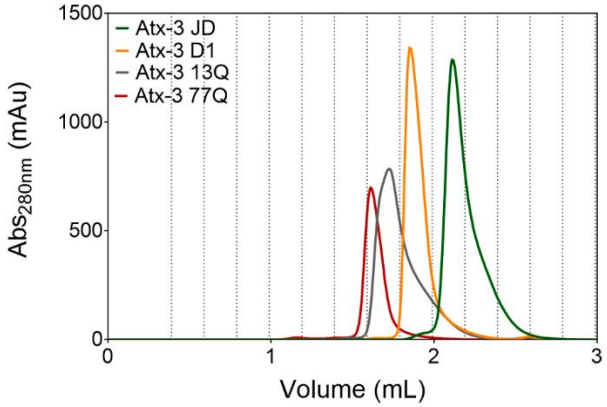

Figure 27: Repurification of Atx-3 variants by size exclusion chromatography to remove possible protein aggregates and glycerol from the buffer. Protein elution volumes (mL) monitored by absorbance measurement at 280 nm. The elution fractions are represented in dotted lines. From the lowest to the highest elution volume are the Atx-3 77Q (red line), Atx-3 13Q (black line), Atx-3 D1 (orange line) and Atx-3 JD (green line) variants.

The NBs previously characterized (NB03, 02, 05, 01) were incubated with Atx-3 variants to study their affect in the aggregation. The following techniques were used as complementary procedures to fully characterize the details of Atx-3 aggregation in the presence of these NBs.

The impact of the incubation of the NBs with Atx-3 variants was monitored using a ThT fluorescence assay. This technique allows the detection of differences in the lag phase upon incubation with NBs and to study changes in the elongation mechanism (aggregation curve). At the endpoint of the ThT assay a Filter Retardation Assay was used to study changes in the insoluble mature fibers caused by the NBs followed by a dot-blot to analyze the presence of toxic species using different antibodies as reporters, such as anti-A11 (recognizes toxic oligomers in other amyloid disorders) and Anti-OC (for fibril recognition). To study changes in the morphology of the fibrils Transmission Electron Microscopy (TEM) visualization of the endpoint samples was performed.

To directly observe the effect of the most promising NBs (and the most effective ratios) in the soluble forms of Atx-3 during the dimerization and oligomerization processes a SEC time course assay was used. Additionally, in order to study the average size distribution of the species in solution during aggregation DLS was used as well. The effect of each NB in Atx-3 aggregation is presented individually.

NB03 NB03 was previously used as a negative control in the characterization of the Atx-3:NB interaction so it was interesting to study the effect of a NB that does not present any binding interaction with Atx-3 variants in their aggregation. Observing Figure 28 the presence of NB03 surprisingly leads to a delay of aggregation of all Atx-3 variants. Since there is no binding interaction, this inhibition may be caused by the increased number of molecules in solution leading to molecular crowding. An interesting effect is the earlier aggregation start of the highest concentration of NB comparing with the lower ones. This result may be explained by a change in sample conductivity caused by the NB, facilitating the start of aggregation. However, this is only a hypothesis and further experiments must be made to understand this behavior.

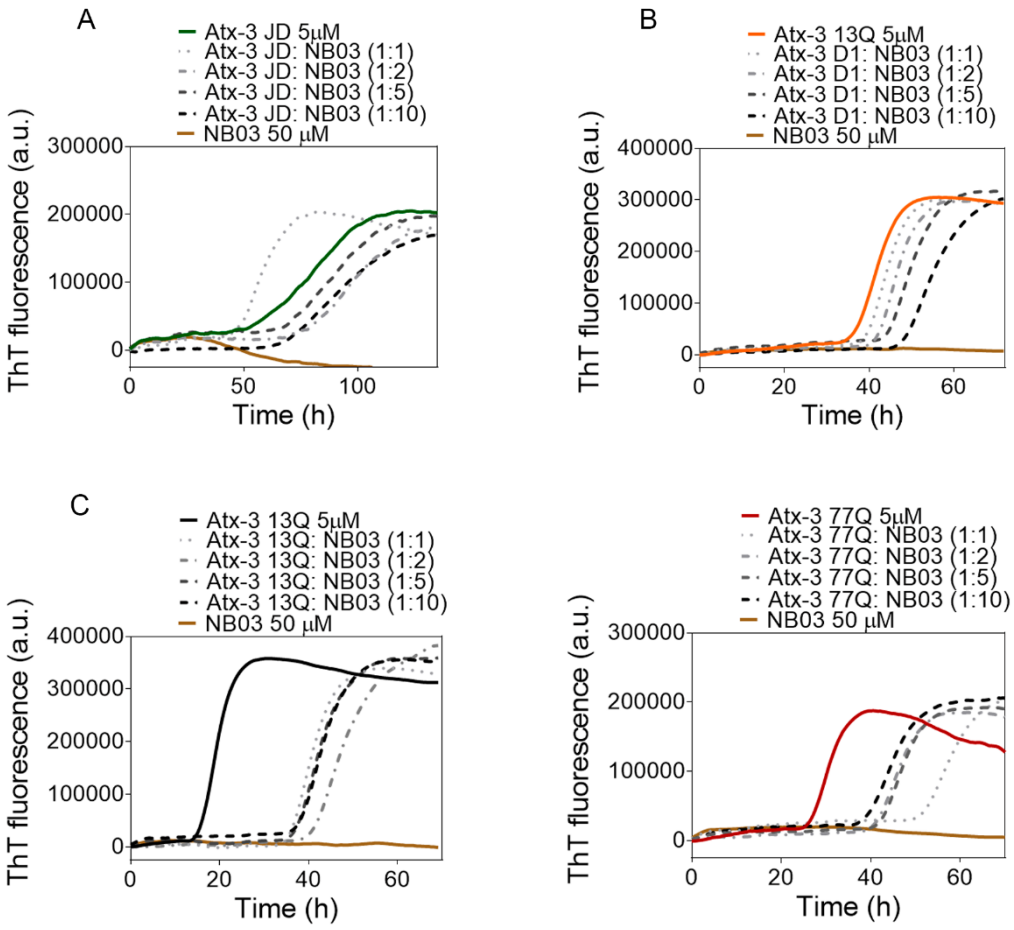

Figure 28: Modulation of 5 μM Atx-3 isoforms aggregation by NB03 visualized by a ThT assay. Each plot displays the results of the aggregation assay for each isoform incubated with different ratios of NB03, as well as the negative controls (Atx-3 isoform alone). The legend corresponding to each sample is shown above the corresponding graphic. The plots presented were obtained by means of triplicates.

With the aim of studying the effect of NB03 besides the delay in the Atx-3 aggregation a Filter Retardation Assay was used to observe its effect in the fibril species present at the ThT experiment endpoint.

Atx-3 JD formed soluble species in the experiment endpoint (aggregates are mostly soluble/small than the membrane cut-off (0.2 μm)) since they are not retained in the membrane and the insoluble oligomeric species formed by Atx-3 D1, Atx-3 13Q and Atx-3 77Q (Figure 29A) are not changed upon incubation with NB03. The same information is obtained regarding the protofibrils/fibrils of Atx-3 JD, Atx-3 D1 and Atx-3 13Q as well as the mature amyloid fibrils of Atx-3 77Q (Figure 29B).

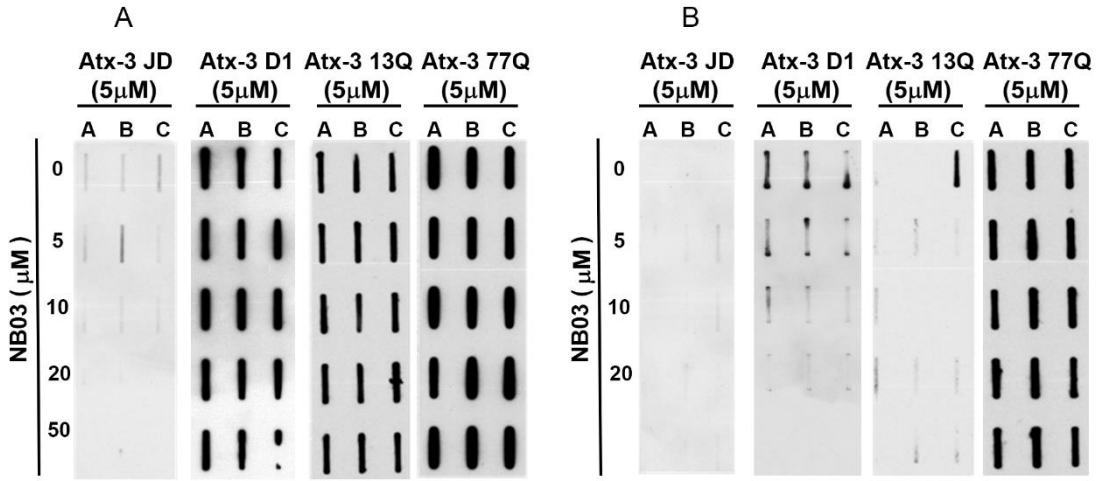

Figure 29: Filter Retardation Assay of endpoint samples from ThT aggregation assay of Atx-3 isoforms incubated with NB03. A) Filter retardation Assay without SDS-treatment, Atx-3 JD shows soluble oligomeric species while Atx-3 D1, Atx-3 13Q and Atx-3 77Q shows insoluble oligomeric species without changes in the presence of NB03. B) Filter Retardation Assay with SDS treatment, Atx-3 JD, Atx-3 D1 and Atx-3 13Q exhibit protofibrils/fibrils without change with the presence of NB03 and the mature amyloid fibrils of Atx-3 77Q are also not affected by the presence of NB03. The signal was obtained by recognition of total protein in the membrane by antibody 1H9.

Furthermore, to study if other toxic species such as oligomers and protofibers are formed during the aggregation process, a dot-blot assay was performed. The samples absorbed in the membrane were recognized by the anti-OC and anti-A11 antibodies. In the case of NB03, no major changes were observed (Figure 30).

Overall, the results obtained using NB03 suggest a basal lag phase retardation, possibly due to an increase in molecular crowding, since this NB was initially demonstrated to be unable to interact directly with Atx-3 constructs. An odd information was acquired with the highest concentration of NB03 used (1:10 ratio) which led to a decrease of Atx-3 lag phase. Additional ThT assays are needed to prove if this was an isolated result or a recurrent effect in the presence of higher concentrations of NBs. No changes were detected in the mature fibers of Atx-3 77Q nor in the toxic species recognized by Anti-A11 and Anti-OC.

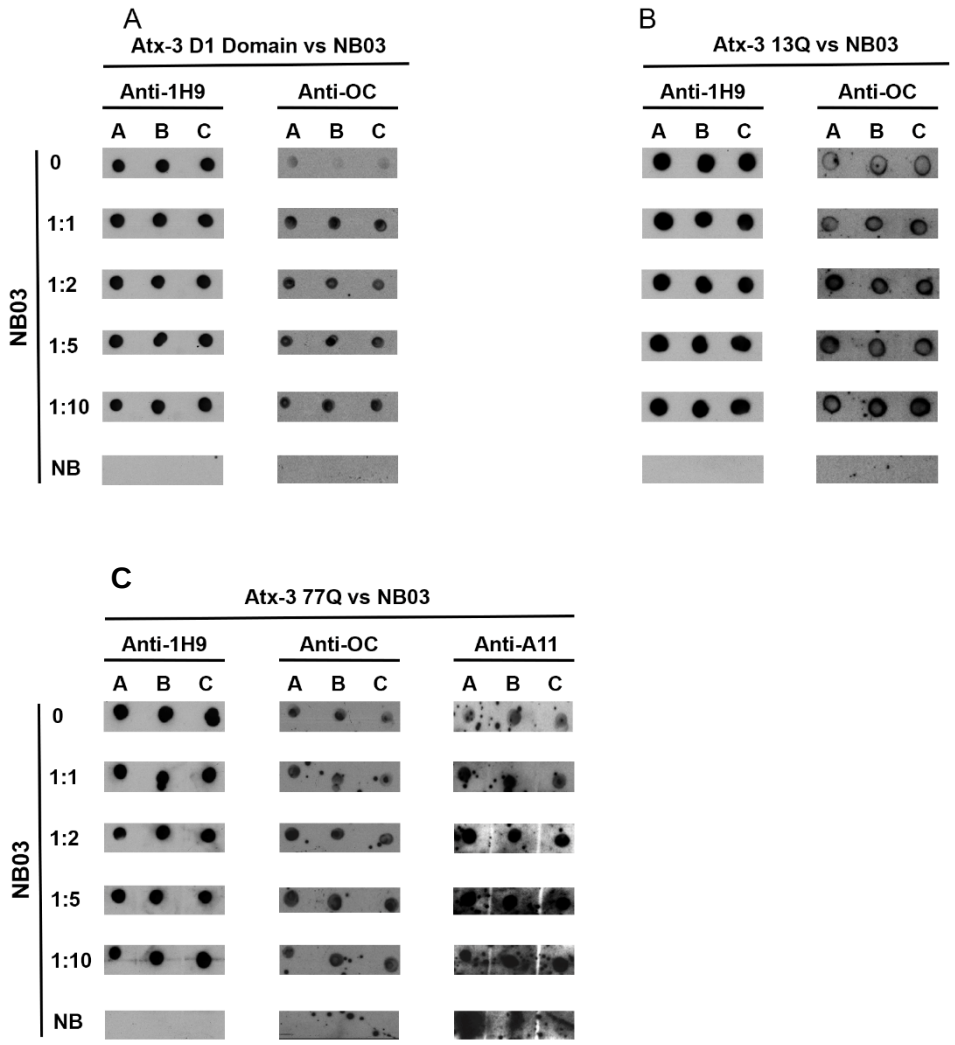

Figure 30: Dot-blot Assay of Atx-3 incubated with NB03. The endpoint samples of ThT assay were used in a Dot Bolt assay. The membrane was incubated with different antibodies: Antibody 1H9 (that recognizes the total Atx-3 protein loaded), an anti-OC antibody (that recognizes amyloid fibrils/protofibrils) and an anti-A11 antibody (that recognizes toxic oligomers). A) Dot-blot of Atx-3 D1 with NB03 recognition by anti-1H9 and anti-OC. B) Dot Bolt of Atx-3 13Q with NB03 recognition by anti-1H9 and anti-OC. C) Dot Bolt of Atx-3 77Q with NB03 recognition by anti-1H9, anti-OC and anti-A11. There are no major changes in the antibody recognition.

NB02 ITC showed that NB02 interacts with Atx-3 D1, Atx-3 13Q and Atx-3 77Q (presenting the lowest affinity of all NB tested) without interacting with Atx-3 JD. Still, the ThT assay showed that this NB delays aggregation of Atx-3 constructs. This effect appears to be dose dependent (the higher the ratio, the higher the effect). However, the inhibitory effect on the aggregation saturates at a ratio of 1:5 (Atx-3 to NB02). Furthermore, NB02 has a much higher impact in Atx-3 13Q (Figure 31C) and Atx-3 77Q (Figure 31D) when compared with the truncated variant Atx-3 D1. Other than an increased lag-phase, there is no apparent change in the profile of the aggregation curve indicating that the elongation proceeds as usual.

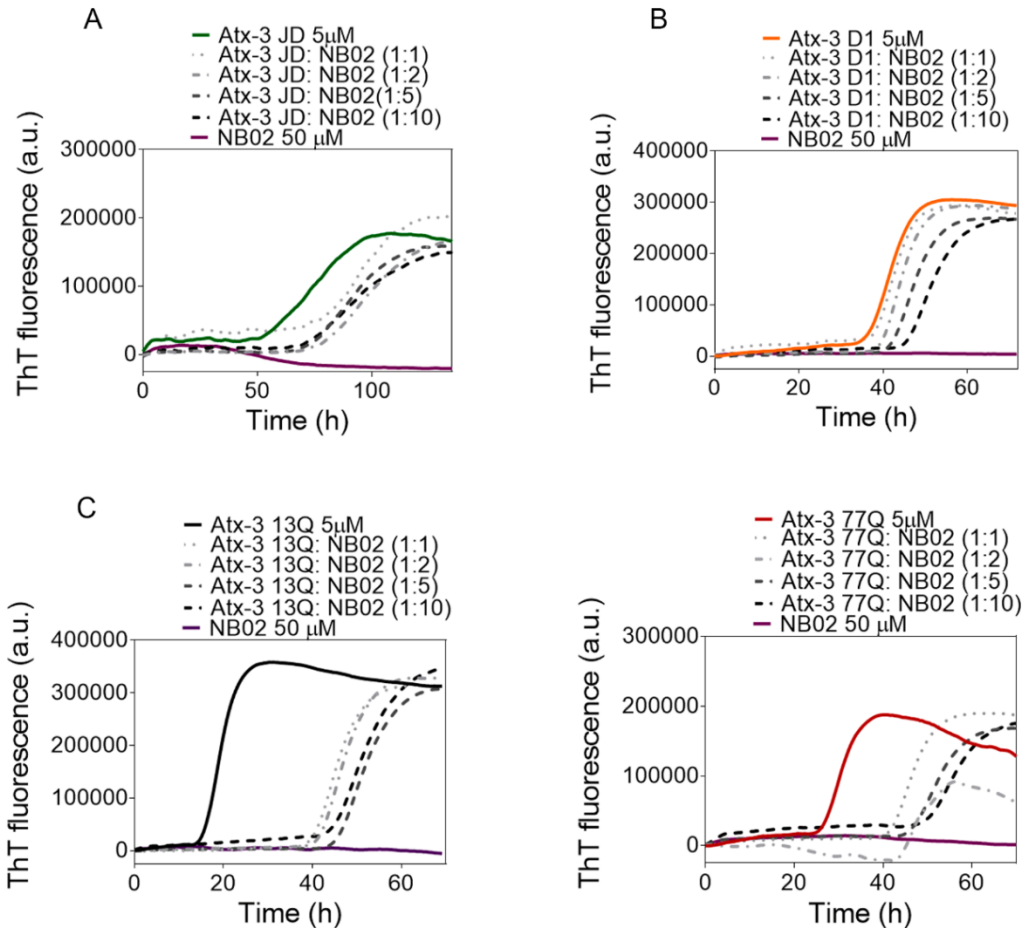

Figure 31: Modulation of 5 µM Atx-3 aggregation by NB02, visualized by a ThT assay. Each plot displays the results of the aggregation assay for each variant incubated with different ratios of NB02, as well as the negative controls (Atx-3 variant alone). The legend corresponding to each sample is shown above the corresponding graphic. The plots presented were obtained by means of triplicates.

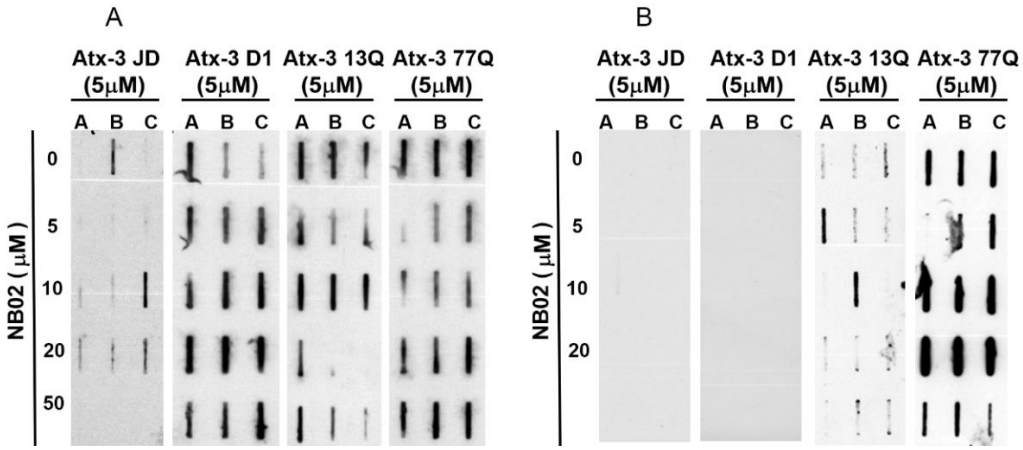

Figure 32: Filter Retardation Assay of endpoint samples from ThT aggregation assay of Atx-3 variants in the presence of NB02. A) Filter retardation Assay without SDS-treatment, Atx-3 JD show soluble oligomeric specie, while Atx-3 D1, Atx-3 13Q and Atx-3 77Q show insoluble oligomeric species, both without changes in the presence of NB02. B) Filter Retardation Assay with SDS treatment, Atx-3 JD, Atx-3 D1 and Atx-3 13Q show protofibrils/fibrils without any change with the presence of NB02 while the mature amyloid fibrils Atx-3 77Q are affected by the NB02 presence. The signal was obtained by recognition by antibody 1H9.

In opposition of NB03 results, NB02 presence modulates the amount of insoluble amyloid mature fibers of Atx-3 77Q (Figure 32B). As previously stated (see Introduction), mature fibers are in fact a final amyloidogenic structure that protects the cell from intermediate toxic species. These toxic oligomeric species are now believed to be the true cause for the neurodegeneration associated with this disease. It is therefore necessary to evaluate if NB02, which prolongs the lag phase, affects the abundance of these toxic species.

The results shown in Figure 33 indicate that the recognition patterns of the Anti-OC and Anti-A11 antibodies are quite similar between the control samples and the NB incubation.

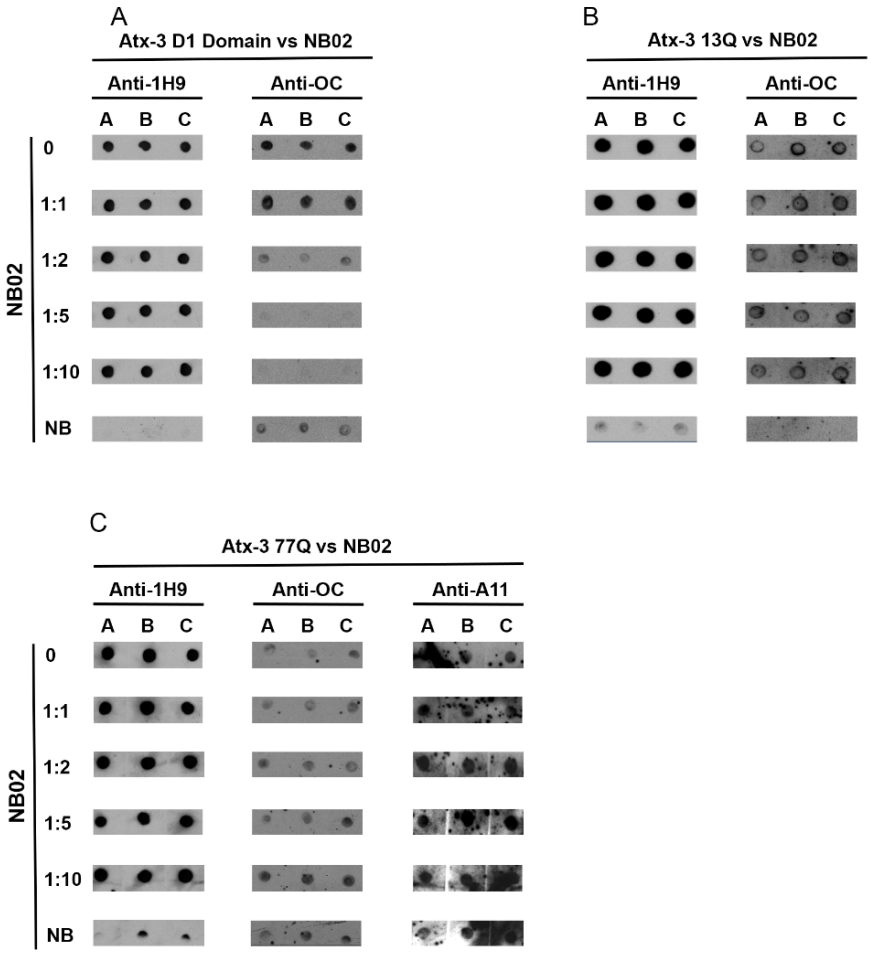

Figure 33: Dot-blot Assay incubated with NB02. The endpoint samples of ThT assay were used in a Dot Bolt assay. The membrane was incubated with different antibodies., Antibody 1H9 (that recognizes the total Atx-3 protein loaded), an anti-OC antibody (that recognizes amyloid fibrils/protofibrils) and an Anti-A11 antibody (that recognizes toxic oligomers). A) Dot-blot of Atx-3 D1 with NB02 recognition by Anti-1H9 and Anti-OC. B) Dot Bolt of Atx-3 13Q with NB02 recognition by Anti-1H9 and Anti-OC. C) Dot Bolt of Atx-3 77Q with NB02 recognition by Anti-1H9, Anti-OC and Anti-A11. There are no major changes in the antibody recognition.

An interesting aspect of this result was the fact that NB02 alone (control) was also recognized by the Atx-3 antibodies (Anti-OC and Anti-A11). Finally, a third antibody was also used (1H9) as a load control for the detection of total Atx-3 as a positive control and this antibody also recognizes NB02.

NB05 The study of the effect of this NB (which showed the second highest affinity to Atx-3) on the aggregation process of Atx-3 consisted on the same steps as the NBs described so far. Results show that Atx-3 JD, Atx-3 D1 and Atx-3 13Q (Figure 34A, 34B and 34C) aggregation is not greatly affected by the presence of NB05 which seems to only have a basal effect (similar to the effect showed on the NB03 studies). However, taking in account the fact that the aggregation of Atx-3 77Q, the pathological variant of Atx-3, was highly affected by NB05 (Figure 34, 3-fold increase in lag phase), it can still be considered as a promising tool to modulate the aggregation of this protein.

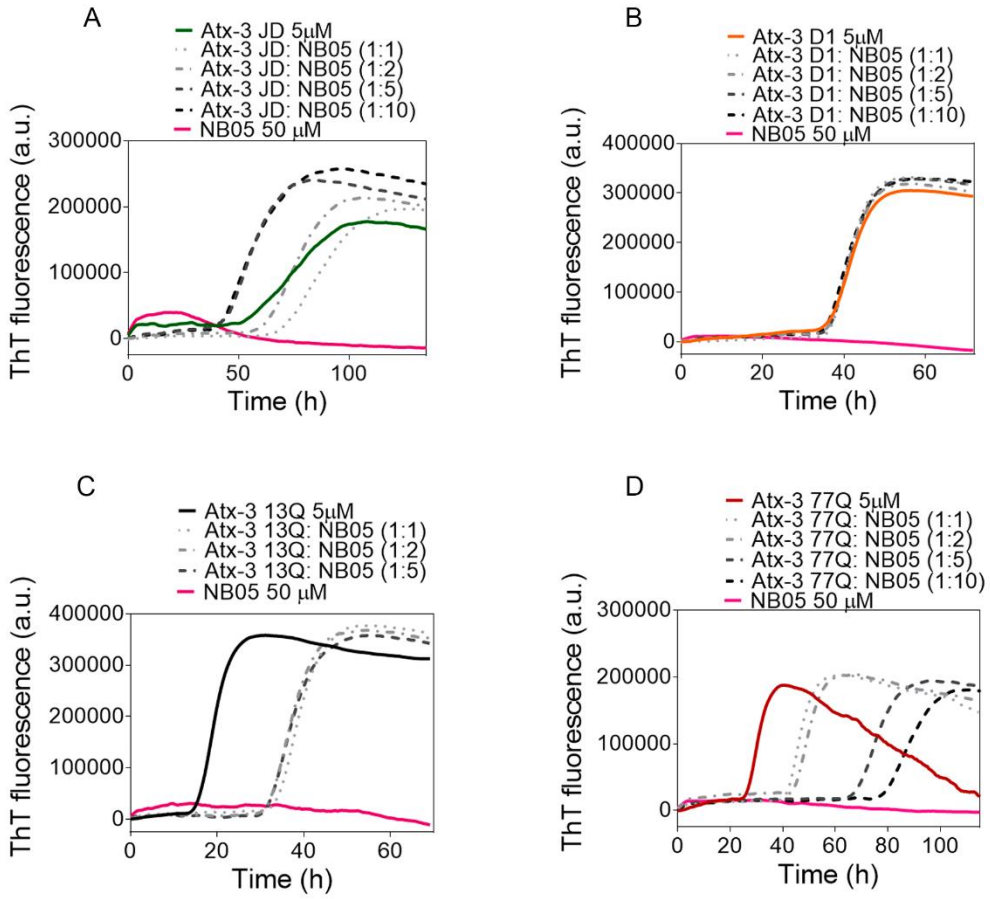

Figure 34: Modulation of 5 μM Atx-3 isoforms aggregation by NB05, visualized by a ThT assay. Each plot displays the results of the aggregation assay for each isoform incubated with different ratios of NB05, as well as the negative controls (Atx-3 isoform alone). The legend corresponding to each sample is shown above the corresponding graphic. The plots presented were obtained by means of triplicates.

Considering that NB05 showed a small effect on Atx-3 13Q (similar to NB03), the ability to selectively delay the aggregation of Atx-3 77Q makes it a promising subject in the search for a modulator of Atx-3 aggregation in the pharmacology of the disease.

Analyzing the results of the dot-blot assay for Atx-3:NB05 complexes (Figure 35), there is also no apparent increase in the production of toxic oligomeric and protofibrils forms, when compared to the control samples. The anti-OC and anti-A11 antibodies recognized the presence of some species, but the signal was not increased by the presence of NB05. The study of this NB is an ongoing work so additional experiments and validation assays are still needed.

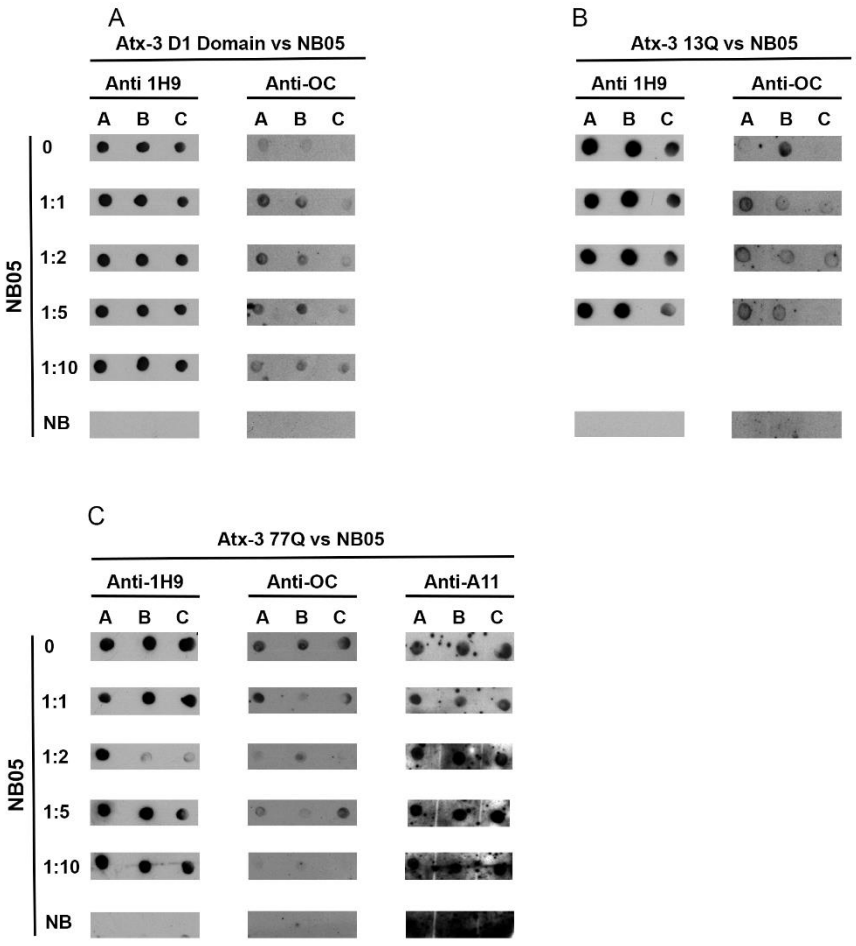

Figure 35: Dot-blot Assay of Atx-3 incubated with NB05. The endpoint samples of ThT assay were used in a Dot Bolt assay. The membrane was incubated with different antibodies: Antibody 1H9 (that recognizes the total Atx-3 protein loaded), an anti-OC antibody (that recognizes amyloid fibrils/protofibrils) and an anti-A11 antibody (that recognizes toxic oligomers). A) Dot-blot of Atx-3 D1 with NB05 recognition by anti-1H9 and anti-OC. B) Dot Bolt of Atx-3 13Q with NB05 recognition by anti-1H9 and Anti-OC. C) Dot Bolt of Atx-3 77Q with NB05 recognition by anti-1H9, anti-OC and anti-A11. There are no major changes in the antibody recognition.

The ability of this NB to specifically modulate the aggregation of Atx-3 77Q was explored with additional assays to understand the soluble forms that are generated during the aggregation both in the presence and absence of NB05.

Size Exclusion Chromatography Time course (Atx-3 77Q:NB05)

In the first aggregation assay timepoint (0 hours) (Figure 36A) it is visible that Atx-3 77Q is mostly monomeric (fraction 7) and then progressively evolves into the HMW oligomeric species peak (fraction 4/5). In some points of the Atx-3 77Q aggregation pathway (Figure 36G) the presence of intermediary oligomeric species (dimers and low molecular weight oligomers in fraction 6) is traceable. Along the amyloid formation process, total Atx-3 77Q absorbance decreases due to sample filtration and consequent retention of insoluble fibrils. At 140h (Figure 36H) there are no monomeric species of Atx-3 77Q present.

In the first injection (0 hours) the complex Atx-3 77Q:NB05 (1:10) is composed solely by the monomeric fraction (fraction 7). Oligomerization process seems to start at the same time for Atx-3 77Q both with and without NB05 (around 40 to 72 hours of incubation). Yet, after 92 or 140 hours Atx-3 77Q evolves very quickly into the HMW oligomeric species peak (fraction 4/5) while the Atx-3 77Q:NB05 complex seems to remain in the monomeric form. Ultimately, in the last injection (166 hours in), Atx-77Q alone is already completely aggregated while the Atx-3 77Q:NB01 (1:10) complex is still partially in the monomeric form.

Soluble intermediates are formed in both Atx-3 77Q control and Atx-3:NB05 complex samples.

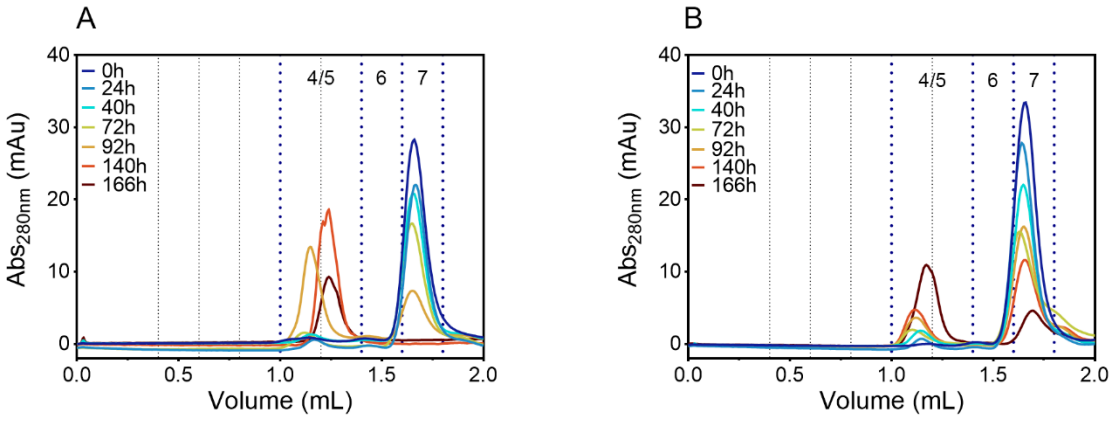

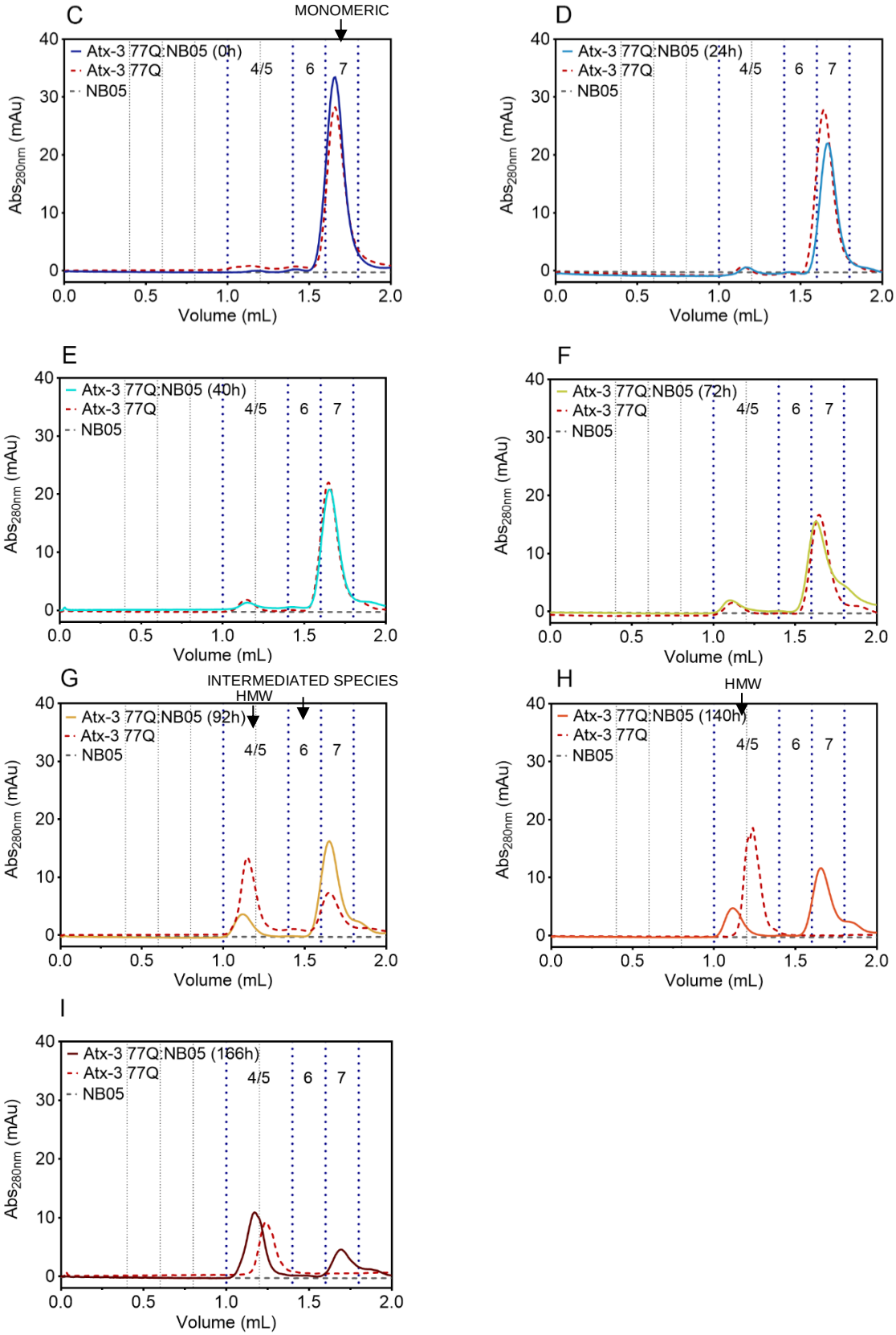

Figure 36: Modulation of the aggregation of 5μM Atx-3 77Q by incubation with NB05 (1:10). Size Exclusion Chromatography analysis at different time points indicated by different colors. A) Atx-3 77Q control, B) Complex of Atx-3 77Q and NB05 (1:10). Aggregation comparison between Atx-3 77Q and the complex: C) 0 h, D) 24 h, E) 40 h, F) 72 h, G) 92 h, H) 140 h, I) 166 h. Aggregation is delayed by the presence of NB05.

Thus, NB05 presents very promising results for the specific modulation of Atx-77Q aggregation without affect the normal isoform (Atx-3 13Q). Still, more experiments need to be performed to verify if the soluble intermediary species that are prolonged in the NB05 presence increase the cellular toxicity.

NB01 The effect of NB01, the NB with the highest affinity, in the modulation of Atx-3 variants is presented in Figure 37. Even though no interaction between NB01 and Atx-3 JD was observed by SEC and ITC, ThT aggregation assay shows an apparent delay in Atx-3 JD aggregation in the presence of NB01 in a molar ratio of 1:1 (grey dots) and 1:2 (grey dots and lines) (Figure 37A). Regarding the Atx-3 isoforms to which NB01 presented high affinity, a delay in the aggregation lag phase with the same molar ratios was also noticed, especially in the full-length isoforms Atx-3 13Q and Atx-3 77Q.

Between the molar ratio of 1:1 and 1:2 the increase in the lag-phase of aggregation appears to be dose dependent. Remarkably, using a molar ratio of 1:2, the lag phase of the Atx-3 13Q and Atx-3 77Q is extended twofold comparing to the isolated proteins (Figure 37C and 37D). With the molar ratio of Atx-3:NB01 of 1:5 and 1:10 (dark grey lines), the lag phase is still longer than the control (without NB01) but is strangely shorter than for the ratios 1:1 and 1:2, similar to the result displayed with NB03.

Besides the increase in the lag phase period, the curve profile has no other apparent change (Figure 37), pointing to the idea that although NB01 delays Atx-3 primary nucleation it does not affect the elongation process of aggregation just as the other NBs (NB02 and NB05).

Further information was needed before selecting NB01 as a good Atx-3 anti-aggregation agent. For example, it was necessary to characterize the oligomeric species formed throughout the aggregation process in the presence of the NB01. It was also necessary to study if besides extending the aggregation lag-phase this NB can also prevent the formation of toxic oligomeric species.

As expected, the protofibrils/fibrils formed during the aggregation process of Atx-3 JD, D1 and 13Q are non-mature and SDS-sensitive (Figure 38B), due to the absence of the polyQ extension. Consequently, they are not retained in the membrane. Insoluble aggregates formed by Atx-3 77Q, containing the polyQ extension, proved to be mature SDS-resistant amyloid fibrils which are retained in the membrane after SDS treatment. Curiously, at higher molar ratios of Atx-3 77Q:NB01 there is an apparent modulation of Atx-3 77Q amyloid fibrils maturation by the NB01. At a molar ratio of

1:10, the mature fibrils cannot be detected, which indicates that the NB01 affected and or significantly delayed their self-assembly.

Figure 39A and 39B exhibit the recognition of Atx-3 D1 and Atx-3 13Q by the Anti-OC antibody in both control samples and samples with different ratios of NB01. At the endpoint of Atx-3 D1 aggregation amyloid fibrils/protofibrils are present, which appears to be slightly reduced in the presence of NB01, especially at higher molar ratios (1:10). The recognition by the antibodies Anti-A11 and Anti-OC to Atx-3 13Q and Atx-3 77Q with NBs incubation appears to be identical with and without NB01. The immunoblot assay for Atx-3 77Q was repeated with the Anti-A11 antibody (Figure 39C). Despite the background, it was possible to detect toxic oligomeric species in Atx-3 77Q alone and in the presence of NB01. Finally, a third antibody was also used (1H9) as a load control for the detection of Atx-3 and the amount of Atx-3 was similar in all samples.

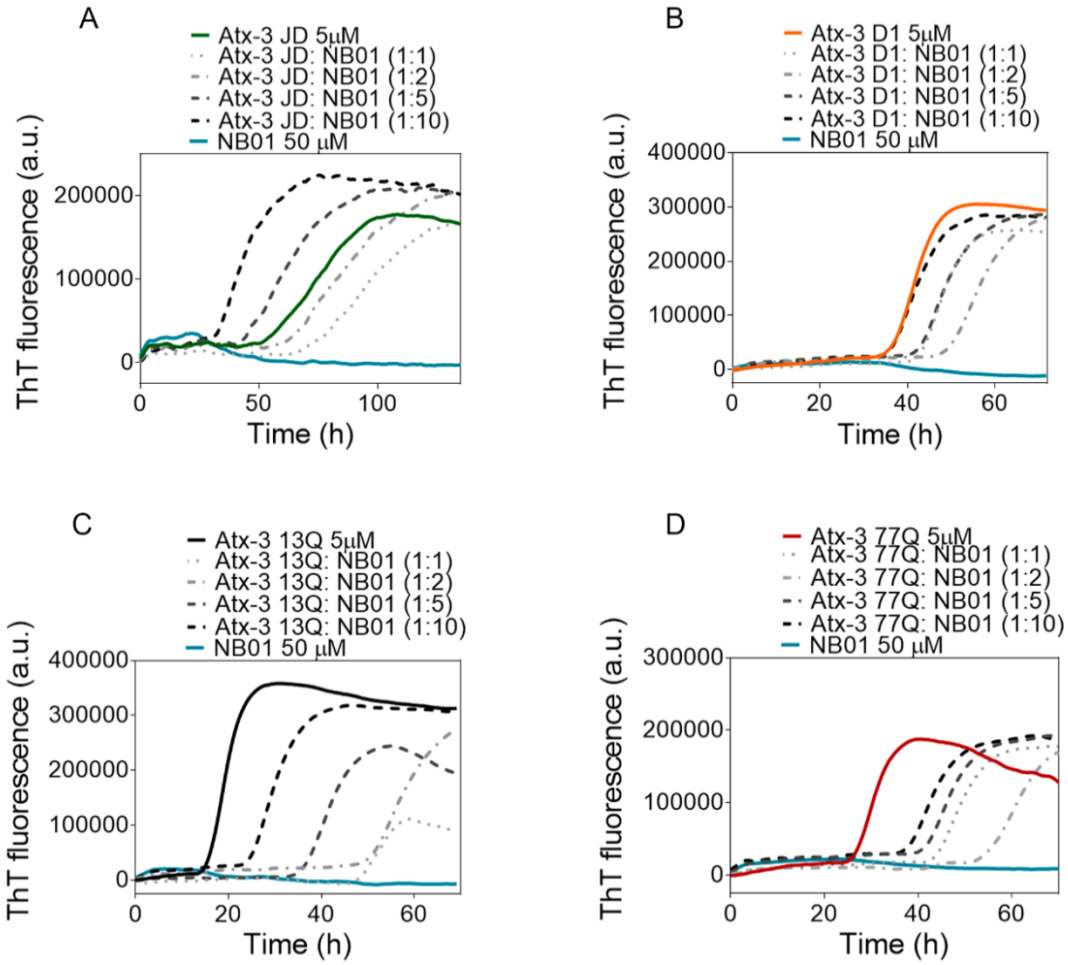

Figure 37: Modulation of 5 μM Atx-3 aggregation by NB01, visualized by a ThT assay. Each plot displays the results of the aggregation assay for each isoform incubated with different molar ratios of NB01, as well as the negative controls (Atx-3 variants alone). The legend corresponding to each sample is shown above the corresponding graphic. The plots presented were obtained by means of triplicates.

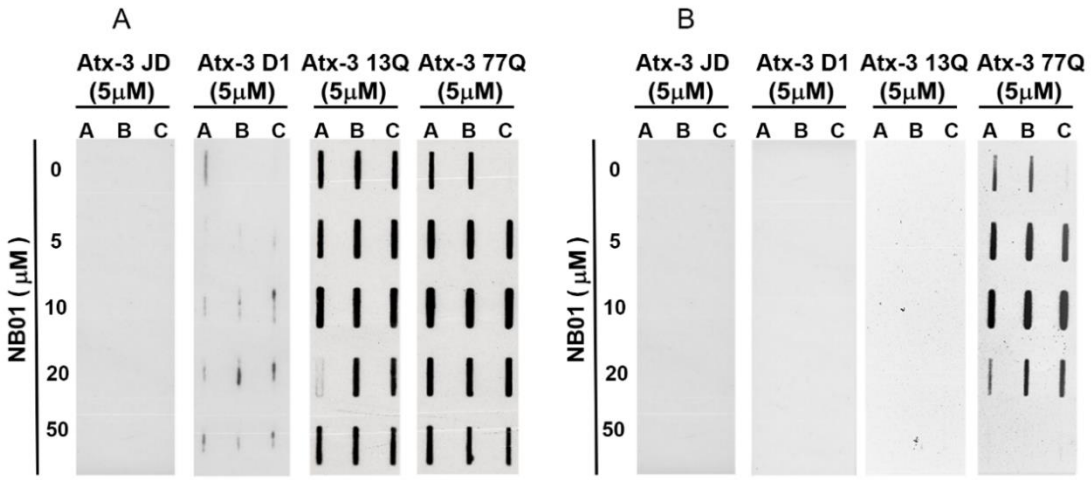

Figure 38: Filter Retardation Assay of endpoint samples from ThT aggregation assay of Atx-3 variants in the presence of NB01. A) Filter retardation Assay without SDS-treatment, Atx-3 JD shows soluble oligomers species, while Atx-3 D1, Atx-3 13Q and Atx-3 77Q show insoluble oligomers species, both without changes in the presence of NB01. B) Filter Retardation Assay with SDS treatment, Atx-3 JD, Atx-3 D1 and Atx-3 13Q show protofibrils/fibrils without any change with the presence of NB01 while the mature amyloid fibrils of Atx-3 77Q are affected by the NB01 presence. The samples are identified by 1H9 antibody binding.

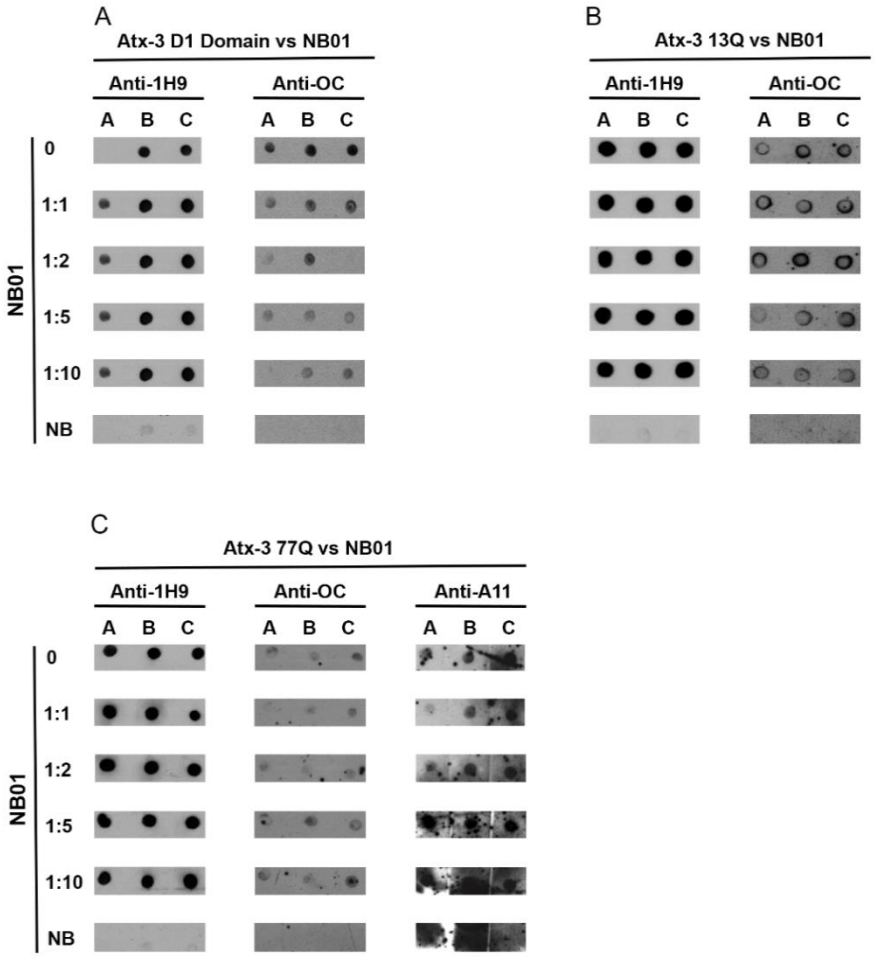

Figure 39: Dot-blot assay incubated with NB01. The endpoint samples of ThT assay were used in a Dot-blot assay. The membrane was incubated with different antibodies: Antibody 1H9 (that recognizes the total Atx-3 protein loaded), an anti-OC antibody (that recognizes fibrils/protofibrils) and an anti-A11 antibody (that recognizes toxic oligomers). A) Dot-blot of Atx-3 D1 with NB01 recognition by Anti-1H9 and Anti-OC. B) Dot-blot of Atx-3 13Q with NB01 recognition by Anti-1H9 and Anti-OC. C) Dot-blot of Atx-3 77Q with NB01 recognition by Anti-1H9, Anti-OC and Anti-A11. There are no major changes in the antibody recognition patterns.

Finally, to analyze the presence of fibers and possible changes in their morphology, TEM was performed using different ratios of NB01 and the three Atx-3 isoforms (see Figure 40). TEM images obtained for Atx-3 D1, with a scale of 100 nm, showed a decrease in the number of protofibrils upon addition of NB01, especially in the molar ratio 1:5, with no major changes in their morphology.

A different perception is obtained when visualizing Atx-3 13Q. It seems that the presence of NB01 also decreases the amount of protofibrils, but changes their morphology: the protofibrils seem to be longer and thicker.

Regarding Atx-3 77Q, TEM images of this isoform show the presence of mature elongated fibrils. When NB01 is added, these fibrils seem to be less frequent and shorter, and with a molar ratio of 1:10 it was not possible to visualize them at all. On the other hand, it is possible to see that the number of Atx-3 77Q protofibrils is increased by the incubation with NB01. So, it was once again possible to confirm that there is indeed an effect on the aggregation of Atx-3 caused by NB01.

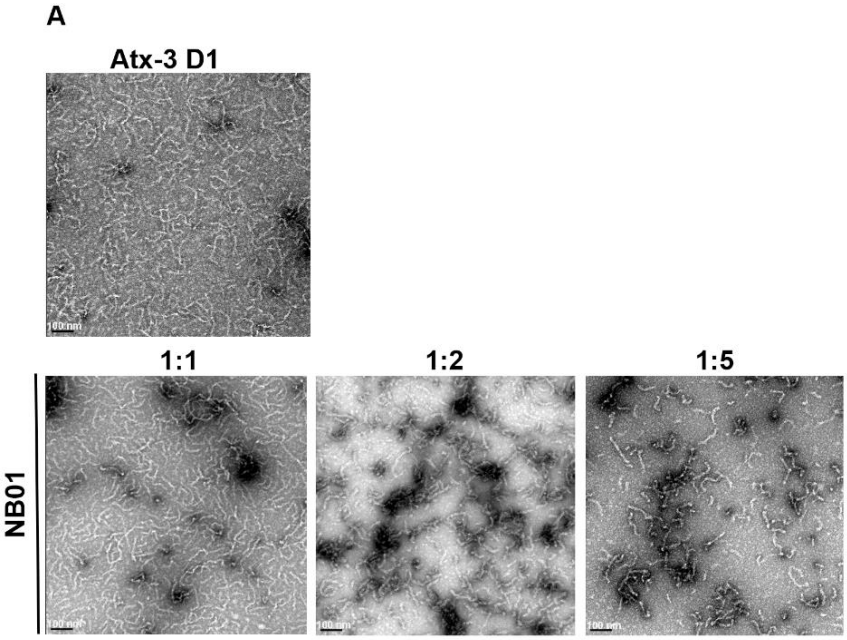

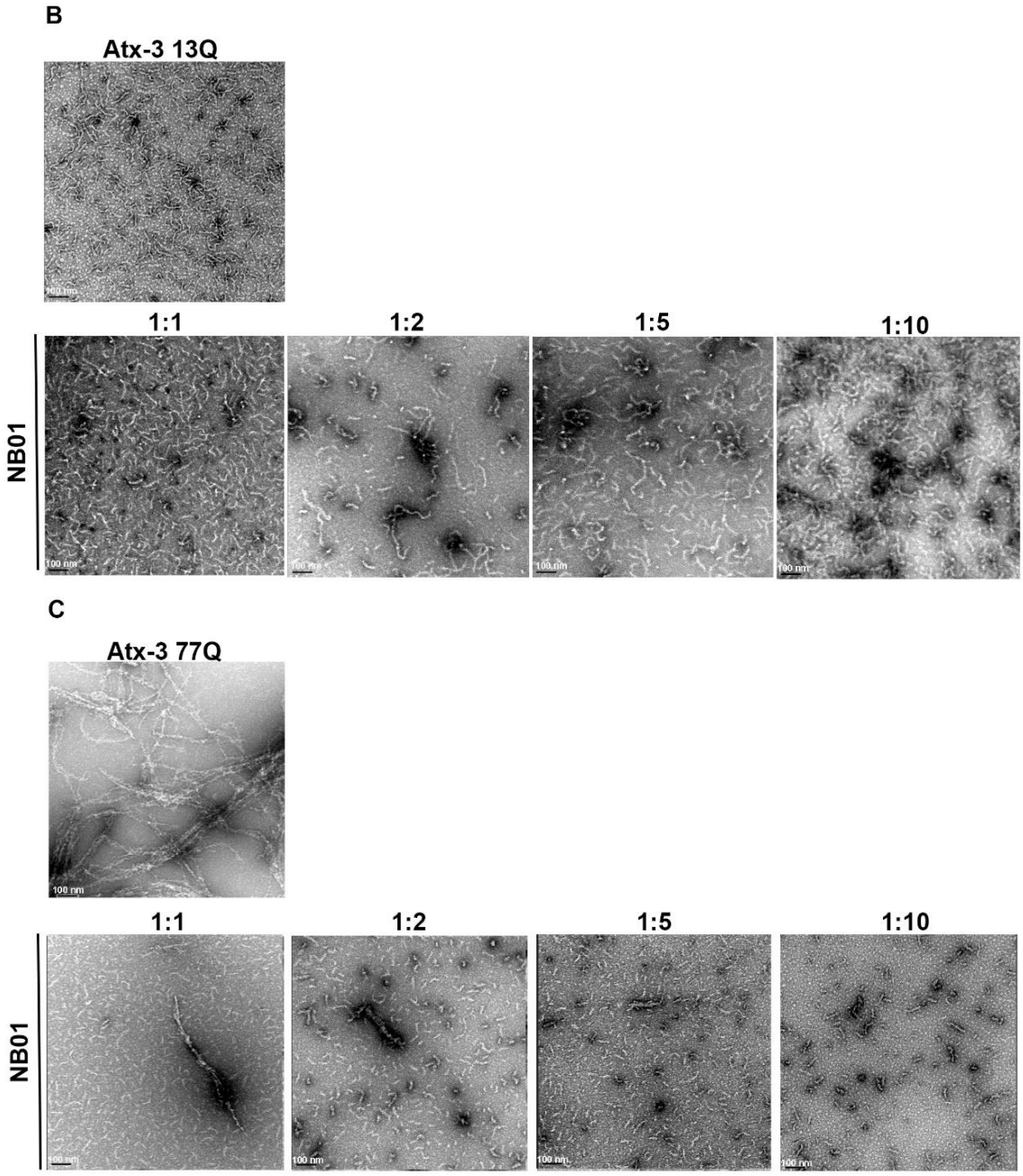

Figure 40: Transmission Electron microscopy images of Atx-3 with NB01. A) Atx-3 D1 domain with NB01 in a ratio of 1:1, 1:2, 1:5 and 1:10. Decrease in the protofibril number with no changes in the fibrils morphology. B) Atx-3 13Q with NB01 in a ratio of 1:1, 1:2, 1:5 and 1:10. Decrease in protofibril number and changes in their morphology. C) Atx-3 77Q with NB01 in a ratio of 1:1, 1:2, 1:5 and 1:10. Decrease in the number of mature fibrils and increase in amount of protofibril structures.

NB01 increased both Atx-3 13Q and Atx-3 77Q aggregation lag phase and decreased the number of mature Atx-3 77Q fibers Atx-3 13Q protofibrils. Yet, there is no apparent change in the toxic forms that are recognized by the Anti-A11 antibody. This prompted the study of soluble intermediary species that are formed during the aggregation process using a SEC time course assay. Two distinct time courses were executed: either Atx-3 13Q or Atx-3 77Q incubated with NB01 in a ratio of 1:2 (ratio that lead to a higher lag phase).

Time course of Atx-3 aggregation:

Size Exclusion Chromatography (Atx-3 13Q:NB01 complex)

This assay was used to monitor selectively the soluble species (that have a high contribute for Atx-3 toxicity) that are formed during the ThT assay, which showed the average behavior of the total species in solution. Atx-3 13Q aggregation kinetic analysis is displayed in Figure 41A, where the superimposed colored curves represent the chromatographic profiles of the protein samples collected from the aggregation assay at different time points.

In the beginning (0 hours) it is visible that Atx-3 13Q is mostly monomeric (starts in fraction 6) but over time a decrease in absorbance and a gradual shift from the monomeric peak to the high molecular weight (HMW) oligomeric species peak (fraction 4) occurs. Simultaneously, the total absorbance of the sample decreases, which can be explained by the increasing amount of insoluble aggregated protein retained in the eppendorf filter, a step systematically required before analyzing each sample collected along the aggregation process. At 19 h of incubation it's possible to detect a very small amount of Atx-3 13Q present in the intermediate fraction (Figure 41D, fractions 5) of the chromatogram. These species are in fact intermediate species formed along the aggregation process such as dimers and low molecular weight oligomers. After 72 hours, it is no longer possible to detect the presence of monomeric form or intermediate states of the Atx-3 13Q and all the protein is present in the HMW oligomeric species fraction.

Upon addition of NB01 (in a ratio of 1:2) the starting point (0 hours) consists on monomeric fractions just like the Atx-3 13Q control (Figure 41C). Along the aggregation process (Figure 41D) only a small part of the complex is converted to the HMW oligomeric species. At 72 hours, most of the Atx-3 13Q:NB01 complex is still monomeric (Figure 41E) while Atx-3 13Q alone is already predominantly found as HMW species. Progressively, the fraction corresponding to the HMW oligomeric species increases in comparison with the monomeric form (Figure 41G), but in the final time point of the aggregation assay (102 hours), low molecular weight species corresponding to the monomeric complex are still detected (Figure 41H), something the Atx-3 13Q alone does not display.

Contrary to Atx-3 13Q alone, the complex chromatographic profile (Figure 41G and 41H) exhibits a pronounced presence of intermediate oligomeric species (fraction 5). These intermediate species may be stabilized by the presence of NB01 or may occur in both experiments but are only detectable in the presence of the NB due to a delay of the process overall.

Thus, with this assay it was possible to confirm that the first steps of aggregation are in fact modulated by the presence of NB01, resulting in a deceleration of the aggregation process. Moreover, the experiment also demonstrates that NB01 remains bound to Atx-3 13Q throughout the process (no NB01 peak reappears). Still, it is mandatory to carry out a more detailed characterization of the aggregation species size distribution during both Atx-3 13Q and Atx-3 13Q:NB01 aggregation to guarantee that no additional species with a different molecular weight are formed along the process.

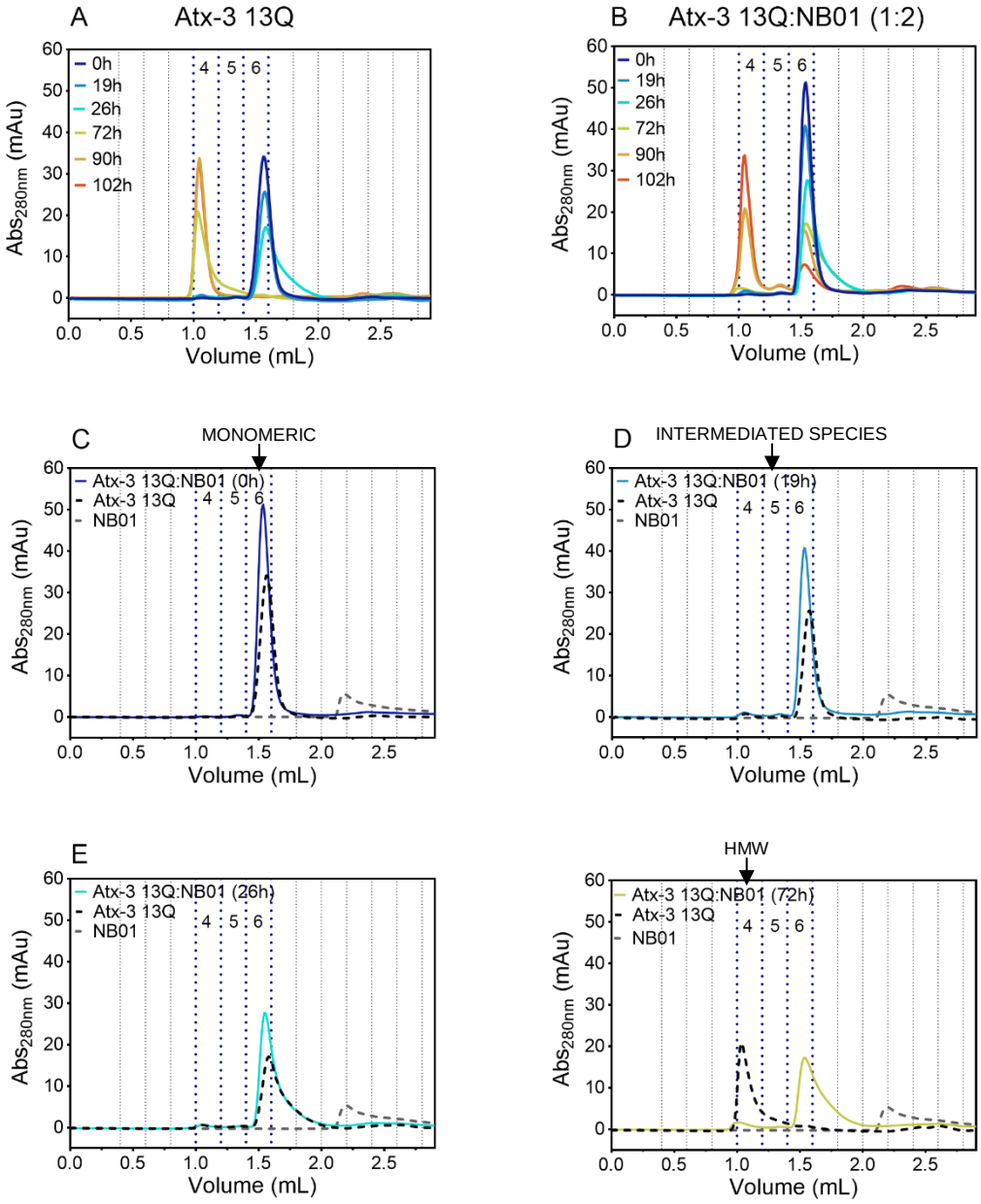

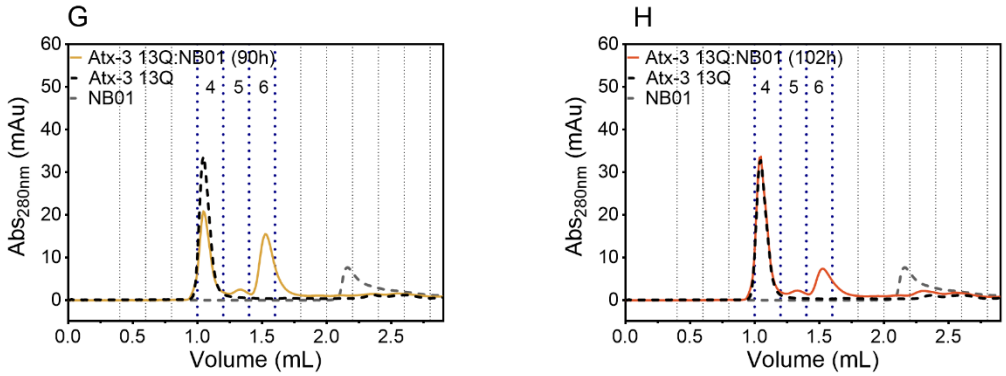

Figure 41: Modulation of the aggregation of Atx-3 13Q by NB01. SEC analysis at different time points (0, 19, 26, 72, 90 and 102 h) indicated by different colors. A) Atx-3 13Q control, B) Complex between Atx-3 13Q and NB01 in a molar ratio of 1:2. Comparison of the chromatographic profile of the species formed by Atx-3 13Q and the Atx-3:NB01 complex along the aggregation time-course: C) 0 h, D) 19 h, E) 26 h, F) 72h, G) 90h, H) 102h. The formation of HMW species is delayed by the presence of NB01.

Dynamic Light Scattering (DLS) (Atx-3 13Q:NB01)

A time-resolved Dynamic Light Scattering (DLS) assay using Atx-3 13Q as control and Atx-3 13Q:NB01 complex at a ratio of 1:2 was performed to determine the particle size distribution in solution through time (Figure 42). In Figure 42A, the aggregation of Atx-3 13Q control is shown in full circles and Atx-3 13Q:NB01 complex in empty circles. The aggregation process is measured by the increase of scattering intensity represented in normalized units (αD) along the time of aggregation. By the slope of both elongation curves of fibril formation it is possible to observe that the aggregation processes such as the fibril elongation, secondary nucleation and fragmentation are not affected. Once more, a remarkable inhibition of the formation of initial fibrils (primary nucleation) by NBs is demonstrated.

In the first moment of fibril formation of Atx-3 13Q, the intensity distribution (Figure 42B) shows the presence of small oligomers with hydrodynamic radius R_h < 10 nm. Some higher molecular weight species with a scattering intensity closer to R_h = 100 nm (primary fibers) are also present in the first hours of incubation (Figure 42B). These bigger species are present in a very low amount, since they were only detected by DLS (and not by SEC). These species work as a template for the well--defined peak centered at R_h = 15 nm (Figure 42D and 42F) that is formed during amyloid nucleation (secondary fibrils)[148].

A notorious similarity between Atx-3 13Q alone and Atx-3 13Q:NB01 complex is displayed since the shape of the size distribution hardly changes (Figure 42B vs 42C, 42D vs 42E and 42F vs 42G).

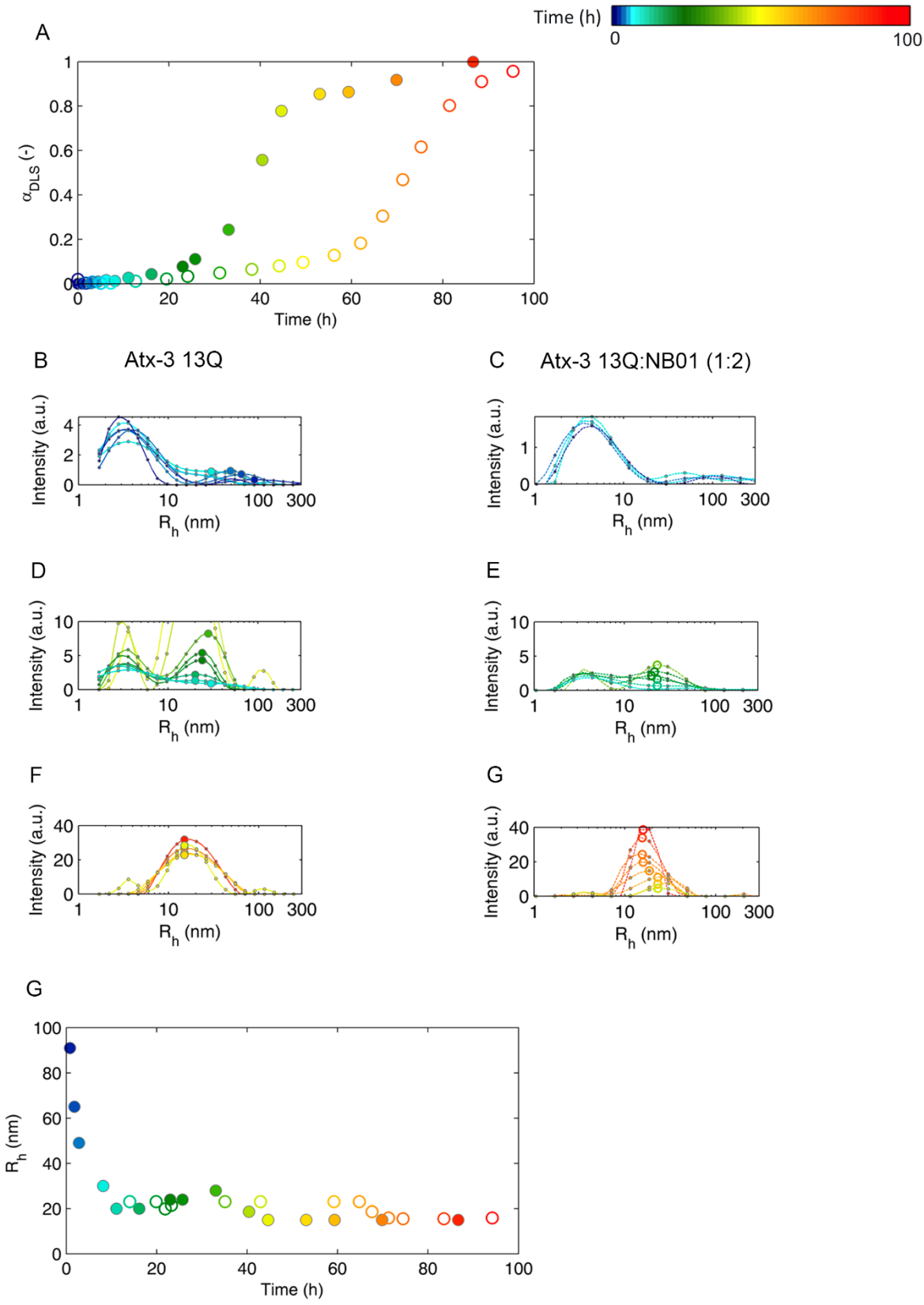

Figure 42: Time course analysis of the aggregation of Atx-3 13Q and Atx-13Q:NB01 complex (1:2) using DLS. A) Aggregation of Atx-3 13Q in full circles and complex in empty circles measured by the increase of light scattering intensity in normalized units α_{DLS} through time. B) D) F) Atx-3 13Q particle size distribution by DLS. C) D) F) Complex particle size distribution by DLS. G) Time evolution of Rh. The coloration of the circles demonstrates the assay time course and it the correspondence in hours is displayed in the top of the panel.

The hydrodynamic radius of the first moments of the complex aggregation was not detected due to low fibril concentration in the sample (Figure 42G). The initial HMW fibril species (100 nm) are prevented in the presence of the NB and the mean distribution of fiber size both with and without NB01 is about 15 nm. The species that are being formed during the aggregation process of Atx-3 13Q and Atx-3 13Q:NB01 (1:2) seem to present the same average distribution molecular weight. This indicates that the aggregation process occurs through the same mechanism in the presence of NB01.

As mentioned for NB05, additional studies using NB01 are essential to clarify the changes in the toxicity caused by this NB. It is also essential to study the effect of this nanobody in the expanded form of Atx-3.

Size Exclusion Chromatography (Atx-3 77Q:NB01 complex)

The assay was simultaneously performed for the Atx-3 77Q:NB05 and Atx-3 77Q:NB01 complex so both time courses were compared to the same Atx-3 77Q control previously presented. With the addition of NB01 (1:2) the monomeric fraction of the complex remains present for longer periods, being still identifiable 140 hours after the start of the aggregation process (Figure 43H). Regarding the intermediate oligomeric species, their presence is visible after 92 hours (Figure 43G, fraction 6) like the Atx-3 77Q control (Figure 43G). After 166h (Figure 43I) all of the complex is present in fraction 7 (with very low absorbance), corresponding to high molecular weight oligomers. The aggregation profile for complexes with NB01 is the same regardless of the Atx-3 isoform involved in complex formation. Fibril formation needs more time to start and takes more time to oligomerize.

Due to the expansion of the lag phase and a prolonged presence of soluble low molecular weight species more studies are needed to understand the toxicity resulting of the incubation of NBs such as *in vivo* studies to evaluate the therapeutic relevance of this molecular tool on Machado-Joseph disease and to guarantee that there is no heightened toxicity.

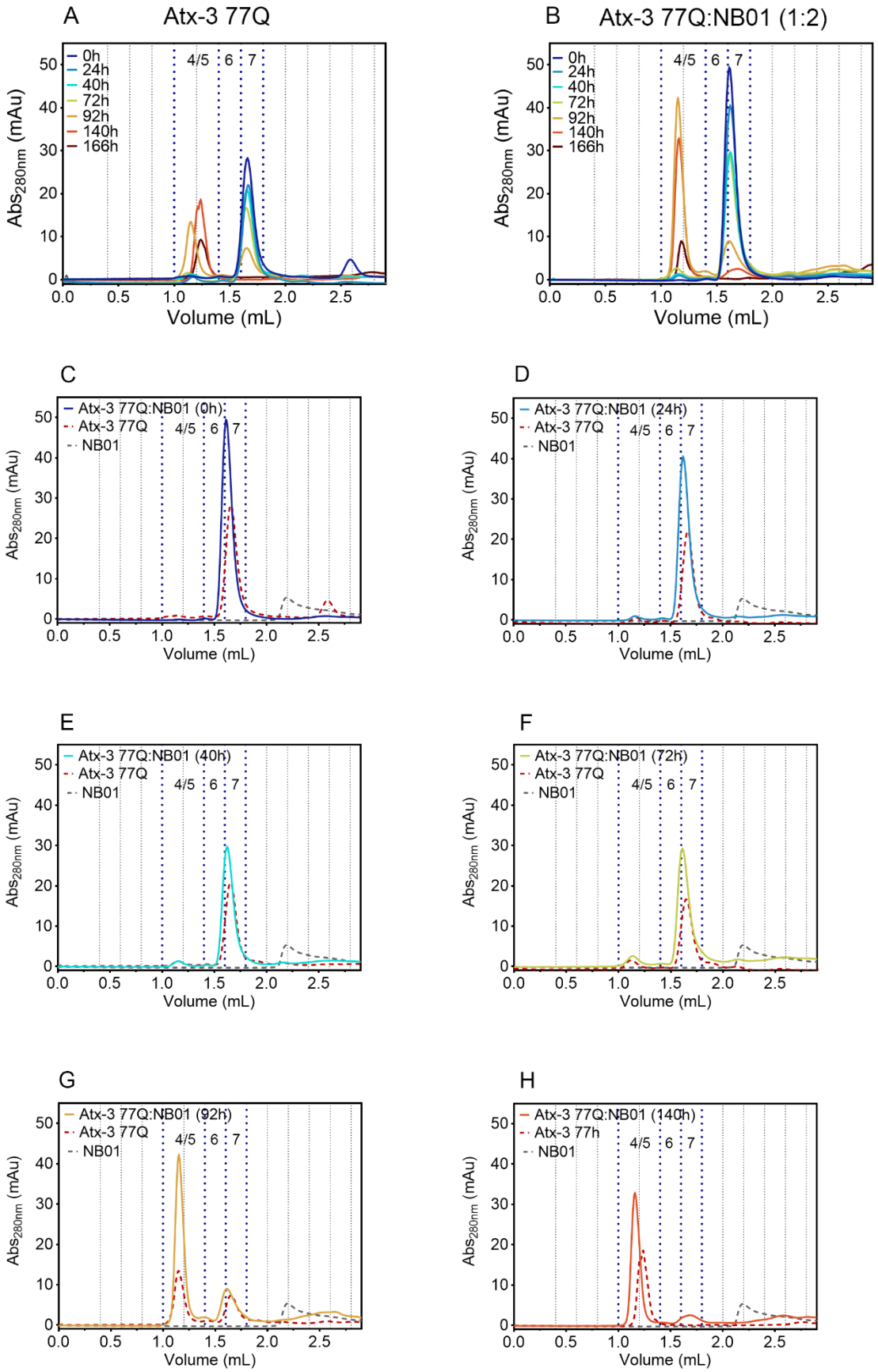
A
Atx-3 77Q
0h
24h
40h
72h
92h
140h
166h
4/5
6
7
Abs280nm (mAu)
Volume (mL)
B
Atx-3 77Q:NB01 (1:2)
C
Atx-3 77Q:NB01 (0h)
Atx-3 77Q
NB01
D
Atx-3 77Q:NB01 (24h)
E
Atx-3 77Q:NB01 (40h)
F
Atx-3 77Q:NB01 (72h)
G
Atx-3 77Q:NB01 (92h)
H
Atx-3 77Q:NB01 (140h)
Atx-3 77h

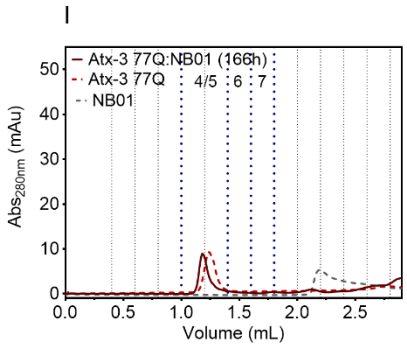

Figure 43: Modulation of the aggregation of 5µM Atx-3 77Q by incubation with NB01 (Atx-3:NB01 ration 1:2). SEC analysis at different time points (0, 24, 40, 72, 92, 140, 166) indicated by different colors. A) Atx-3 77Q control, B) Complex of Atx-3 77Q and NB01 (1:2). Aggregation comparison between Atx-3 77Q and the complex: C) 0 h, D) 24 h, E) 40 h, F) 72 h, G) 92 h, H) 140 h, I) 166 h. The aggregation is delayed by the presence of NB01.

In summary, all NBs studied so far increased the lag phase of Atx-3 and the elongation phase appears not to be altered. However, only the NBs that can bind to Atx-3 77Q can decrease the presence of mature fibers. Toxic species (that are recognized by Anti-A11) are still formed, but their detection is similar to the controls. NB01 presented a high increase in the aggregation lag phase of Atx-3 13Q and Atx-3 77Q and NB05 showed the ability to specifically delay Atx-3 77Q aggregation. Based on this information further studies were performed using these NBs. The soluble species formed when these NBs are present are identical to the control. Still, these results prompt new questions about the toxicity of the NBs and their applicability in the Atx-3 aggregation modulation.

Conclusions

The main goal of this work was to explore the potential of NBs produced against the Atx-3 JD in modulating the aggregation process of Atx-3 and subsequent applicability in the therapy of Machado-Joseph Disease. An additional objective was to use these NBs as crystallization chaperones to aid the crystallization and structure determination of Atx-3.

The optimal conditions of expression and purification of NBs were determined and resulted in the production of high amounts of pure protein for 17 of the 18 NB variants under study, except for NB10, which remained insoluble.

After the production of the 17 NBs a selection of the most promising was done via a pull-down assay. This technique provided some promising hits, such as NB01 and NB02. The incubation of each NB with different constructs of Atx-3 followed by purification of the binary complexes by SEC confirmed the interaction of NB01 and NB02 with Atx-3 and revealed another possible Atx-3 interactor, NB05, which was not detected by the pull-down assay. The inability to detect this interaction in the pull-down assay could be explained by a competitive binding of NB05 and of antibody anti-Atx-3 1H9 to an overlapping Atx-3 interaction surface. Interestingly, although the NBs were produced against JD, no interaction between the isolated Atx-3 JD and the NBs (01, 02 and 05) was detected.

Biochemical characterization of the interaction between the three NBs and the different Atx-3 isoforms and truncated constructs resulted in the determination of the affinity constants, which were in the nanomolar range for the interaction between the three Atx-3 interacting NBs and the Atx-3 variants. In accordance with the pull-down and the SEC assay, no interaction was detected between the NBs and the isolated Atx-3 JD by ITC under the conditions tested. The NB that exhibited the highest affinity to Atx-3 variants was NB01 with K_D = 49.4 $\pm$ 6.7 nM for Atx-3 D1, K_D =212 $\pm$ 9 nM for Atx-3 13Q and K_D = 333 $\pm$ 49 nM for Atx-3 77Q. NB02 and NB05 showed similar affinity constants (428-911 nM) while no interaction was detected using NB03. Also, the molar ratio varied between 1:1 and 1:2 (Atx-3:NB).

Regarding NB01, there seems to exist a correlation between the size of Atx-3 (and the PolyQ tract) and the affinity of interaction. The presence of further Atx-3 domains and the expansion of the polyQ stretch may increase the protein flexibility decreasing the affinity for NB01. The absence of interaction with Atx-3 JD may be justified by the low affinity or transient nature of this interaction or even by the low abundance of a specific Atx-3 conformer to which NB exclusively binds in the

conditions tested. This suggests that these NBs may only recognize specific conformations of Atx-3 JD that are mainly present in Atx-3 D1, Atx-3 13Q and Atx-3 77Q, triggered by the dynamic behavior of the structurally disordered C-terminal tail. For all three NBs (NB01, 02 and 05) complex formation is governed by enthalpic-driven interactions such as hydrogen bonds or polar contacts, suggesting that no major structural changes are occurring.

DLS results combined with SAXS analysis showed that, although Atx-3 protein naturally displays an elongated structure, the presence of NB01 confers the complex a more compact globular shape. The use of Small Angle X-ray Scattering added an important layer of information: the reconstruction of the shape of the complex displays 2 NB01 bound to 1 Atx-3 13Q molecule. This technique also confirmed the hypothesis that no major structural changes occur: The globular shape of the complex does not derive from conformational changes in either protein but from the enveloping effect of the two NBs. Still, it is not clear whether both NB01 molecules are in fact bound to Atx-3 or if only one is directly interacting. Additionally, this method does not allow to precisely map the Atx-3 interaction site.

The ability of the NBs to stabilize Atx-3 and induce a more compact structure was a good hint of their crystallization chaperone properties. While preliminary crystallization conditions were obtained for co-crystallization of Atx-3 D1 with NB01, no optimal condition was found. Further optimization of the crystallization conditions is required.

The DLS assay gave the first indication that these NBs (NB01 more precisely) may be in fact good modulators of Atx-3 aggregation by decreasing of Atx-3 polydispersity. This finding was then supported by the incubation of Atx-3 constructs with three of the NBs (NB01, NB02 and NB05) which resulted in a prolonged lag phase of Atx-3 aggregation. This delayed aggregation was not accompanied by alterations in the profile of the amyloid progress curves, indicating that the elongation process is not affected by the presence of these interactors. NB03 did not present any interaction with Atx-3 isoforms during biochemical assays but also delayed Atx-3 aggregation probably due to an unspecific molecular crowding effect.

Considering NB01 specifically, this NB extended the amyloid aggregation lag phase of both normal and expanded Atx-3 and decreased the formation of mature amyloid mature fibrils of the pathogenic Atx-3, without affecting the formation of intermediate species. The oligomeric species that are formed during the lag phase present the same size both with and without the addition of NB01. In turn, studies using NB05 present an impressive retardation of Atx-3 77Q aggregation and a moderate

delay of non-pathogenic (Atx-3 13Q) aggregation. The increase in the lag phase by NB05 did not affect the presence of low molecular weight intermediated species. Combining this information, it becomes clear that the main effect of the tested NBs on Atx-3 is the delay of the aggregation process, probably by shielding the previously mentioned aggregation--prone regions (although the exact region of interaction could not yet be determined).

Nowadays, the soluble low molecular weight toxic oligomeric species formed during the aggregation process of Atx-3 are pointed as the main intermediate species causing the neurodegeneration associated with distinct amyloid diseases, such as MJD, Parkinson's and Alzheimer's. The interaction of the NBs with Atx-3 leads to a delay in the aggregation but does not prevent the presence of toxic oligomeric species in the endpoint. The toxicity of the soluble intermediates formed in the presence of NBs may be different than the species formed with Atx-3 alone. Since we intend to explore the potential of NBs in modulating the neurodegeneration resulting from this process, additional *in vivo* studies using an already established MJD neuronal model are required to make sure that the beneficial effect of the NBs in the lag phase is not cancelled by an increase in overall toxicity.

Overall, this study provides valuable insights on the biochemical and biophysical characterization of the interaction between NBs and Atx-3, clarifying the thermodynamics of the binding and absence of structural changes induced by the complex formation. Additionally, *in vitro* experiments revealed that binding of NBs to or near the Josephin Domain of Atx-3 results in the delay of the start of the aggregation process. As such, this work may be the basis for promising exploration of NBs as biopharmaceutical tools in the prevention of Machado-Joseph Disease.

Future Perspectives

Future perspectives for this work comprise the following topics: to complete the characterization of the interaction between the two best NBs (NB01 and NB05) and Atx-3 as well as studying the toxicity of the soluble intermediate species that are formed during the aggregation process in both non-expanded and expanded Atx-3:NB complexes using cell culture techniques.

It is also essential to demonstrate the ability of these NBs to delay the aggregation in a selective and directed manner by mapping the binding site residues of the complex. Site-directed mutagenesis studies of the Atx-3 binding site residues may

be used to test if the interaction is crucial to the NB effect. Additionally, knowing the binding sequence of the NBs we could design even smaller peptides as good interactors, with better pharmaceutical properties.

At last, more efforts need to be done in the crystallography studies of the Atx-3:NB complex. The determination of its atomic structure would be an important step in the endeavor of fully understanding the molecular properties of Atx-3 and in the discovery of new pharmacological approaches.

References

1 Dobson, C. M. Protein folding and misfolding. *Nature* **426**, 884-890, doi:10.1038/nature02261 (2003).
2 Vendruscolo, M. & Dobson, C. M. Towards complete descriptions of the free-energy landscapes of proteins. *Philos Trans A Math Phys Eng Sci* **363**, 433-450; discussion 450-432, doi:10.1098/rsta.2004.1501 (2005).
3 Wolynes, P. G. Energy landscapes and solved protein-folding problems. *Philos Trans A Math Phys Eng Sci* **363**, 453-464; discussion 464-457, doi:10.1098/rsta.2004.1502 (2005).
4 Jahn, T. R. & Radford, S. E. The Yin and Yang of protein folding. *FEBS J* **272**, 5962-5970, doi:10.1111/j.1742-4658.2005.05021.x (2005).
5 Fersht, A. R. Transition-state structure as a unifying basis in protein-folding mechanisms: contact order, chain topology, stability, and the extended nucleus mechanism. *Proc Natl Acad Sci U S A* **97**, 1525-1529 (2000).
6 Daggett, V. & Fersht, A. R. Is there a unifying mechanism for protein folding? *Trends Biochem Sci* **28**, 18-25 (2003).
7 Vendruscolo, M., Paci, E., Karplus, M. & Dobson, C. M. Structures and relative free energies of partially folded states of proteins. *Proc Natl Acad Sci U S A* **100**, 14817-14821, doi:10.1073/pnas.2036516100 (2003).
8 Chiti, F. & Dobson, C. M. Protein Misfolding, Amyloid Formation, and Human Disease: A Summary of Progress Over the Last Decade. *Annu Rev Biochem* **86**, 27-68, doi:10.1146/annurev-biochem-061516-045115 (2017).
9 Dobson, J. *et al.* Inducing protein aggregation by extensional flow. *Proc Natl Acad Sci U S A* **114**, 4673-4678, doi:10.1073/pnas.1702724114 (2017).
10 Chen, S., Berthelier, V., Hamilton, J. B., O'Nuallain, B. & Wetzel, R. Amyloid-like features of polyglutamine aggregates and their assembly kinetics. *Biochemistry* **41**, 7391-7399 (2002).
11 Margulis, B. A., Vigont, V., Lazarev, V. F., Kaznacheyeva, E. V. & Guzhova, I. V. Pharmacological protein targets in polyglutamine diseases: mutant polypeptides and their interactors. *FEBS Lett* **587**, 1997-2007, doi:10.1016/j.febslet.2013.05.022 (2013).
12 Orr, H. T. *et al.* Expansion of an unstable trinucleotide CAG repeat in spinocerebellar ataxia type 1. *Nat Genet* **4**, 221-226, doi:10.1038/ng0793-221 (1993).
13 Nechiporuk, A. *et al.* Genetic mapping of the spinocerebellar ataxia type 2 gene on human chromosome 12. *Neurology* **46**, 1731-1735 (1996).
14 Kawaguchi, Y. *et al.* CAG expansions in a novel gene for Machado-Joseph disease at chromosome 14q32.1. *Nat Genet* **8**, 221-228, doi:10.1038/ng1194-221 (1994).
15 Zhuchenko, O. *et al.* Autosomal dominant cerebellar ataxia (SCA6) associated with small polyglutamine expansions in the alpha 1A-voltage-dependent calcium channel. *Nat Genet* **15**, 62-69, doi:10.1038/ng0197-62 (1997).
16 David, G. *et al.* Molecular and clinical correlations in autosomal dominant cerebellar ataxia with progressive macular dystrophy (SCA7). *Hum Mol Genet* **7**, 165-170 (1998).
17 Nakamura, K. *et al.* SCA17, a novel autosomal dominant cerebellar ataxia caused by an expanded polyglutamine in TATA-binding protein. *Hum Mol Genet* **10**, 1441-1448 (2001).
18 Koide, R. *et al.* Unstable expansion of CAG repeat in hereditary dentatorubral-pallidoluysian atrophy (DRPLA). *Nat Genet* **6**, 9-13, doi:10.1038/ng0194-9 (1994).
19 Nagafuchi, S. *et al.* Dentatorubral and pallidoluysian atrophy expansion of an unstable CAG trinucleotide on chromosome 12p. *Nat Genet* **6**, 14-18, doi:10.1038/ng0194-14 (1994).
20 La Spada, A. R., Wilson, E. M., Lubahn, D. B., Harding, A. E. & Fischbeck, K. H. Androgen receptor gene mutations in X-linked spinal and bulbar muscular atrophy. *Nature* **352**, 77-79, doi:10.1038/352077a0 (1991).
21 Zoghbi, H. Y. & Orr, H. T. Glutamine repeats and neurodegeneration. *Annu Rev Neurosci* **23**, 217-247, doi:10.1146/annurev.neuro.23.1.217 (2000).
22 Gatchel, J. R. & Zoghbi, H. Y. Diseases of unstable repeat expansion: mechanisms and common principles. *Nat Rev Genet* **6**, 743-755, doi:10.1038/nrg1691 (2005).

23 Kieling, C., Prestes, P. R., Saraiva-Pereira, M. L. & Jardim, L. B. Survival estimates for patients with Machado-Joseph disease (SCA3). *Clin Genet* **72**, 543-545, doi:10.1111/j.1399-0004.2007.00910.x (2007).
24 Bevivino, A. E. & Loll, P. J. An expanded glutamine repeat destabilizes native ataxin-3 structure and mediates formation of parallel beta -fibrils. *Proc Natl Acad Sci U S A* **98**, 11955-11960, doi:10.1073/pnas.211305198 (2001).
25 Huang, C. C. *et al.* Amyloid formation by mutant huntingtin: threshold, progressivity and recruitment of normal polyglutamine proteins. *Somat Cell Mol Genet* **24**, 217-233 (1998).
26 Poirier, M. A. *et al.* Huntingtin spheroids and protofibrils as precursors in polyglutamine fibrilization. *J Biol Chem* **277**, 41032-41037, doi:10.1074/jbc.M205809200 (2002).
27 Scherzinger, E. *et al.* Huntingtin-encoded polyglutamine expansions form amyloid-like protein aggregates in vitro and in vivo. *Cell* **90**, 549-558 (1997).
28 Treusch, S., Cyr, D. M. & Lindquist, S. Amyloid deposits: protection against toxic protein species? *Cell Cycle* **8**, 1668-1674, doi:10.4161/cc.8.11.8503 (2009).
29 Almeida, B., Fernandes, S., Abreu, I. A. & Macedo-Ribeiro, S. Trinucleotide repeats: a structural perspective. *Front Neurol* **4**, 76, doi:10.3389/fneur.2013.00076 (2013).
30 Coutinho, P. & Andrade, C. Autosomal dominant system degeneration in Portuguese families of the Azores Islands. A new genetic disorder involving cerebellar, pyramidal, extrapyramidal and spinal cord motor functions. *Neurology* **28**, 703-709 (1978).
31 Rosenberg, R. N. Machado-Joseph disease: an autosomal dominant motor system degeneration. *Mov Disord* **7**, 193-203, doi:10.1002/mds.870070302 (1992).
32 Sudarsky, L. & Coutinho, P. Machado-Joseph disease. *Clin Neurosci* **3**, 17-22 (1995).
33 Ranum, L. P. *et al.* Spinocerebellar ataxia type 1 and Machado-Joseph disease: incidence of CAG expansions among adult-onset ataxia patients from 311 families with dominant, recessive, or sporadic ataxia. *Am J Hum Genet* **57**, 603-608 (1995).
34 Riess, O., Rub, U., Pastore, A., Bauer, P. & Schols, L. SCA3: neurological features, pathogenesis and animal models. *Cerebellum* **7**, 125-137, doi:10.1007/s12311-008-0013-4 (2008).
35 Schols, L., Bauer, P., Schmidt, T., Schulte, T. & Riess, O. Autosomal dominant cerebellar ataxias: clinical features, genetics, and pathogenesis. *Lancet Neurol* **3**, 291-304, doi:10.1016/S1474-4422(04)00737-9 (2004).
36 Alves, S. *et al.* Striatal and nigral pathology in a lentiviral rat model of Machado-Joseph disease. *Hum Mol Genet* **17**, 2071-2083, doi:10.1093/hmg/ddn106 (2008).
37 Durr, A. *et al.* Spinocerebellar ataxia 3 and Machado-Joseph disease: clinical, molecular, and neuropathological features. *Ann Neurol* **39**, 490-499, doi:10.1002/ana.410390411 (1996).
38 Klockgether, T. *et al.* Autosomal dominant cerebellar ataxia type I. MRI-based volumetry of posterior fossa structures and basal ganglia in spinocerebellar ataxia types 1, 2 and 3. *Brain* **121 (Pt 9)**, 1687-1693 (1998).
39 Rub, U., Brunt, E. R. & Deller, T. New insights into the pathoanatomy of spinocerebellar ataxia type 3 (Machado-Joseph disease). *Curr Opin Neurol* **21**, 111-116, doi:10.1097/WCO.0b013e3282f7673d (2008).
40 D'Abreu, A., Franca, M. C., Jr., Paulson, H. L. & Lopes-Cendes, I. Caring for Machado-Joseph disease: current understanding and how to help patients. *Parkinsonism Relat Disord* **16**, 2-7, doi:10.1016/j.parkreldis.2009.08.012 (2010).
41 Lima, L. & Coutinho, P. Clinical criteria for diagnosis of Machado-Joseph disease: report of a non-Azorena Portuguese family. *Neurology* **30**, 319-322 (1980).
42 Padiath, Q. S., Srivastava, A. K., Roy, S., Jain, S. & Brahmachari, S. K. Identification of a novel 45 repeat unstable allele associated with a disease phenotype at the MJD1/SCA3 locus. *Am J Med Genet B Neuropsychiatr Genet* **133B**, 124-126, doi:10.1002/ajmg.b.30088 (2005).
43 Maciel, P. *et al.* Improvement in the molecular diagnosis of Machado-Joseph disease. *Arch Neurol* **58**, 1821-1827 (2001).
44 van Alfen, N. *et al.* Intermediate CAG repeat lengths (53,54) for MJD/SCA3 are associated with an abnormal phenotype. *Ann Neurol* **49**, 805-807 (2001).
45 Matos, C. A., de Macedo-Ribeiro, S. & Carvalho, A. L. Polyglutamine diseases: the special case of ataxin-3 and Machado-Joseph disease. *Prog Neurobiol* **95**, 26-48, doi:10.1016/j.pneurobio.2011.06.007 (2011).

46 Masino, L. *et al.* Domain architecture of the polyglutamine protein ataxin-3: a globular domain followed by a flexible tail. *FEBS Lett* **549**, 21-25 (2003).
47 Nicastro, G. *et al.* Josephin domain of ataxin-3 contains two distinct ubiquitin-binding sites. *Biopolymers* **91**, 1203-1214, doi:10.1002/bip.21210 (2009).
48 Goto, J. *et al.* Machado-Joseph disease gene products carrying different carboxyl termini. *Neurosci Res* **28**, 373-377 (1997).
49 Harris, G. M., Dodelzon, K., Gong, L., Gonzalez-Alegre, P. & Paulson, H. L. Splice isoforms of the polyglutamine disease protein ataxin-3 exhibit similar enzymatic yet different aggregation properties. *PLoS One* **5**, e13695, doi:10.1371/journal.pone.0013695 (2010).
50 Macedo-Ribeiro, S., Cortes, L., Maciel, P. & Carvalho, A. L. Nucleocytoplasmic shuttling activity of ataxin-3. *PLoS One* **4**, e5834, doi:10.1371/journal.pone.0005834 (2009).
51 Chow, M. K., Mackay, J. P., Whisstock, J. C., Scanlon, M. J. & Bottomley, S. P. Structural and functional analysis of the Josephin domain of the polyglutamine protein ataxin-3. *Biochem Biophys Res Commun* **322**, 387-394, doi:10.1016/j.bbrc.2004.07.131 (2004).
52 Burnett, B., Li, F. & Pittman, R. N. The polyglutamine neurodegenerative protein ataxin-3 binds polyubiquitylated proteins and has ubiquitin protease activity. *Hum Mol Genet* **12**, 3195-3205, doi:10.1093/hmg/ddg344 (2003).
53 Mao, Y. *et al.* Deubiquitinating function of ataxin-3: insights from the solution structure of the Josephin domain. *Proc Natl Acad Sci U S A* **102**, 12700-12705, doi:10.1073/pnas.0506344102 (2005).
54 Nicastro, G. *et al.* The solution structure of the Josephin domain of ataxin-3: structural determinants for molecular recognition. *Proc Natl Acad Sci U S A* **102**, 10493-10498, doi:10.1073/pnas.0501732102 (2005).
55 Song, A. X. *et al.* Structural transformation of the tandem ubiquitin-interacting motifs in ataxin-3 and their cooperative interactions with ubiquitin chains. *PLoS One* **5**, e13202, doi:10.1371/journal.pone.0013202 (2010).
56 Zhemkov, V. A., Kulminskaya, A. A., Bezprozvanny, I. B. & Kim, M. The 2.2-Angstrom resolution crystal structure of the carboxy-terminal region of ataxin-3. *FEBS Open Bio* **6**, 168-178, doi:10.1002/2211-5463.12029 (2016).
57 Lupton, C. J. *et al.* Enhanced molecular mobility of ordinarily structured regions drives polyglutamine disease. *J Biol Chem* **290**, 24190-24200, doi:10.1074/jbc.M115.659532 (2015).
58 Scarff, C. A. *et al.* Examination of Ataxin-3 (atx-3) Aggregation by Structural Mass Spectrometry Techniques: A Rationale for Expedited Aggregation upon Polyglutamine (polyQ) Expansion. *Mol Cell Proteomics* **14**, 1241-1253, doi:10.1074/mcp.M114.044610 (2015).
59 McGowan, D. P. *et al.* Amyloid-like inclusions in Huntington's disease. *Neuroscience* **100**, 677-680 (2000).
60 Gales, L. *et al.* Towards a structural understanding of the fibrillization pathway in Machado-Joseph's disease: trapping early oligomers of non-expanded ataxin-3. *J Mol Biol* **353**, 642-654, doi:10.1016/j.jmb.2005.08.061 (2005).
61 Masino, L. *et al.* Characterization of the structure and the amyloidogenic properties of the Josephin domain of the polyglutamine-containing protein ataxin-3. *J Mol Biol* **344**, 1021-1035, doi:10.1016/j.jmb.2004.09.065 (2004).
62 Masino, L. *et al.* The Josephin domain determines the morphological and mechanical properties of ataxin-3 fibrils. *Biophys J* **100**, 2033-2042, doi:10.1016/j.bpj.2011.02.056 (2011).
63 Ahmed, A. B., Znassi, N., Chateau, M. T. & Kajava, A. V. A structure-based approach to predict predisposition to amyloidosis. *Alzheimers Dement* **11**, 681-690, doi:10.1016/j.jalz.2014.06.007 (2015).
64 Chiti, F., Stefani, M., Taddei, N., Ramponi, G. & Dobson, C. M. Rationalization of the effects of mutations on peptide and protein aggregation rates. *Nature* **424**, 805-808, doi:10.1038/nature01891 (2003).
65 Fernandez-Escamilla, A. M., Rousseau, F., Schymkowitz, J. & Serrano, L. Prediction of sequence-dependent and mutational effects on the aggregation of peptides and proteins. *Nat Biotechnol* **22**, 1302-1306, doi:10.1038/nbt1012 (2004).

66 Garbuzynskiy, S. O., Lobanov, M. Y. & Galzitskaya, O. V. FoldAmyloid: a method of prediction of amyloidogenic regions from protein sequence. *Bioinformatics* **26**, 326-332, doi:10.1093/bioinformatics/btp691 (2010).
67 Linding, R., Schymkowitz, J., Rousseau, F., Diella, F. & Serrano, L. A comparative study of the relationship between protein structure and beta-aggregation in globular and intrinsically disordered proteins. *J Mol Biol* **342**, 345-353, doi:10.1016/j.jmb.2004.06.088 (2004).
68 Pallares, I. & Ventura, S. Advances in the prediction of protein aggregation propensity. *Curr Med Chem*, doi:10.2174/0929867324666170705121754 (2017).
69 Roche, D. B., Villain, E. & Kajava, A. V. Usage of a dataset of NMR resolved protein structures to test aggregation versus solubility prediction algorithms. *Protein Sci* **26**, 1864-1869, doi:10.1002/pro.3225 (2017).
70 Rousseau, F., Schymkowitz, J. & Serrano, L. Protein aggregation and amyloidosis: confusion of the kinds? *Curr Opin Struct Biol* **16**, 118-126, doi:10.1016/j.sbi.2006.01.011 (2006).
71 Tartaglia, G. G., Cavalli, A. & Vendruscolo, M. Prediction of local structural stabilities of proteins from their amino acid sequences. *Structure* **15**, 139-143, doi:10.1016/j.str.2006.12.007 (2007).
72 Tartaglia, G. G., Cavalli, A., Pellarin, R. & Caflisch, A. Prediction of aggregation rate and aggregation-prone segments in polypeptide sequences. *Protein Sci* **14**, 2723-2734, doi:10.1110/ps.051471205 (2005).
73 Thompson, M. J. *et al.* The 3D profile method for identifying fibril-forming segments of proteins. *Proc Natl Acad Sci U S A* **103**, 4074-4078, doi:10.1073/pnas.0511295103 (2006).
74 Walsh, I., Seno, F., Tosatto, S. C. & Trovato, A. PASTA 2.0: an improved server for protein aggregation prediction. *Nucleic Acids Res* **42**, W301-307, doi:10.1093/nar/gku399 (2014).
75 Zambrano, R. *et al.* AGGRESCAN3D (A3D): server for prediction of aggregation properties of protein structures. *Nucleic Acids Res* **43**, W306-313, doi:10.1093/nar/gkv359 (2015).
76 Ellisdon, A. M., Thomas, B. & Bottomley, S. P. The two-stage pathway of ataxin-3 fibrillogenesis involves a polyglutamine-independent step. *J Biol Chem* **281**, 16888-16896, doi:10.1074/jbc.M601470200 (2006).
77 Natalello, A. *et al.* A major role for side-chain polyglutamine hydrogen bonding in irreversible ataxin-3 aggregation. *PLoS One* **6**, e18789, doi:10.1371/journal.pone.0018789 (2011).
78 Invernizzi, G., Lambrughi, M., Regonesi, M. E., Tortora, P. & Papaleo, E. The conformational ensemble of the disordered and aggregation-protective 182-291 region of ataxin-3. *Biochim Biophys Acta* **1830**, 5236-5247, doi:10.1016/j.bbagen.2013.07.007 (2013).
79 de Chiara, C., Menon, R. P., Dal Piaz, F., Calder, L. & Pastore, A. Polyglutamine is not all: the functional role of the AXH domain in the ataxin-1 protein. *J Mol Biol* **354**, 883-893, doi:10.1016/j.jmb.2005.09.083 (2005).
80 de Chiara, C. *et al.* Self-assembly and conformational heterogeneity of the AXH domain of ataxin-1: an unusual example of a chameleon fold. *Biophys J* **104**, 1304-1313, doi:10.1016/j.bpj.2013.01.048 (2013).
81 Menon, R. P. *et al.* Mapping the self-association domains of ataxin-1: identification of novel non overlapping motifs. *PeerJ* **2**, e323, doi:10.7717/peerj.323 (2014).
82 Monsellier, E., Redeker, V., Ruiz-Arlandis, G., Bousset, L. & Melki, R. Molecular interaction between the chaperone Hsc70 and the N-terminal flank of huntingtin exon 1 modulates aggregation. *J Biol Chem* **290**, 2560-2576, doi:10.1074/jbc.M114.603332 (2015).
83 Wang, Z. M. & Lashuel, H. A. Discovery of a novel aggregation domain in the huntingtin protein: implications for the mechanisms of Htt aggregation and toxicity. *Angew Chem Int Ed Engl* **52**, 562-567, doi:10.1002/anie.201206561 (2013).
84 Wanker, E. E. *et al.* Membrane filter assay for detection of amyloid-like polyglutamine-containing protein aggregates. *Methods Enzymol* **309**, 375-386 (1999).
85 Chen, S., Berthelier, V., Yang, W. & Wetzel, R. Polyglutamine aggregation behavior in vitro supports a recruitment mechanism of cytotoxicity. *J Mol Biol* **311**, 173-182, doi:10.1006/jmbi.2001.4850 (2001).

86 Kar, K., Jayaraman, M., Sahoo, B., Kodali, R. & Wetzel, R. Critical nucleus size for disease-related polyglutamine aggregation is repeat-length dependent. *Nat Struct Mol Biol* **18**, 328-336, doi:10.1038/nsmb.1992 (2011).
87 Xue, W. F., Homans, S. W. & Radford, S. E. Systematic analysis of nucleation-dependent polymerization reveals new insights into the mechanism of amyloid self-assembly. *Proc Natl Acad Sci U S A* **105**, 8926-8931, doi:10.1073/pnas.0711664105 (2008).
88 Chiti, F. & Dobson, C. M. Protein misfolding, functional amyloid, and human disease. *Annu Rev Biochem* **75**, 333-366, doi:10.1146/annurev.biochem.75.101304.123901 (2006).
89 Legleiter, J. *et al.* Mutant huntingtin fragments form oligomers in a polyglutamine length-dependent manner in vitro and in vivo. *J Biol Chem* **285**, 14777-14790, doi:10.1074/jbc.M109.093708 (2010).
90 Walters, R. H. & Murphy, R. M. Examining polyglutamine peptide length: a connection between collapsed conformations and increased aggregation. *J Mol Biol* **393**, 978-992, doi:10.1016/j.jmb.2009.08.034 (2009).
91 Walters, R. H. & Murphy, R. M. Aggregation kinetics of interrupted polyglutamine peptides. *J Mol Biol* **412**, 505-519, doi:10.1016/j.jmb.2011.07.003 (2011).
92 Thakur, A. K. *et al.* Polyglutamine disruption of the huntingtin exon 1 N terminus triggers a complex aggregation mechanism. *Nat Struct Mol Biol* **16**, 380-389, doi:10.1038/nsmb.1570 (2009).
93 Adegbuyiro, A., Sedighi, F., Pilkington, A. W. t., Groover, S. & Legleiter, J. Proteins Containing Expanded Polyglutamine Tracts and Neurodegenerative Disease. *Biochemistry* **56**, 1199-1217, doi:10.1021/acs.biochem.6b00936 (2017).
94 Orr, H. T. Polyglutamine neurodegeneration: expanded glutamines enhance native functions. *Curr Opin Genet Dev* **22**, 251-255, doi:10.1016/j.gde.2012.01.001 (2012).
95 Fink, A. L. Protein aggregation: folding aggregates, inclusion bodies and amyloid. *Fold Des* **3**, R9-23, doi:10.1016/S1359-0278(98)00002-9 (1998).
96 Lasagna-Reeves, C. A. *et al.* A native interactor scaffolds and stabilizes toxic ATAXIN-1 oligomers in SCA1. *Elife* **4**, doi:10.7554/eLife.07558 (2015).
97 Nagai, Y. *et al.* A toxic monomeric conformer of the polyglutamine protein. *Nat Struct Mol Biol* **14**, 332-340, doi:10.1038/nsmb1215 (2007).
98 Olshina, M. A. *et al.* Tracking mutant huntingtin aggregation kinetics in cells reveals three major populations that include an invariant oligomer pool. *J Biol Chem* **285**, 21807-21816, doi:10.1074/jbc.M109.084434 (2010).
99 Todd, T. W. & Lim, J. Aggregation formation in the polyglutamine diseases: protection at a cost? *Mol Cells* **36**, 185-194, doi:10.1007/s10059-013-0167-x (2013).
100 Arrasate, M., Mitra, S., Schweitzer, E. S., Segal, M. R. & Finkbeiner, S. Inclusion body formation reduces levels of mutant huntingtin and the risk of neuronal death. *Nature* **431**, 805-810, doi:10.1038/nature02998 (2004).
101 Ross, C. A. & Poirier, M. A. Protein aggregation and neurodegenerative disease. *Nat Med* **10 Suppl**, S10-17, doi:10.1038/nm1066 (2004).
102 Shao, J. & Diamond, M. I. Polyglutamine diseases: emerging concepts in pathogenesis and therapy. *Hum Mol Genet* **16 Spec No. 2**, R115-123, doi:10.1093/hmg/ddm213 (2007).
103 Slow, E. J. *et al.* Absence of behavioral abnormalities and neurodegeneration in vivo despite widespread neuronal huntingtin inclusions. *Proc Natl Acad Sci U S A* **102**, 11402-11407, doi:10.1073/pnas.0503634102 (2005).
104 Pennuto, M., Palazzolo, I. & Poletti, A. Post-translational modifications of expanded polyglutamine proteins: impact on neurotoxicity. *Hum Mol Genet* **18**, R40-47, doi:10.1093/hmg/ddn412 (2009).
105 Sambataro, F. & Pennuto, M. Post-translational Modifications and Protein Quality Control in Motor Neuron and Polyglutamine Diseases. *Front Mol Neurosci* **10**, 82, doi:10.3389/fnmol.2017.00082 (2017).
106 Kuiper, E. F., de Mattos, E. P., Jardim, L. B., Kampinga, H. H. & Bergink, S. Chaperones in Polyglutamine Aggregation: Beyond the Q-Stretch. *Front Neurosci* **11**, 145, doi:10.3389/fnins.2017.00145 (2017).
107 Fiumara, F., Fioriti, L., Kandel, E. R. & Hendrickson, W. A. Essential role of coiled coils for aggregation and activity of Q/N-rich prions and PolyQ proteins. *Cell* **143**, 1121-1135, doi:10.1016/j.cell.2010.11.042 (2010).

108 Petrakis, S., Schaefer, M. H., Wanker, E. E. & Andrade-Navarro, M. A. Aggregation of polyQ-extended proteins is promoted by interaction with their natural coiled-coil partners. *Bioessays* **35**, 503-507, doi:10.1002/bies.201300001 (2013).
109 Chai, Y., Berke, S. S., Cohen, R. E. & Paulson, H. L. Poly-ubiquitin binding by the polyglutamine disease protein ataxin-3 links its normal function to protein surveillance pathways. *J Biol Chem* **279**, 3605-3611, doi:10.1074/jbc.M310939200 (2004).
110 Robertson, A. L. *et al.* Small heat-shock proteins interact with a flanking domain to suppress polyglutamine aggregation. *Proc Natl Acad Sci U S A* **107**, 10424-10429, doi:10.1073/pnas.0914773107 (2010).
111 Popiel, H. A. *et al.* The Aggregation Inhibitor Peptide QBP1 as a Therapeutic Molecule for the Polyglutamine Neurodegenerative Diseases. *J Amino Acids* **2011**, 265084, doi:10.4061/2011/265084 (2011).
112 Padlan, E. A. Anatomy of the antibody molecule. *Mol Immunol* **31**, 169-217 (1994).
113 Hamers-Casterman, C. *et al.* Naturally occurring antibodies devoid of light chains. *Nature* **363**, 446-448, doi:10.1038/363446a0 (1993).
114 Muyldermans, S., Cambillau, C. & Wyns, L. Recognition of antigens by single-domain antibody fragments: the superfluous luxury of paired domains. *Trends Biochem Sci* **26**, 230-235 (2001).
115 Desmyter, A. *et al.* Crystal structure of a camel single-domain VH antibody fragment in complex with lysozyme. *Nat Struct Biol* **3**, 803-811 (1996).
116 Stanfield, R. L., Dooley, H., Flajnik, M. F. & Wilson, I. A. Crystal structure of a shark single-domain antibody V region in complex with lysozyme. *Science* **305**, 1770-1773, doi:10.1126/science.1101148 (2004).
117 Vu, K. B., Ghahroudi, M. A., Wyns, L. & Muyldermans, S. Comparison of llama VH sequences from conventional and heavy chain antibodies. *Mol Immunol* **34**, 1121-1131 (1997).
118 Wesolowski, J. *et al.* Single domain antibodies: promising experimental and therapeutic tools in infection and immunity. *Med Microbiol Immunol* **198**, 157-174, doi:10.1007/s00430-009-0116-7 (2009).
119 Holliger, P. & Hudson, P. J. Engineered antibody fragments and the rise of single domains. *Nat Biotechnol* **23**, 1126-1136, doi:10.1038/nbt1142 (2005).
120 Rasmussen, S. G. *et al.* Crystal structure of the beta2 adrenergic receptor-Gs protein complex. *Nature* **477**, 549-555, doi:10.1038/nature10361 (2011).
121 Baranova, E. *et al.* SbsB structure and lattice reconstruction unveil Ca2+ triggered S-layer assembly. *Nature* **487**, 119-122, doi:10.1038/nature11155 (2012).
122 Park, Y. J., Pardon, E., Wu, M., Steyaert, J. & Hol, W. G. Crystal structure of a heterodimer of editosome interaction proteins in complex with two copies of a cross-reacting nanobody. *Nucleic Acids Res* **40**, 1828-1840, doi:10.1093/nar/gkr867 (2012).
123 Korotkov, K. V. *et al.* Structural and functional studies on the interaction of GspC and GspD in the type II secretion system. *PLoS Pathog* **7**, e1002228, doi:10.1371/journal.ppat.1002228 (2011).
124 Rasmussen, S. G. *et al.* Structure of a nanobody-stabilized active state of the beta(2) adrenoceptor. *Nature* **469**, 175-180, doi:10.1038/nature09648 (2011).
125 Low, C. *et al.* Nanobody mediated crystallization of an archeal mechanosensitive channel. *PLoS One* **8**, e77984, doi:10.1371/journal.pone.0077984 (2013).
126 Cromie, K. D., Van Heeke, G. & Boutton, C. Nanobodies and their Use in GPCR Drug Discovery. *Curr Top Med Chem* **15**, 2543-2557 (2015).
127 Loris, R. *et al.* Crystal structure of the intrinsically flexible addiction antidote MazE. *J Biol Chem* **278**, 28252-28257, doi:10.1074/jbc.M302336200 (2003).
128 Abskharon, R. N. *et al.* Combining in-situ proteolysis and microseed matrix screening to promote crystallization of PrPc-nanobody complexes. *Protein Eng Des Sel* **24**, 737-741, doi:10.1093/protein/gzr017 (2011).
129 De Genst, E. & Dobson, C. M. Nanobodies as structural probes of protein misfolding and fibril formation. *Methods Mol Biol* **911**, 533-558, doi:10.1007/978-1-61779-968-6_34 (2012).
130 Pain, C., Dumont, J. & Dumoulin, M. Camelid single-domain antibody fragments: Uses and prospects to investigate protein misfolding and aggregation, and to treat diseases associated with these phenomena. *Biochimie* **111**, 82-106, doi:10.1016/j.biochi.2015.01.012 (2015).

131 Iljina, M. *et al.* Nanobodies raised against monomeric a-synuclein inhibit fibril formation and destabilize toxic oligomeric species. *BMC Biol* **15**, 57, doi:10.1186/s12915-017-0390-6 (2017).
132 Miller, T. W. & Messer, A. Intrabody applications in neurological disorders: progress and future prospects. *Mol Ther* **12**, 394-401, doi:10.1016/j.ymthe.2005.04.003 (2005).
133 Lecerf, J. M. *et al.* Human single-chain Fv intrabodies counteract in situ huntingtin aggregation in cellular models of Huntington's disease. *Proc Natl Acad Sci U S A* **98**, 4764-4769, doi:10.1073/pnas.071058398 (2001).
134 Miller, T. W. *et al.* A human single-chain Fv intrabody preferentially targets amino-terminal Huntingtin's fragments in striatal models of Huntington's disease. *Neurobiol Dis* **19**, 47-56, doi:10.1016/j.nbd.2004.11.003 (2005).
135 Pardon, E. *et al.* A general protocol for the generation of Nanobodies for structural biology. *Nat Protoc* **9**, 674-693, doi:10.1038/nprot.2014.039 (2014).
136 Kayed, R. *et al.* Fibril specific, conformation dependent antibodies recognize a generic epitope common to amyloid fibrils and fibrillar oligomers that is absent in prefibrillar oligomers. *Mol Neurodegener* **2**, 18, doi:10.1186/1750-1326-2-18 (2007).
137 Kayed, R. *et al.* Common structure of soluble amyloid oligomers implies common mechanism of pathogenesis. *Science* **300**, 486-489, doi:10.1126/science.1079469 (2003).
138 Franke, D. *et al.* ATSAS 2.8: a comprehensive data analysis suite for small-angle scattering from macromolecular solutions. *J Appl Crystallogr* **50**, 1212-1225, doi:10.1107/S1600576717007786 (2017).
139 Svergun, D. Determination of the regularization parameter in indirect-transform methods using perceptual criteria. *Journal of Applied Crystallography* **25**, 495-503, doi:doi:10.1107/S0021889892001663 (1992).
140 Franke, D. & Svergun, D. I. DAMMIF, a program for rapid ab-initio shape determination in small-angle scattering. *J Appl Crystallogr* **42**, 342-346, doi:10.1107/S0021889809000338 (2009).
141 Volkov, V. V. & Svergun, D. I. Uniqueness of ab initio shape determination in small-angle scattering. *Journal of Applied Crystallography* **36**, 860-864, doi:doi:10.1107/S0021889803000268 (2003).
142 Svergun, D., Barberato, C. & Koch, M. H. J. CRYSOL - a Program to Evaluate X-ray Solution Scattering of Biological Macromolecules from Atomic Coordinates. *Journal of Applied Crystallography* **28**, 768-773, doi:doi:10.1107/S0021889895007047 (1995).
143 Petoukhov, M. V. *et al.* New developments in the ATSAS program package for small-angle scattering data analysis. *Journal of Applied Crystallography* **45**, 342-350, doi:doi:10.1107/S0021889812007662 (2012).
144 Marek, P., Mukherjee, S., Zanni, M. T. & Raleigh, D. P. Residue-specific, real-time characterization of lag-phase species and fibril growth during amyloid formation: a combined fluorescence and IR study of p-cyanophenylalanine analogs of islet amyloid polypeptide. *J Mol Biol* **400**, 878-888, doi:10.1016/j.jmb.2010.05.041 (2010).
145 Meng, F., Marek, P., Potter, K. J., Verchere, C. B. & Raleigh, D. P. Rifampicin does not prevent amyloid fibril formation by human islet amyloid polypeptide but does inhibit fibril thioflavin-T interactions: implications for mechanistic studies of beta-cell death. *Biochemistry* **47**, 6016-6024, doi:10.1021/bi702518m (2008).
146 De Genst, E. J. *et al.* Structure and properties of a complex of alpha-synuclein and a single-domain camelid antibody. *J Mol Biol* **402**, 326-343, doi:10.1016/j.jmb.2010.07.001 (2010).
147 Brockhaus, M. *et al.* Thermodynamic studies on the interaction of antibodies with beta-amyloid peptide. *J Phys Chem B* **111**, 1238-1243, doi:10.1021/jp0664059 (2007).
148 Silva, A. *et al.* Distribution of amyloid-like and oligomeric species from protein aggregation kinetics. *Angew Chem Int Ed Engl*, doi:10.1002/anie.201707345 (2017).

Appendix

Isoform	Sequence	Molecular Weight	Abs 0.1 % (1 g/L)
Atx-3 JD	MHHHHHESIFHEKQEGSLCAQHCLNNLLQGEYFSP VELSSIAHQLDEEERMRMAEGGVTSEDYRTFLQQPS GNMDDSGFFSIQVISNALKVWGLELILFNSPEYQRLRI DPINERSFICNYKEHWFTVRKLGKQWFNLNSLLTGP ELISDTYLALFLAQLQQEGYSIFVVKGDLPDCEADQL LQMIR	21.86 kDa	1.175
Atx-3 D1	MSYYHHHHHHLENLYFQGMESIFHEKQEGSLCAQH CLNNLLQGEYFSPVELSSIAHQLDEEERMRMAEGGV TSEDYRTFLQQPSGNMDDSGFFSIQVISNALKVWGLE LILFNSPEYQRLRIDPINERSFICNYKEHWFTVRKLGK QWFNLNSLLTGPELISDTYLALFLAQLQQEGYSIFVV KGDLPDCEADQLLQMIRVQQMHRPKLIGEELAQLK EQRVHKTDLERVLEANDGSGMLDEDEEDLQRALAL SRQEIDMEDEEADLRRTIQLSMQGSSR	32.58 kDa	0.926
Atx-3 13Q	MSYYHHHHHHLENLYFQGMESIFHEKQEGSLCAQH CLNNLLQGEYFSPVELSSIAHQLDEEERMRMAEGGV TSEDYRTFLQQPSGNMDDSGFFSIQVISNALKVWGLE LILFNSPEYQRLRIDPINERSFICNYKEHWFTVRKLGK QWFNLNSLLTGPELISDTYLALFLAQLQQEGYSIFVV KGDLPDCEADQLLQMIRVQQMHRPKLIGEELAQLK EQRVHKTDLERVLEANDGSGMLDEDEEDLQRALAL SRQEIDMEDEEADLRRTIQLSMQGSSRNISQDMTQTS GTNLTSEELRKRREAYFEKQQQKQQQQQQQQQQG DLSGQSSHPCERPATSSGALGSDLGDAMSEEDMLQA AVTMSLETVRNDLKTEGKK	43.58 kDa	0.726
Atx-3 77Q	MSYYHHHHHHLENLYFQGMESIFHEKQEGSLCAQH CLNNLLQGEYFSPVELSSIAHQLDEEERMRMAEGGV TSEDYRTFLQQPSGNMDDSGFFSIQVISNALKVWGLE LILFNSPEYQRLRIDPINERSFICNYKEHWFTVRKLGK QWFNLNSLLTGPELISDTYLALFLAQLQQEGYSIFVV KGDLPDCEADQLLQMIRVQQMHRPKLIGEELAQLK EQRVHKTDLERVLEANDGSGMLDEDEEDLQRALAL SRQEIDMEDEEADLRRTIQLSMQGSSRNISQDMTQTS GTNLTSEELRKRREAYFEKQQQKQQQQQQQQQQQ QQQQQQQQQQQQQQQQQQQQQQQQQQQQQQQQ QQQQQQQQQQQQQQQQQQQQQQQQQQQQQQQQ RDLSGQSSHPCERPATSSGALGSDLGDAMSEEDML QAAVTMSLETVRNDLKTEGKK	51.88 kDa	0.610
NB01	-	14.16	1.523
NB02	-	14.50	1.281
NB03	-	15.09	2.157
NB05	-	14.08	1.425

NB01

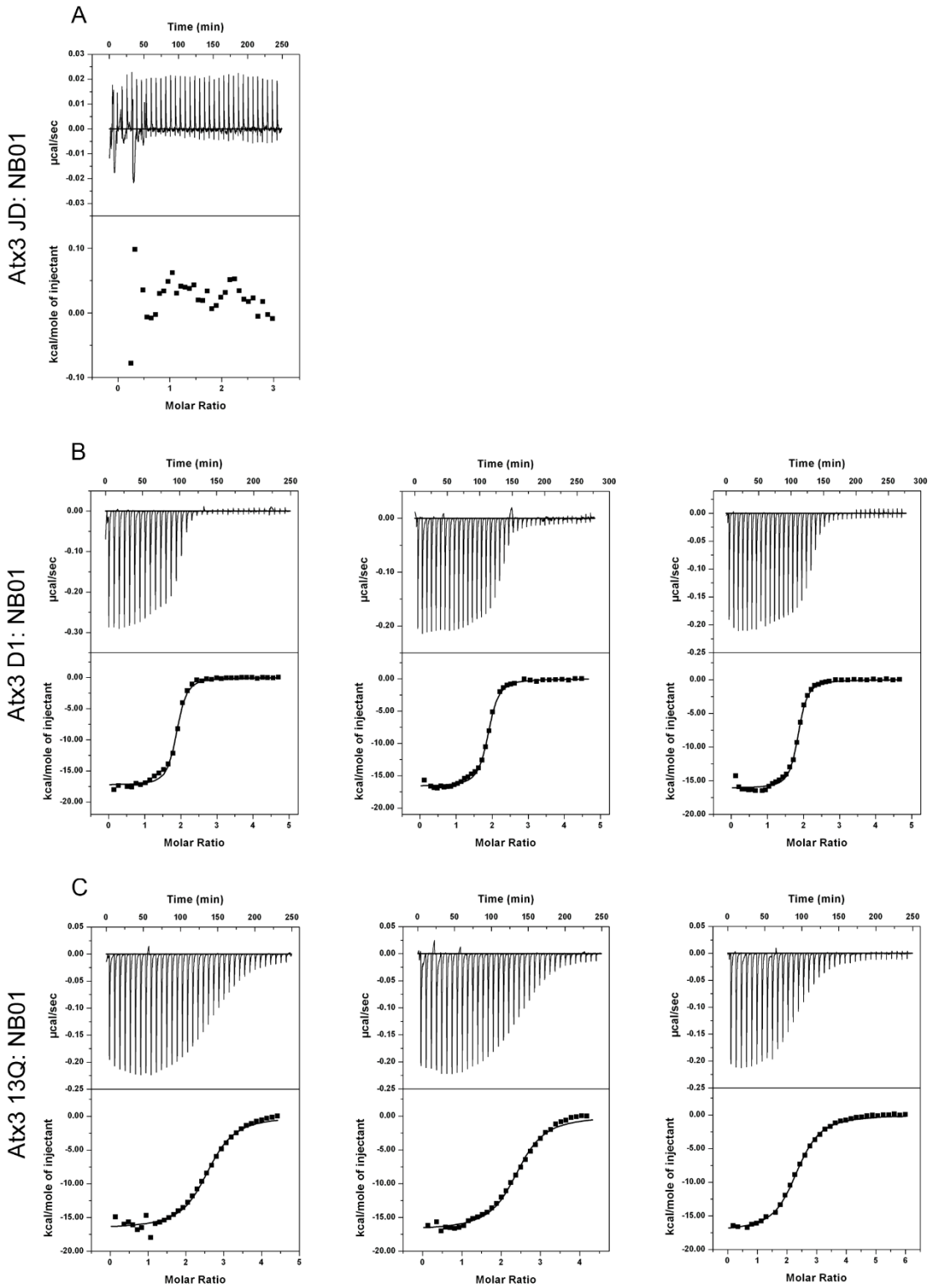
A
Time (min)
µcal/sec
kcal/mole of injectant
Molar Ratio
Atx3 JD: NB01
B
Atx3 D1: NB01
C
Atx3 13Q: NB01

D

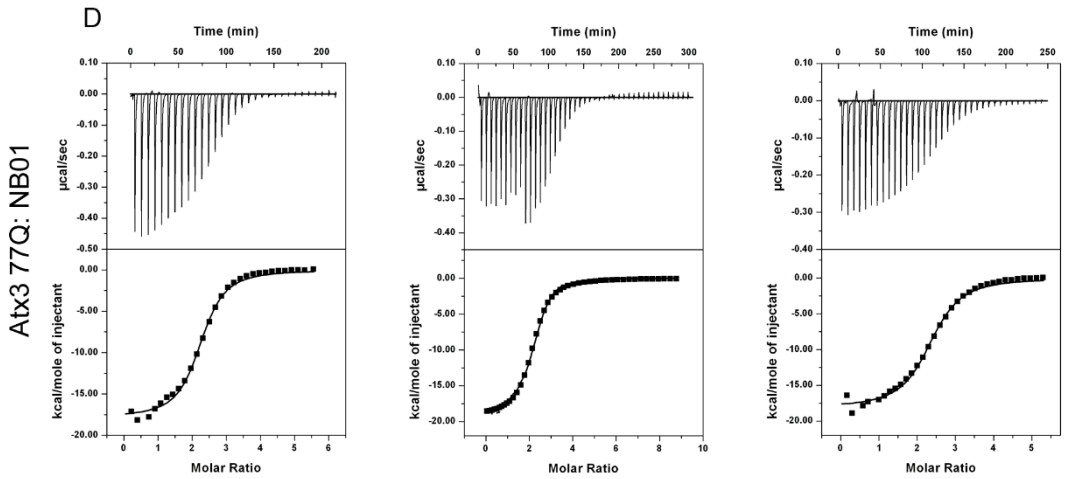

E

NB01					
Protein	N (Molar Ration)	K_D (uM)	ΔH (kcal/mol)	-TΔSb (kcal/mol)	ΔG (kcal/mol)
Atx3 JD	-	-	-	-	-
Atx3 D1	1.83 ± 0.01	47.2 ± 0.4	-17.29 ± 0.13	7.48	-9.82
	1.86 ± 0.01	56.8 ± 0.7	-16.65 ± 0.10	6.92	-9.73
	1.82 ± 0.01	44.1 ± 0.4	-16.11 ± 0.12	6.24	-9.87
Atx3 13Q	2.57 ± 0.02	204.1 ± 1.5	-16.60 ± 0.23	7.65	-8.95
	2.40 ± 0.02	222.2 ± 2.3	-16.87 ± 0.18	7.94	-8.93
	2.32 ± 0.01	208.8 ± 3.7	-17.00 ± 0.13	8.33	-8.67
Atx3 77Q	2.22 ± 0.02	303.0 ± 3.1	-17.86 ± 0.21	9.12	-8.74
	2.16 ± 0.02	389.1 ± 8.5	-19.23 ± 0.16	10.64	-8.59
	2.36 ± 0.02	305.8 ± 3.1	-18.13 ± 0.23	9.38	-8.75

Figure 44: NB01 vs Atx-3 variants ITC assay. A) Atx-3 JD vs NB01, B) Atx-3 D1:NB01 in triplicates, C) Atx-3 13Q:NB01 in triplicates, D) Atx-3 77Q:NB01 in triplicates. Measure of the heat that is released during the NB01 injections (µcal/seg) and experimental data fitting using a non-linear regression. E) Parameter values N (molar ratio), K_D, ΔH, -TΔS and ΔG, experimental error of each assay.

NB02

A

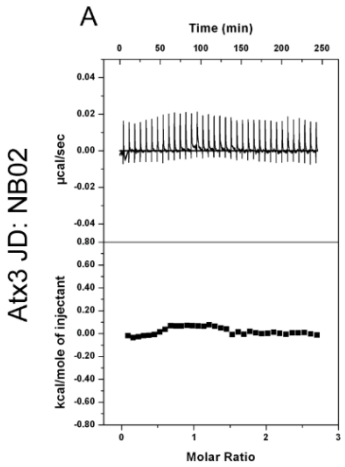

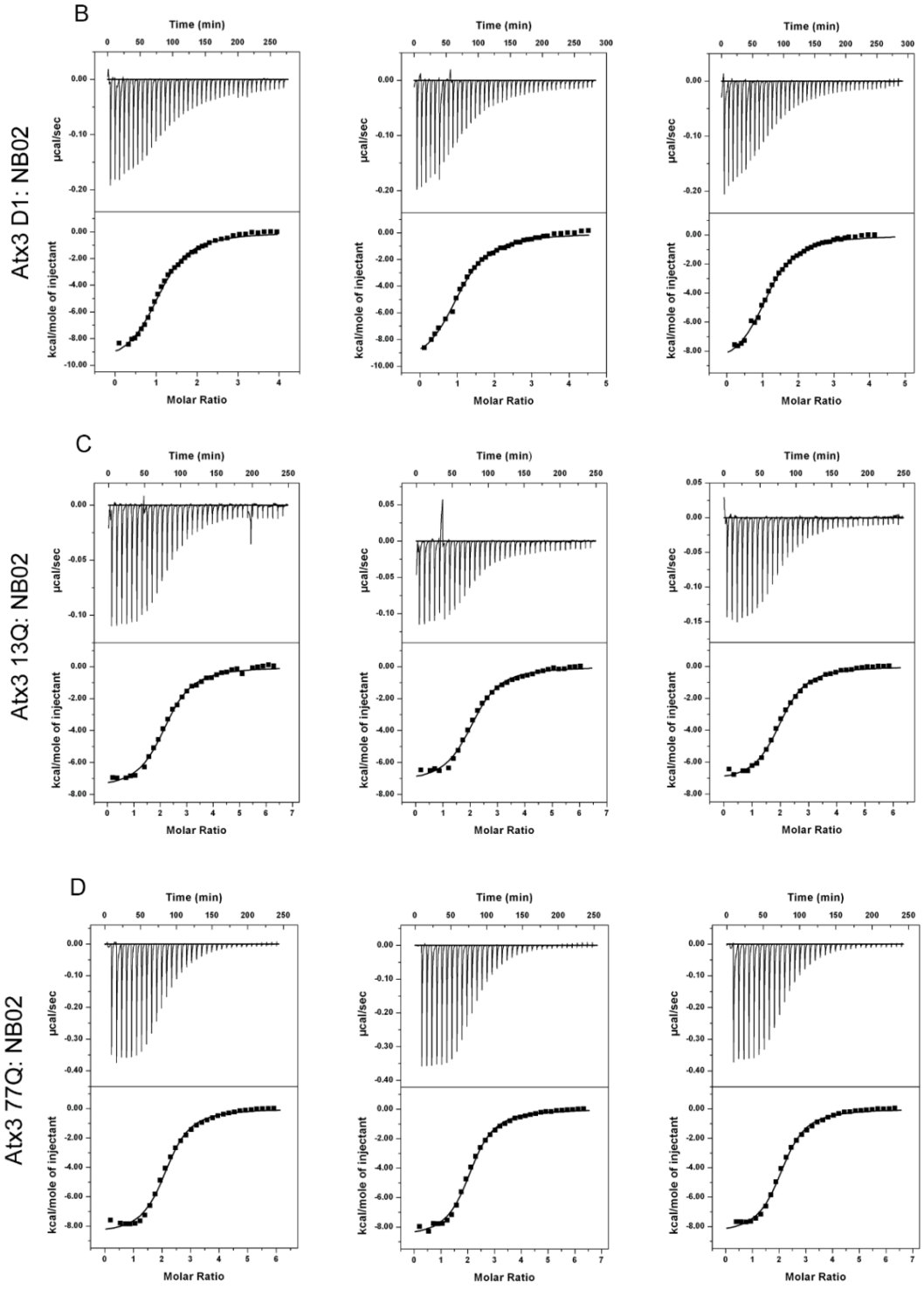
B
Atx3 D1: NB02
C
Atx3 13Q: NB02
D
Atx3 77Q: NB02
Time (min)
µcal/sec
kcal/mole of injectant
Molar Ratio

E

NB02					
Protein	N (Molar Ratio)	K_D (uM)	ΔH (kcal/mol)	-TΔSb (kcal/mol)	ΔG (kcal/mol)
Atx3 JD	-	-	-	-	-
Atx3 D1	1.14 ± 0.02	1202 ± 15	-10.0 ± 0.2	2.09	-7.94
	1.11 ± 0.02	1698 ± 22	-10.3 ± 0.3	2.52	-7.73
	1.19 ± 0.02	1431 ± 20	-9.22 ± 0.19	1.38	-7.84
Atx3 13Q	2.22 ± 0.02	403 ± 5	-7.67 ± 0.11	-0.90	-8.58
	2.12 ± 0.03	405 ± 4	-7.28 ± 0.13	-1.28	-8.58
	2.02 ± 0.02	463 ± 6	-7.25± 0.09	-1.25	-8.50
Atx3 77Q	2.14 ± 0.02	855 ± 8	-8.56 ± 0.13	0.41	-8.14
	2.11 ± 0.02	917 ± 1	-8.52 ± 0.11	0.42	-8.10
	2.11 ±0.02	962 ± 1	-8.72 ± 0.11	0.65	-8.07

Figure 45: NB02 vs Atx-3 variants ITC assay. A) Atx-3 JD vs NB02, B) Atx-3 D1:NB02 in triplicates, C) Atx-3 13Q:NB02 in triplicates, D) Atx-3 77Q:NB02 in triplicates. Measure of the heat that is released during the NB02 injections (μcal/seg) and experimental data fitting using a non-linear regression. E) Parameter values N (molar ratio), K_D, ΔH, -TΔS and ΔG, experimental error of each assay.

NB03

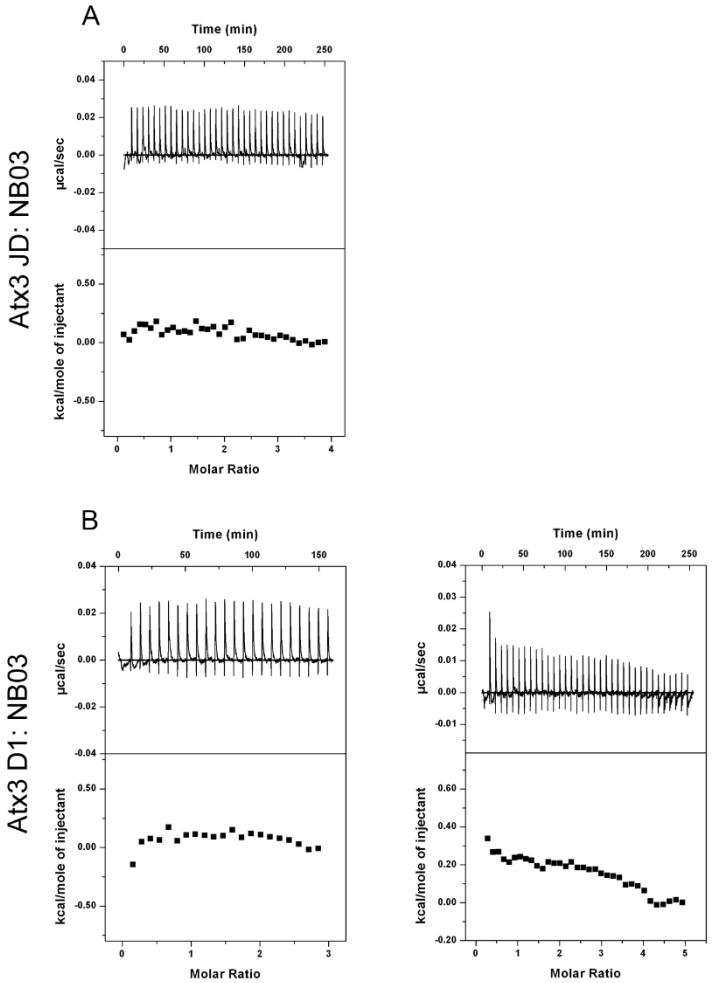

C

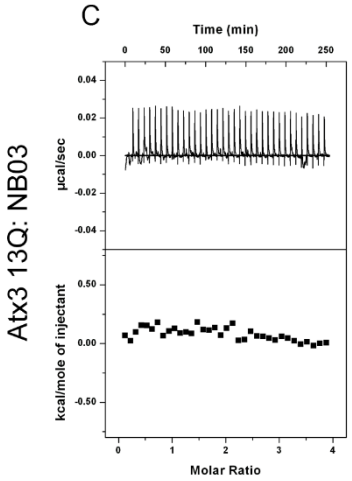

D

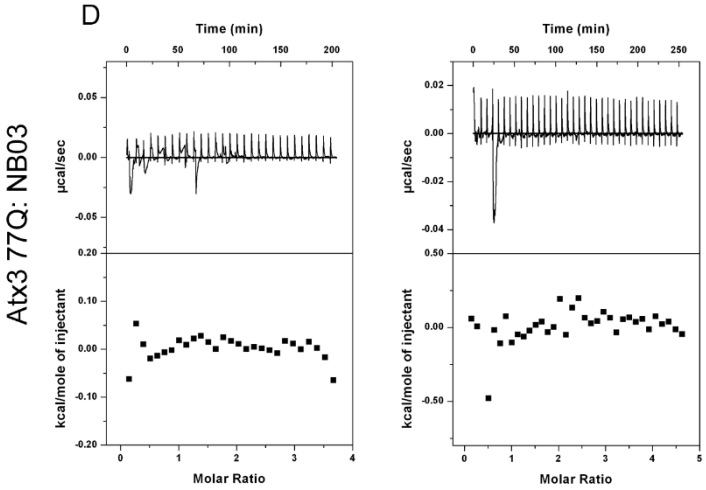

E

NB03					
Protein	N (Molar Ratio)	K_D (uM)	ΔH (kcal/mol)	-TΔSb (kcal/mol)	ΔG (kcal/mol)
Atx3 JD	-	-	-	-	-
Atx3 D1	-	-	-	-	-
Atx3 13Q	-	-	-	-	-
Atx3 77Q	-	-	-	-	-

Figure 46: NB03 vs Atx-3 variants ITC assay. A) Atx-3 JD vs NB03, B) Atx-3 D1:NB03 in triplicates, C) Atx-3 13Q:NB03 in triplicates, D) Atx-3 77Q:NB03 in triplicates. Measure of the heat that is released during the NB03 injections (µcal/seg) and experimental data fitting using a non-linear regression. E) Thermodynamic parameters were not calculated due to the absence of signal.

NB05

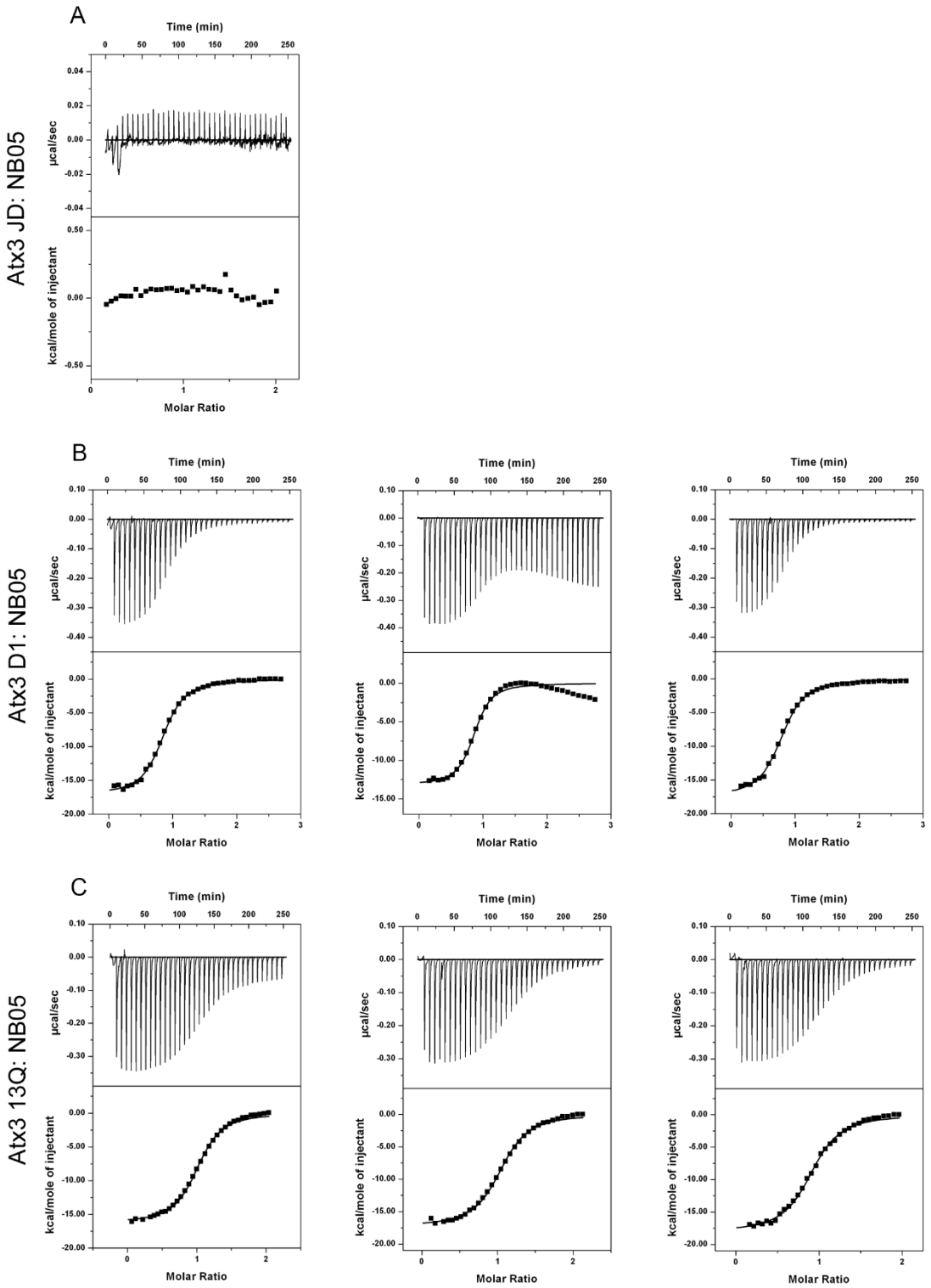
A
Time (min)
µcal/sec
kcal/mole of injectant
Molar Ratio
Atx3 JD: NB05
B
Atx3 D1: NB05
C
Atx3 13Q: NB05

D

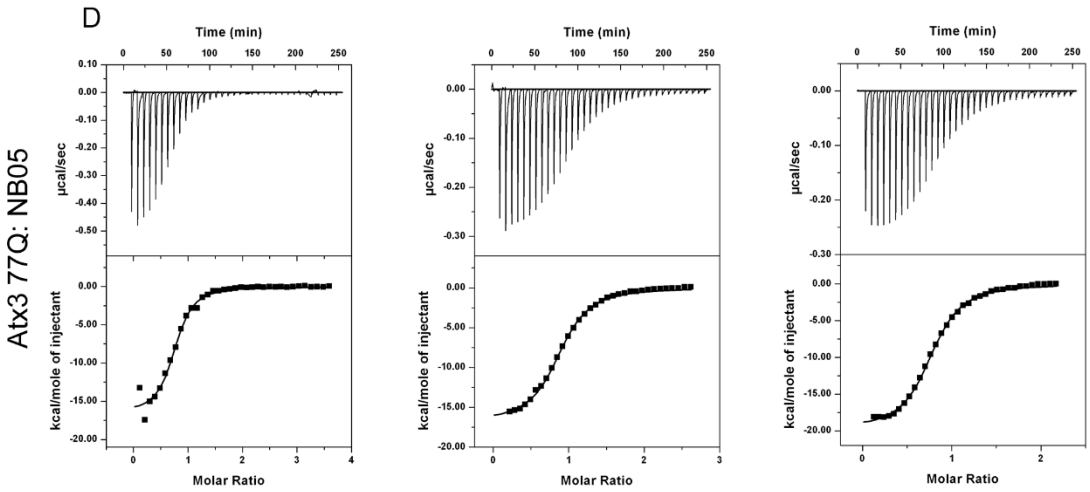

E

NB05					
Protein	N (Molar Ratio)	K_D (uM)	ΔH (kcal/mol)	-TΔSb (kcal/mol)	ΔG (kcal/mol)
Atx3 JD	-	-	-	-	-
Atx3 D1	0.85 ± 0.01	385 ± 7	-17.12 ± 0.14	8.50	-8.62
	0.80 ± 0.01	429 ± 7	-17.47 ± 0.18	8.91	-8.56
Atx3 13Q	1.02 ± 0.01	370 ± 6	-16.26 ± 0.13	7.62	-8.64
	1.05 ± 0.01	373 ± 6	-17.28 ± 0.18	8.65	-8.63
	0.92 ± 0.01	435 ± 6	-18.09 ± 0.19	9.53	-8.56
Atx3 77Q	0.75 ± 0.02	455 ± 2	-16.56 ± 0.5	8.06	-8.50
	0.88 ± 0.01	437 ± 8	-16.84 ± 0.2	8.30	-8.54
	0.78 ± 0.01	330 ± 7	-19.79 ± 0.2	11.00	-8.80

Figure 47: NB05 vs Atx-3 variants ITC assay. A) Atx-3 JD vs NB05, B) Atx-3 D1:NB05 in triplicates, C) Atx-3 13Q:NB05 in triplicates, D) Atx-3 77Q:NB05 in triplicates. Measure of the heat that is released during the NB05 injections (µcal/seg) and experimental data fitting using a non-linear regression. E) Parameter values N (molar ratio), K_D, ΔH, -TΔS and ΔG, experimental error of each assay.

Figures License:

Figure 1:

JOHN WILEY AND SONS LICENSE TERMS AND CONDITIONS

Sep 25, 2017

This Agreement between Ana Almeida ("You") and John Wiley and Sons ("John Wiley and Sons") consists of your license details and the terms and conditions provided by John Wiley and Sons and Copyright Clearance Center.

License Number	4195890300602
License date	Sep 25, 2017
Licensed Content Publisher	John Wiley and Sons
Licensed Content Publication	FEBS Journal
Licensed Content Title	The Yin and Yang of protein folding
Licensed Content Author	Thomas R. Jahn,Sheena E. Radford
Licensed Content Date	Nov 10, 2005
Licensed Content Pages	9
Type of use	Dissertation/Thesis
Requestor type	University/Academic
Format	Print and electronic
Portion	Figure/table
Number of figures/tables	1
Original Wiley figure/table number(s)	Figure 1
Will you be translating?	No
Title of your thesis / dissertation	Molecular tools to tackle protein aggregation in Machado-Joseph disease
Expected completion date	Nov 2017
Expected size (number of pages)	100
Requestor Location	Ana Almeida

Figure 4:

ACS Publications
Most Trusted. Most Cited. Most Read.

Title: Proteins Containing Expanded Polyglutamine Tracts and Neurodegenerative Disease
Author: Adewale Adegbuyiro, Faezeh Sedighi, Albert W. Pilkington, et al
Publication: Biochemistry
Publisher: American Chemical Society
Date: Mar 1, 2017
Copyright © 2017, American Chemical Society

LOGIN
If you're a copyright.com user, you can login to RightsLink using your copyright.com credentials. Already a RightsLink user or want to learn more?

PERMISSION/LICENSE IS GRANTED FOR YOUR ORDER AT NO CHARGE

This type of permission/license, instead of the standard Terms & Conditions, is sent to you because no fee is being charged for your order. Please note the following:

- Permission is granted for your request in both print and electronic formats, and translations.
- If figures and/or tables were requested, they may be adapted or used in part.
- Please print this page for your records and send a copy of it to your publisher/graduate school.
- Appropriate credit for the requested material should be given as follows: "Reprinted (adapted) with permission from (COMPLETE REFERENCE CITATION). Copyright (YEAR) American Chemical Society." Insert appropriate information in place of the capitalized words.
- One-time permission is granted only for the use specified in your request. No additional uses are granted (such as derivative works or other editions). For any other uses, please submit a new request.

If credit is given to another source for the material you requested, permission must be obtained from that source.